IN SITU CHARACTERIZATION OF PHASE TRANSITION AND DEFECT DYNAMICS IN MOLYBDENUM DITELLURIDE

by

Qingxiao Wang

APPROVED BY SUPERVISORY COMMITTEE:

Dr. Moon J. Kim, Chair

Dr. Robert M. Wallace, Co-Chair

Dr. Kyeongjae Cho

Dr. Jiyoung Kim

Dr. Luigi Colombo

Copyright 2020

Qingxiao Wang

All Rights Reserved

Dedicated to my wife, Jing Bai,

who has always loved me and supported me.

IN SITU CHARACTERIZATION OF PHASE TRANSITION AND DEFECT DYNAMICS IN MOLYBDENUM DITELLURIDE

by

QINGXIAO WANG, BS

DISSERTATION
Presented to the Faculty of
The University of Texas at Dallas
in Partial Fulfillment
of the Requirements
for the Degree of

DOCTOR OF PHILOSOPHY IN
MATERIALS SCIENCE AND ENGINEERING

THE UNIVERSITY OF TEXAS AT DALLAS
May 2020

ACKNOWLEDGMENTS

First and foremost, I would like to express my sincerest gratitude to my advisor, Dr. Moon J. Kim. I sincerely appreciate him for giving me the opportunity to pursue my doctoral degree under his supervision. I am very thankful for his great support and invaluable guidance through my research. I was very fortunate to have Dr. Robert M. Wallace, Dr. Kyeongjae Cho, Dr. Jiyoung Kim, and Dr. Luigi Colombo on my graduate committee. Their valuable suggestions and advice strengthened this research significantly. In particular, I am indebted to Dr. Wallace for his guidance and willingness during our collaboration.

In addition, I would like to thank individuals who supported my graduate studies at UT Dallas. My colleagues and group members, Dr. Jinguo Wang, Dr. Massimo Catalano, Dr. Ning Lu, Dr. Cyrus Sun, Dr. Zifan Che, Dr. Luhua Wang, and Dr. Juan Pablo Oviedo helped me a lot during my research. Particularly, I would like to acknowledge my colleague Sunah Kwon for her excellent advice and enormous discussions in order to perform my experiments. It was a wonderful experience to work with them at UT Dallas. Also, I would like to thank my collaborators from other groups, including Dr. Angelica Azcatl, Dr. Hui Zhu, Dr. Rafik Addou, Dr. Chenxi Zhang, Dr. Yifan Nie, and Dr. Lanxia Cheng, for their contributions to this research. In particular, I would like to express my gratitude to Dr. Hui Zhu, for the wealth of knowledge about the surface analysis, the numerous discussions, and extensive collaborations. It was my great pleasure to work with them in the past few years. Finally, a special thank must go to my wife, Jing Bai, and two daughters, Xuan and Ziqi, for their steadfast support and encouragement on my PhD journey.

March 2020

IN SITU CHARACTERIZATION OF PHASE TRANSITION AND DEFECT DYNAMICS IN MOLYBDENUM DITELLURIDE

Qingxiao Wang, PhD
The University of Texas at Dallas, 2020

Supervising Professor: Moon J. Kim, Chair
Robert M. Wallace, Co-Chair

Transition metal dichalcogenides (TMDs) are regarded as promising materials for emerging applications, including electronic devices, photonic devices, biosensors, and energy storage, etc. Owing to their novel structures and extraordinary properties, they have provided the researchers with an excellent platform to explore low-dimensional physics. However, some challenges need to be resolved before their practical application. The phases and defects in TMDs can significantly affect their properties. Therefore, understanding the phase transition and defects in TMDs would be of great importance to advance their further application. This dissertation focuses on the identification and characterization of a novel phase transition from two dimensional $MoTe_2$ phase to one dimensional Mo_6Te_6 nanowire phase during the vacuum annealing. Furthermore, the thermal stability of $MoTe_2$ is extensively investigated. In particular, the inversion domain boundaries formed during the vacuum annealing are identified to be a defective interface in $MoTe_2$. The role of Te vacancy to the evolution of inversion domain boundaries is extensively studied. Also, a possible strategy to improve its thermal stability is demonstrated.

TABLE OF CONTENTS

LIST OF FIGURES

LIST OF TABLES

CHAPTER 1

INTRODUCTION

1.1 Transition Metal Dichalcogenides: An Overview

Since the discovery of graphene, the research enthusiasm for two-dimensional (2D) materials has remarkably increased.[1] Among all 2D materials, transition metal dichalcogenides (TMDs) have attracted considerable attention due to their unique physical and electrical properties to fulfill the demands of future applications, such as biosensors, energy storage, nanoelectronics, etc.[2-3] TMDs are a large family of layered compounds with a formula of MX_2 (M = Mo or W; X= S, Se, or Te) and polymorphs, including the semiconducting hexagonal (2H), the metallic octahedral (1T), and the semi-metallic distorted octahedral (1T') phases (Figure 1.1).[4] In a monolayer TMD, the M-atom plane is sandwiched between two X-atom planes. The weak interlayer interactions allow the isolation of a monolayer TMD flake from its bulk crystal using the mechanical exfoliation method.[1] A wealth of compositions and structures of TMDs makes them an excellent platform to explore the new science and applications.[2-3, 5] Among TMDs, molybdenum ditelluride (2H-$MoTe_2$) is a semiconducting compound with an indirect bandgap (1.1 eV), whereas a direct bandgap (1.0 eV) is present in the monolayer $MoTe_2$. The high carrier mobility and on/off current ratio of 10^6 of $MoTe_2$ makes it a promising electronic and photovoltaic candidate.[6] However, many issues need to be addressed before the practical application, for example, the synthesis of high quality and large area flakes, the precise control of flake thickness, the reduction of defects or impurities, the search for a low contact resistance material, etc.[7] In addition, $MoTe_2$ possesses facile phase transition behavior due to the small formation energy difference between Mo and Te. Thus, the thermal stability needs to be investigated prior to its practical application.[6]

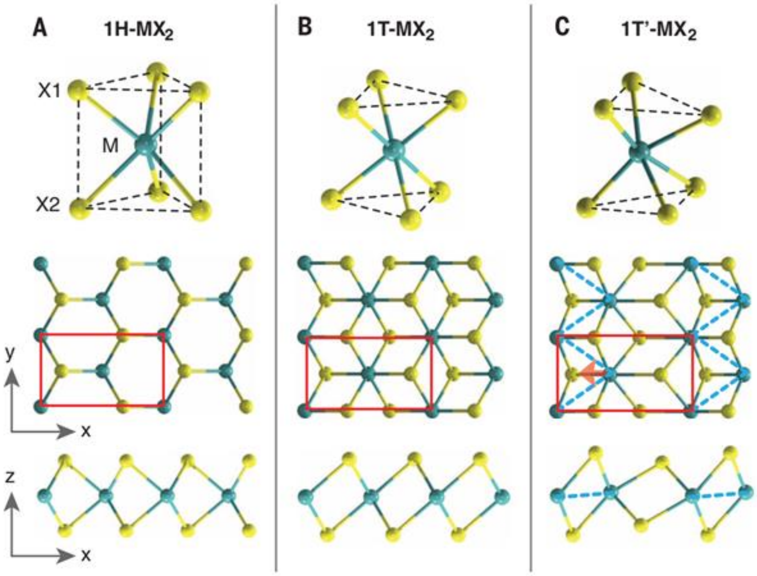

Figure 1.1. Atomic structures of monolayer transition metal dichalcogenides MX_2. M stands for (Mo, W) and X stands for (S, Se, Te). (A) 1H phase, (B) 1T phase, (C) 1T' phase. Adapted with permission from ref (4) Copyright (2014) American Association for the Advancement of Science.

A controlled phase transition of TMDs is very critical for the device performances. For example, the doping via ion implantation, a traditional method to form a low resistance contact for a field-effect transistor, is no longer practical for the atomically thin 2D materials. However, to overcome the high Schottky barrier, a new strategy based on phase engineering to form a lateral-heterojunction in the TMD flake has been extensively explored in the recent years. Figure 1.2 shows some applications that utilize phase engineering in TMDs. For example, Rajesh Kappera *et al*. demonstrated that a low contact resistance is observed by fabricating a 2H-1T' lateral heterojunction in monolayer MoS_2 by using the ion intercalation method.[8] Suyeon Cho *et al*. showed that a 2H-$MoTe_2$ to 1T'-$MoTe_2$ can be achieved using a high energy laser treatment.[6] Ying Wang *et al*. unveiled the reversible 2H-1T' phase transition in monolayer $MoTe_2$ using the electrical doping method. [9] Feng Zhang *et al.* demonstrated a vertical $MoTe_2$ resistive memory that has high on/off ratio and can realize fast state switching.[10]

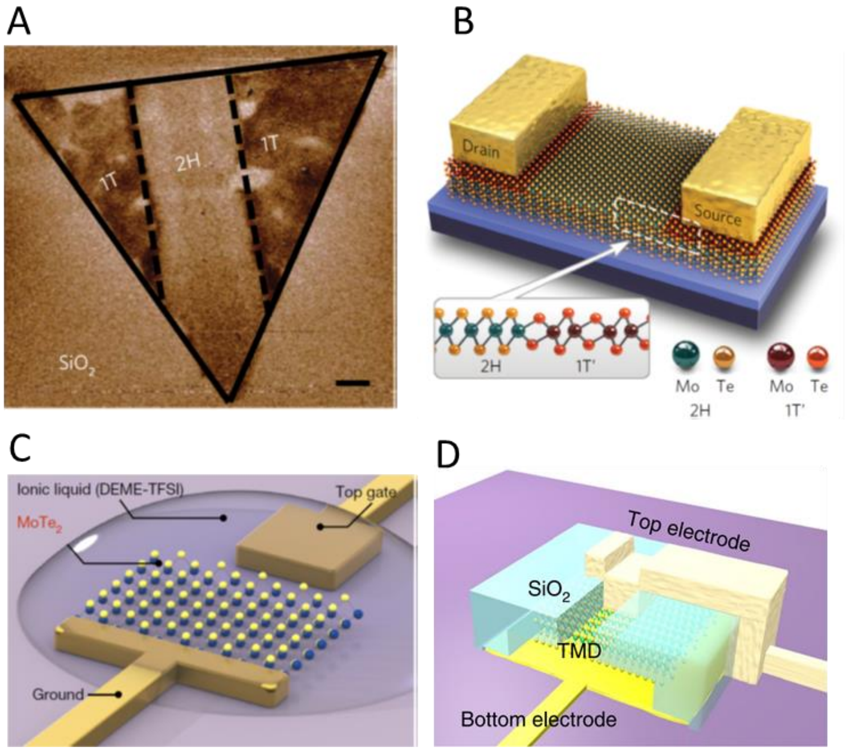

Figure 1.2. Phase Transition Methods for TMDs (A) Intercalation induced 2H-1T' phase transition in MoS_2. Adapted with permission from ref (8) Copyright (2014) Nature Publishing Group. (B) Laser treatment induced 2H-1T' phase transition in $MoTe_2$. Adapted with permission from ref (6) Copyright (2015) American Association for the Advancement of Science. (C) Electrostatic doping induced 2H-1T' phase transition in $MoTe_2$. Adapted with permission from ref (9) Copyright (2017) American Chemical Society. (D) Electrical-field induced structural transition in $Mo_xW_{1-x}Te_2$. Adapted with permission from ref (10) Copyright (2017) Nature Publishing Group.

1.2 Motivation

An accurate material characterization is of great importance to study the mechanism of phase transition and the defects in 2D materials. To date, Transition Electron Microscopy (TEM) has been widely used for the study of 2D materials. The ultra-high spatial and energy resolution makes TEM an ideal tool to explore the structure and the properties of 2D materials. In addition, it is also exciting to investigate the interaction between the high energy beam and 2D materials. The new phenomenon observed only in 2D materials will be of great interest to low dimensional physics.[4-

[5, 11] Figure 1.3 shows the rapid increase in publications of 2D materials and the TEM related studies.[12] The structure and composition of 2D have been extensively explored at the atomic scale.

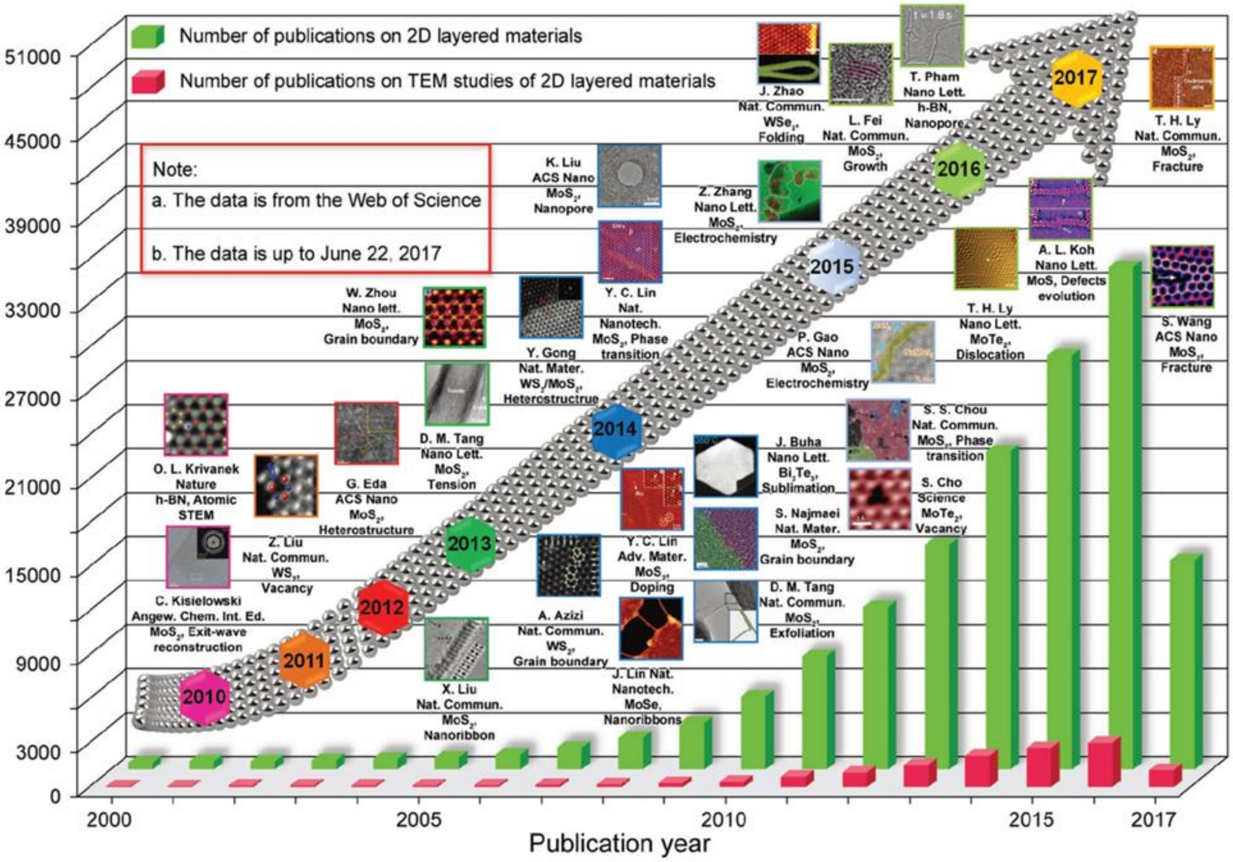

Figure 1.3. The number of publications of 2D materials in recent year. Figure adapted with permission from ref (12) Copyright (2017) John Wiley and Sons.

However, the information on structure and composition obtained using the conventional TEM is limited. With the development of the TEM instrument, especially the advance in aberration correction, and the development of sample holders for *in situ* TEM using the MEMS-based techniques, *in situ* characterization of 2D materials has been performed in recent years[12] (Figure 1.3). *In situ* TEM characterization can provide real-time observation showing the interactions between materials and the applied external fields or environments. A variety of *in situ* TEM holders have been developed in order to measure the thermal, electrical, optical, mechanical, liquid/gas environmental properties. Therefore, the relationship between the structure and property can be extensively explored. For example, the study of phase transitions and defect dynamics induced by the electron-matter interaction is a fascinating field with novel and unusual physics. Figure 1.4 shows some examples of *in situ* characterization of 2D materials. Jinhua Hong *et al*. demonstrated the electron beam induces Mo diffusion in MoS_2.[13] Yung-Chang Lin *et al*. observed the 2H-1T phase transition in monolayer MoS_2 annealed 600 °C.[14] Junhao Lin *et al*. performed the fabrication of MoSe nanowires which are sculpted from a $MoSe_2$ flake using the electron beam.[15] Xiahan Sang *et al*. investigated the edge evolution in a monolayer $MoSe_2$ flake under 450 °C annealing.[16] These results indicate that the direct patterning of nanostructures or even the manipulation of a single atom using the electron beam is possible.

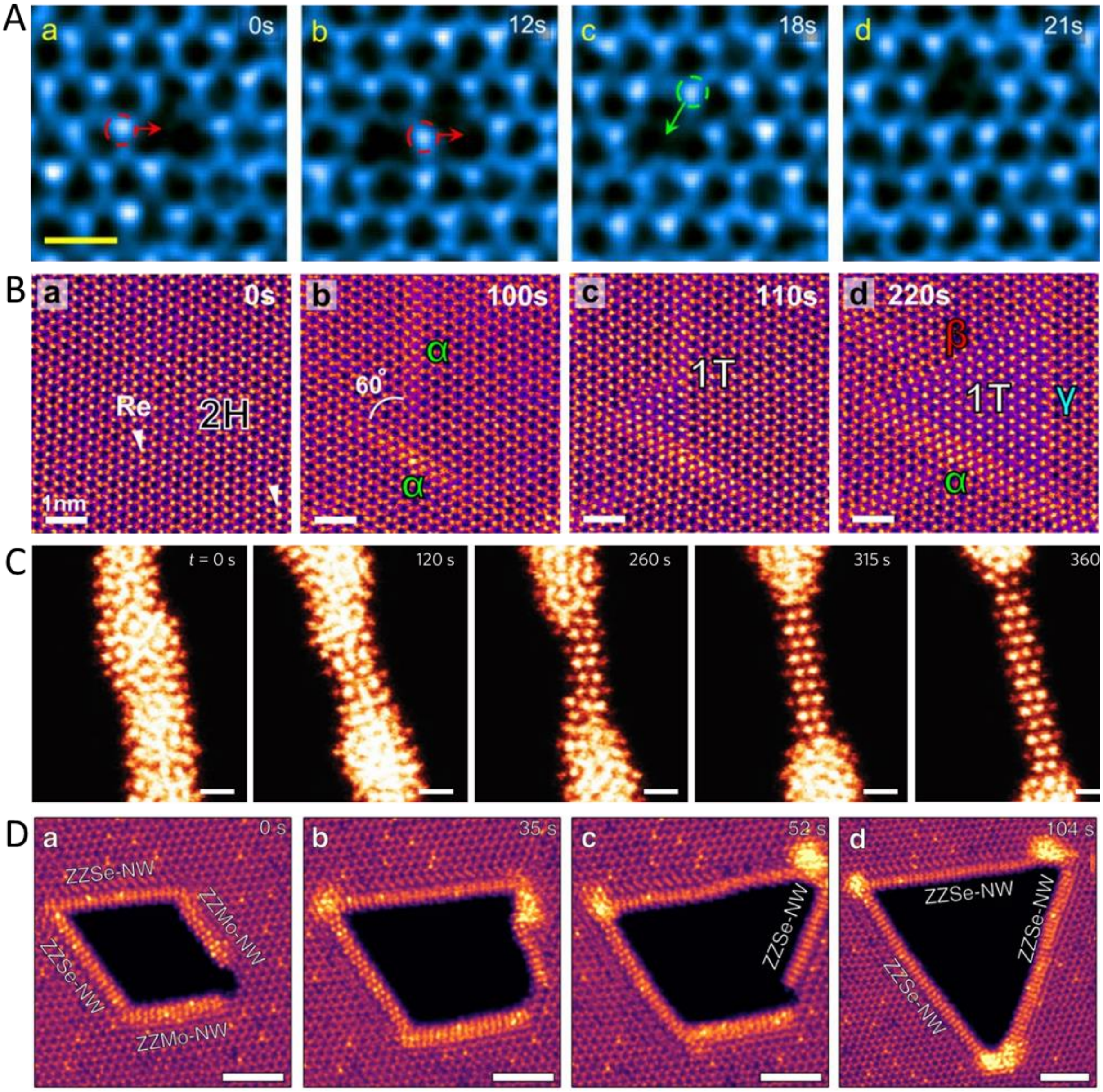

Figure 1.4. *In Situ* TEM characterization of 2D materials (A) Mo atom diffusion under the electron beam irradiation. Adapted with permission from ref (13) Copyright (2017) American Chemical Society. (B) 2H-1T phase transition of MoS_2 at 600 °C. Adapted with permission from ref (14) Copyright (2014) Nature Publishing Group. (C) Fabrication of MoSe nanowire from $MoSe_2$ using the electron beam. Adapted with permission from ref (15) Copyright (2014) Nature Publishing Group. (D) Edge evolution of $MoSe_2$ under 600 °C annealing. Adapted with permission from ref (16) Copyright (2018) Nature Publishing Group.

This dissertation mainly focuses on three types of *in situ* characterization: (1) the phase transition or defects induced by the vacuum annealing (2) the controllable phase transition under electrical biasing; (3) the phase transition or defects due to the electron-mater interaction. Its defects and thermal stability have been extensively investigated.

1.3 Dissertation Outline

In this dissertation, a new 1D nanowire phase is found during a vacuum annealing of $MoTe_2$. *In situ* characterization was carried out using STM and TEM techniques to understand the phase transition. In addition, the thermal stability of $MoTe_2$ was extensively evaluated. Moreover, the evolution of defects and a special domain boundary in $MoTe_2$ are identified and studied.

Chapter 1 gives a brief introduction of current status of 2D materials research. In addition, the study of phase transition in 2D materials is highlighted. Finally, the need and benefit of *in situ* characterization is briefly discussed.

In Chapter 2, a detailed description of the experimental techniques employed in the research is reported, including the equipment set-up and the specimen preparation techniques used, respectively.

In Chapter 3, the 2H-$MoTe_2$ to Mo_6Te_6 nanowire phase transition is extensively investigated. Firstly, a plan view observation of the phase transition for a few layers $MoTe_2$ is presented, followed by the cross-sectional characterization. Then, the structure and the electronic properties of the NW phase is evaluated using DFT calculations. After that, an *in situ* characterization of the phase transition in monolayer and bilayer $MoTe_2$ is performed. Finally, the influence of carbon residue and electron beam irradiation is investigated.

In Chapter 4, the thermal stability of $MoTe_2$ is comprehensively explored. First, the surface defects at room temperature are characterized by STM and XPS. Then, the surface morphology is monitored up to 400 °C by *in situ* STM. Wagon wheel pattern, a novel morphology, is observed using STM. After that, the structure of the Wagon wheel pattern is characterized by *in situ* TEM and the inversion domains are extensively studied by sequential STEM imaging. Lastly, the role of Te vacancy to the evolution of domain boundaries is determined.

Finally, in Chapter 5, the conclusion remarks and future work related to *in situ* electrical characterization are discussed.

1.4 References

1. Geim, A. K.; Novoselov, K. S., The rise of graphene. *Nature Materials* **2007,** *6*, 183-191.

2. Tan, C.; Cao, X.; Wu, X.-J.; He, Q.; Yang, J.; Zhang, X.; Chen, J.; Zhao, W.; Han, S.; Nam, G.-H.; Sindoro, M.; Zhang, H., Recent Advances in Ultrathin Two-Dimensional Nanomaterials. *Chemical Reviews* **2017,** *117* (9), 6225-6331.

3. Wang, Q. H.; Kalantar-Zadeh, K.; Kis, A.; Coleman, J. N.; Strano, M. S., Electronics and optoelectronics of two-dimensional transition metal dichalcogenides. *Nat Nano* **2012,** *7* (11), 699-712.

4. Qian, X.; Liu, J.; Fu, L.; Li, J., Quantum spin Hall effect in two-dimensional transition metal dichalcogenides. *Science* **2014,** *346* (6215), 1344-1347.

5. Geim, A. K.; Grigorieva, I. V., Van der Waals heterostructures. *Nature* **2013,** *499* (7459), 419-425.

6. Cho, S.; Kim, S.; Kim, J. H.; Zhao, J.; Seok, J.; Keum, D. H.; Baik, J.; Choe, D.-H.; Chang, K. J.; Suenaga, K.; Kim, S. W.; Lee, Y. H.; Yang, H., Phase patterning for ohmic homojunction contact in MoTe2. *Science* **2015,** *349* (6248), 625-628.

7. Chhowalla, M.; Jena, D.; Zhang, H., Two-dimensional semiconductors for transistors. *Nature Reviews Materials* **2016,** *1*, 16052.

8. Kappera, R.; Voiry, D.; Yalcin, S. E.; Branch, B.; Gupta, G.; Mohite, A. D.; Chhowalla, M., *Nat. Mater.* **2014,** *13*, 1128.

9. Wang, Y.; Xiao, J.; Zhu, H.; Li, Y.; Alsaid, Y.; Fong, K. Y.; Zhou, Y.; Wang, S.; Shi, W.; Wang, Y.; Zettl, A.; Reed, E. J.; Zhang, X., Structural phase transition in monolayer MoTe2 driven by electrostatic doping. *Nature* **2017,** *550* (7677), 487-491.

10. Zhang, F.; Zhang, H.; Krylyuk, S.; Milligan, C. A.; Zhu, Y.; Zemlyanov, D. Y.; Bendersky, L. A.; Burton, B. P.; Davydov, A. V.; Appenzeller, J., Electric-field induced structural transition in vertical MoTe2- and Mo1–xWxTe2-based resistive memories. *Nature Materials* **2019,** *18* (1), 55-61.

11. Manzeli, S.; Ovchinnikov, D.; Pasquier, D.; Yazyev, O. V.; Kis, A., 2D transition metal dichalcogenides. *Nature Reviews Materials* **2017,** *2,* 17033.

12. Luo, C.; Wang, C.; Wu, X.; Zhang, J.; Chu, J., In Situ Transmission Electron Microscopy Characterization and Manipulation of Two-Dimensional Layered Materials beyond Graphene. *Small* **2017,** *13* (35), 1604259.

13. Hong, J.; Pan, Y.; Hu, Z.; Lv, D.; Jin, C.; Ji, W.; Yuan, J.; Zhang, Z., Direct Imaging of Kinetic Pathways of Atomic Diffusion in Monolayer Molybdenum Disulfide. *Nano Letters* **2017,** *17* (6), 3383-3390.

14. Lin, Y.-C.; Dumcenco, D. O.; Huang, Y.-S.; Suenaga, K., Atomic mechanism of the semiconducting-to-metallic phase transition in single-layered MoS2. *Nat Nano* **2014,** *9* (5), 391-396.

15. Lin, J.; Cretu, O.; Zhou, W.; Suenaga, K.; Prasai, D.; Bolotin, K. I.; Cuong, N. T.; Otani, M.; Okada, S.; Lupini, A. R.; Idrobo, J.-C.; Caudel, D.; Burger, A.; Ghimire, N. J.; Yan, J.; Mandrus, D. G.; Pennycook, S. J.; Pantelides, S. T., Flexible metallic nanowires with self-adaptive contacts to semiconducting transition-metal dichalcogenide monolayers. *Nat Nano* **2014,** *9* (6), 436-442.

16. Sang, X.; Li, X.; Zhao, W.; Dong, J.; Rouleau, C. M.; Geohegan, D. B.; Ding, F.; Xiao, K.; Unocic, R. R., In situ edge engineering in two-dimensional transition metal dichalcogenides. *Nat Commun* **2018,** *9* (1), 2051.

CHAPTER 2

EXPERIMENTAL METHODS

The purpose of this thesis is to investigate the phase transition and defect dynamics of 2D materials ($MoTe_2$, WTe_2, etc.). This chapter introduces the experimental methods used in the research. Toward that, it is divided into three sections. The first section focuses on the priority characterization technique used in this research: transmission electron microscopy (TEM). Among all TEM techniques, scanning transmission electron microscopy (STEM) is the most frequently used characterization technique for the *in situ* study. Therefore, the STEM-related techniques, such as the aberration-corrected STEM, high angle annular dark-field (HAADF) imaging, electron energy loss spectroscopy (EELS), will be described in details. The second section explores the in-situ TEM characterization of 2D materials, including *in situ* heating and *in situ* electrical biasing, respectively. The third section introduces the specimen preparation related techniques: focused ion beam (FIB) and 2D flake transfer. The flakes transfer to the grid for *in situ* TEM experiments is so critical to the *in situ* experiment that the experimental procedures are described in detail.

2.1 Transmission Electron Microscopy

TEM is a versatile characterization technique featuring both high spatial and high energy resolution. In brief, TEM imaging can be distinguished in two categories: coherent imaging and incoherent imaging. Among all the coherent imaging techniques, the phase-contrast imaging, i.e., the high-resolution imaging (HR-TEM), which can visualize the lattice at the atomic scale, is the most used imaging technique. The selective area diffraction (SAD) and convergent beam electron diffraction (CBED), which can provide the crystallographic information of a sample in the reciprocal space, are also used for specific applications. These three operation modes are the traditional techniques for the conventional TEM.[1] In brief, the specimen is treated as a phase-object and illuminated with a plane electron wave. The image is formed by the objective lens and recorded in the image plane using a charge-coupled device (CCD) camera (Figure 2.1a). The contrast in an HR-TEM image is caused by the phase differences of the electron wave, which is attributed to the potential in the specimen. HR-TEM imaging can achieve atomic resolution, making it very useful in the characterization of a crystal structure. However, due to the interference nature of TEM mode, the contrast of the lattice image may reverse with the change of focus. The image interpretation is always the major issue for HR-TEM, especially for a complex structure, therefore image simulation is always required. [2]

With the development of electron microscopes, especially with the introduction of the aberration correctors to overcome the lens imperfections, the incoherent imaging technique, specifically, scanning transmission electron microscopy (STEM), became very popular.[1] It can combine imaging and spectroscopy simultaneously, facilitating the so-called site-specific analysis. Therefore, the relationship between the structure of a material and its chemical properties can be identified at the atomic scale. As shown in Figure 2.1b, in STEM mode, the convergent electron beam is the demagnified image of the electron source by using a series of condenser lenses and the convergence semi-angle of the electron beam is controlled by the condenser aperture.[3] The convergent beam is brought to focus on the sample and scanned over the sample in the raster manner with the help of the scanning coils. Simultaneously, the scattered electrons are collected in a serial acquisition mode by a variety of detectors below the sample. Thus, information about the sample is obtained by analyzing the signal of the detectors.

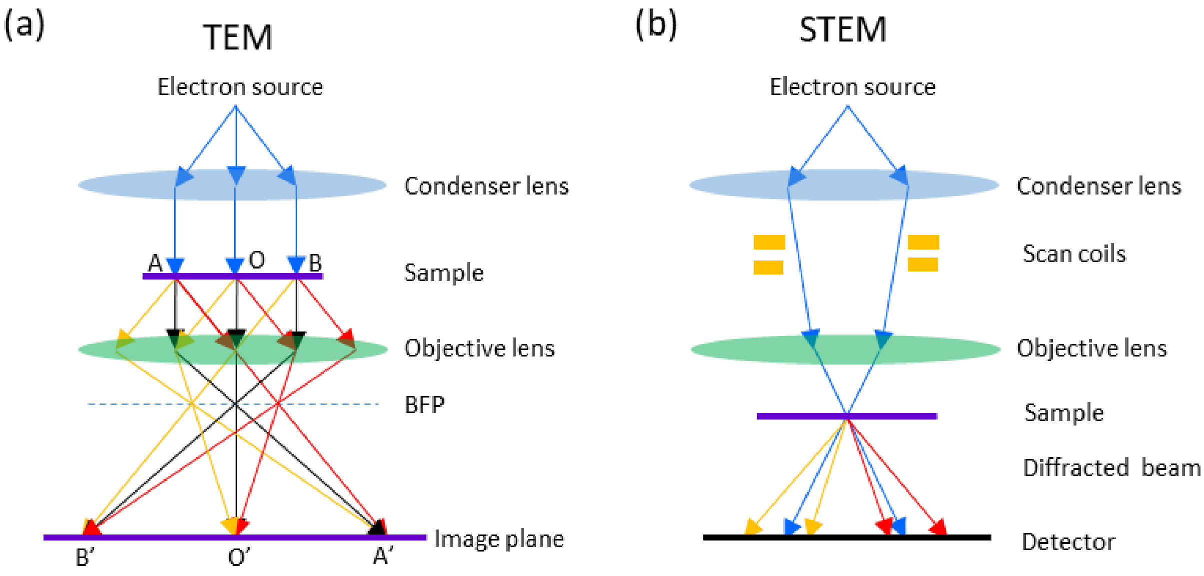

Figure 2.1. (a) Schematic diagram of TEM mode. The sample is illuminated by a parallel electron beam, and the diffraction pattern is formed at the back focal plane (BFP) of the objective lens. The image formed at the image plane is zoomed in and collected by a CCD camera. (b) Ray diagram of STEM mode. A convergent electron beam is formed with the help of the condenser lens and the objective lens pre-field and focused on the sample. The electron beam is scanned in a raster manner over the sample, and an annular dark-field detector or bright field detector, mounted below the sample, is used to collect the scattered electrons and form the image.

2.1.1 Aberration Corrected Scanning Transmission Electron Microscopy

In STEM mode, the resolution is determined by the size of the electron beam. There are many factors that can affect the resolution in the STEM mode. Firstly, similar to TEM mode, the resolution is influenced by the diffraction limit, i.e., the radius δ_D of the electron beam. The diffraction limit is defined using the Rayleigh criterion[3]

$$\delta_D = 0.61\frac{\lambda}{\alpha},$$

where λ is the electron wavelength, and α is the convergence semi-angle. It is clear that a large convergence angle is needed in order to improve the STEM resolution. Secondly, the size of the electron beam can be significantly affected by the spherical aberration of the lens. Figure 2.2 shows the influence of the spherical aberration to the focusing of a converged electron beam. The electrons with a large incident angle are deflected more by the imperfect lens and focused in front of the back focal plane of the lens. Therefore, a broad disk instead of a point-like spot is formed in front of the back focal plane of the lens. The radius of the smallest disk can be expressed as[3]

$$\delta_S = 0.25C_s\alpha^3,$$

where C_s is the constant of spherical aberration of the lens. This disk is called the disk of least confusion. It means that the size of the disk will increase if an electron beam with a larger convergence semi-angle is used. Thirdly, the energy spread of the electron beam can also influence the focusing of the electron probe. When an electron beam with the energy of E_0 passes through a lens, the electrons with slightly different energy will be focused differently. Similar with the effect of spherical aberration, the radius of the disk of least diffusion can be expressed as[3]

$$\delta_c = C_c\alpha\frac{\Delta E}{E_0},$$

where C_c is the constant of chromatic aberration of the lens and ΔE is the energy spread of the electron beam. This indicates that the size of an electron beam will increase linearly with the convergence semi-angle for a given energy spread. Finally, it is evident that there are conflicts between the three factors mentioned above. For example, a large convergence angle is always preferred to achieve a great STEM resolution according to the effect of diffraction. However, a large convergence semi-angle will increase the contribution of the spherical aberration exponentially. Practically, an optimum convergence semi-angle can be calculated by combining the first two factors and expressed as[3]

$$\alpha_{opt} = \left(\frac{4\lambda}{C_s}\right)^{1/4},$$

with a resolution ρ of

$$\rho = 0.43\sqrt[4]{C_s\lambda^3}.$$

It is evident that the spherical aberration can greatly affect the resolution of STEM imaging and the selection of the optimum convergence semi-angle of the electron beam. In reality, such theoretical resolution cannot be achieved because of the chromatic aberration and the higher-order aberrations, such as the fifth-order aberration.

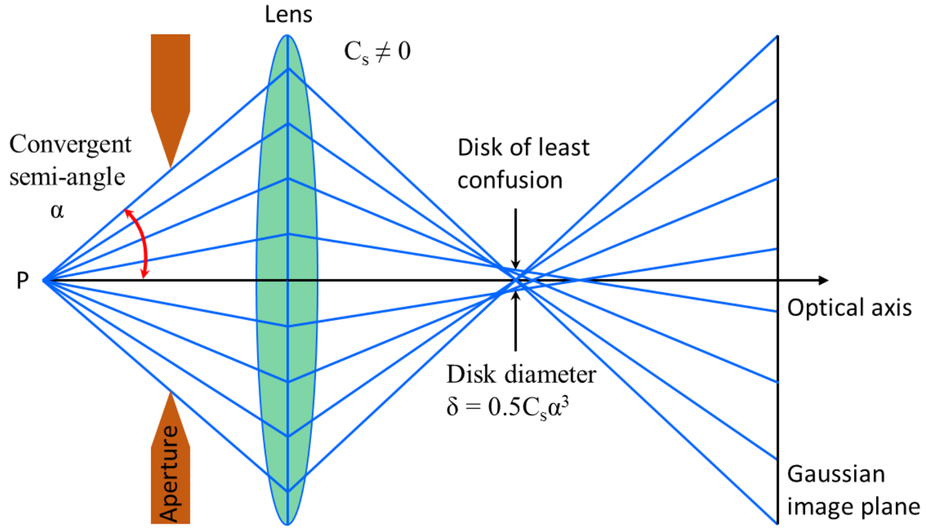

Figure 2.2. Schematic diagram showing the effect of the spherical aberration. A convergent electron beam is formed with the help of the lens, and its convergence semi-angle is controlled by using an aperture. The electron beam is then brought to a focus at the plane of a sample. Due to the spherical aberration of the lens, a small disk, rather than an infinitely small point, is formed near the back focal plane of the lens. The electron beam with the smallest diameter is called the disk of least confusion.

In this thesis, the *in situ* TEM characterization of 2D materials is performed using an aberration-corrected electron microscope JEOL JEM-ARM200F (Figure 2.3a). The microscope is equipped with a CEOS GmbH double-hexapole spherical-aberration corrector (CECOR). The lenses used in TEM are round lenses with positive spherical aberrations. In order to counterbalance this impact, a multi-pole lens, the so-called non-round lens, must be employed in the microscope.[4]

The first workable spherical aberration corrector with a series of quadrupole and hexapole was successfully built by Haider in 1998.[4] Figure 2.3b shows the image of a hexapole lens used in this aberration-corrected microscope.[5] The Zemlin-tableau method is employed to measure the aberrations of the lens with the tilted illumination to tune the corrector. Firstly, a series of micrographs with the tilted illumination in underfocus and overfocus conditions are recorded, respectively. Next, the size and shape of the electron probe at each focusing and tilting condition can be extracted using the deconvolution method. Each micrograph in the tilting series is compared with a reference micrograph acquired at the Gaussian focus under untilted illumination. Then, a list of the defocus and twofold astigmatism of each illumination condition can be obtained as a function of beam tilt. After that, the CEOS software will calculate a set of aberration coefficients that is in agreement with the tableau result. Lastly, the aberration coefficient that affects the resolution most can be identified and corrected automatically or manually. By repeating this procedure, an optimum electron probe with sub-Å resolution can be achieved once all the aberration coefficients are controlled within a certain range.

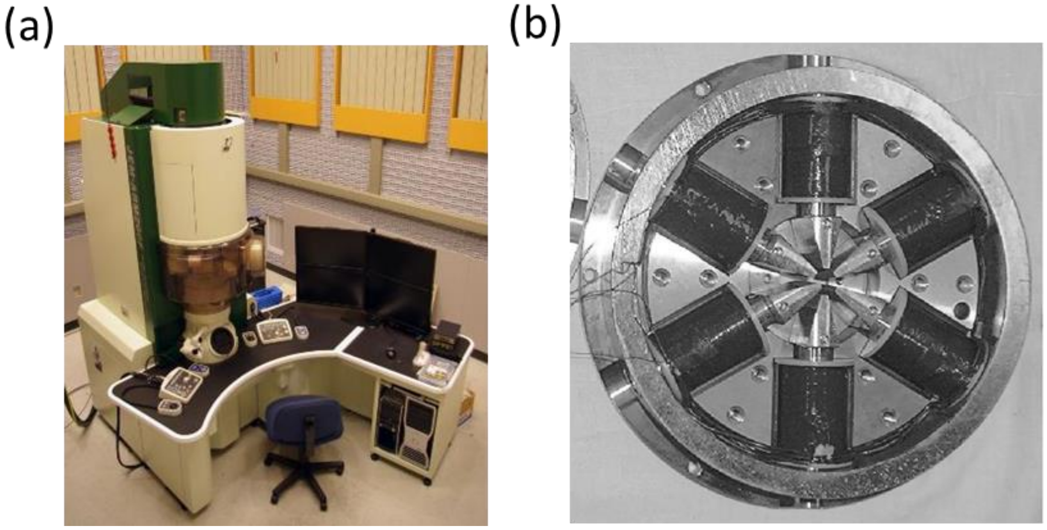

Figure 2.3. (a) Image of an aberration-corrected electron microscope JEOL JEM-ARM200F in UTD (b) Image of a hexapole lens in a spherical aberration corrector. Adapted with permission from ref (5) Copyright (1998) Elsevier B.V.

2.1.2 High-Angle Annular Dark-Field Imaging (HAADF)

Figure 2.4a shows the schematic diagram of a STEM imaging system with an ADF detector and a BF detector. To acquire an HAADF image, an annular dark-field (ADF) detector is used to collect the electrons scattered to a relatively high angle (~50-250 mrad). When the electron beam is scanned across the sample, a serial acquisition mode is applied to collect the signals collected by the ADF detector.

To understand the origins of contrast in HAADF imaging, one can start with the formation of a lattice image in TEM mode. In the conventional HR-TEM imaging, a sufficiently thin TEM specimen can be assumed as a phase object which can introduce a phase shift to a plane wave with a unity amplitude[1]

$$\varphi(\boldsymbol{R}) = e^{i\sigma V(\boldsymbol{R})},$$

where $\sigma = \pi/\lambda E$ is the interaction constant, λ is the wavelength, E is the accelerating voltage, V is the projected potential, and $\boldsymbol{R}$ is the position vector in the specimen. The additional phase shift from the lens aberrations can be expressed as χ as[1]

$$\chi(\boldsymbol{K}) = \pi(\Delta f\lambda\boldsymbol{K}^2 + \tfrac{1}{2}C_s\lambda^3\boldsymbol{K}^4),$$

where Δf is the defocus, C_s is the spherical aberration of the lens, and $\boldsymbol{K}$ is the transverse component of wavevector. $\chi(\boldsymbol{K})$ is called the contrast transfer function (CTF) in HR-TEM imaging. Thus the image intensity is the square of the convolution[1]

$$I(\boldsymbol{R}) = \left|\varphi(\boldsymbol{R})\otimes FT[e^{-i\chi(\boldsymbol{K})}]\right|^2,$$

where ⊗ denotes the convolution. This explains the origin of reverse contrast in TEM mode with the change of defocus. However, in HAADF-STEM imaging, one assumes that the specimen is illuminated by a coherently convergent electron beam. The wave function emerging from the phase object is [1]

$$\psi(\boldsymbol{R}, \boldsymbol{R_0}) = \varphi(\boldsymbol{R})P(\boldsymbol{R} - \boldsymbol{R_0}),$$

where $\boldsymbol{R_0}$ is the scan coordinate, and $P(\boldsymbol{R})$ is the probe amplitude distribution function, i.e., the Fourier transform of the phase changes due to the lens aberrations[1]

$$P(\boldsymbol{R}) = \int e^{2\pi i\boldsymbol{K}\cdot\boldsymbol{R}}e^{-i\chi(\boldsymbol{K})}d\boldsymbol{K} = FT[e^{-i\chi(\boldsymbol{K})}].$$

Thus the intensity of HAADF image at the scan position $\boldsymbol{R_0}$ is [1]

$$I(\boldsymbol{R_0}) = |\varphi(\boldsymbol{R_0})|^2 \otimes |P(\boldsymbol{R_0})|^2.$$

The equation indicates that the HAADF image is the convolution between the square of the object function and the square of probe amplitude function. It is easy to find out that there is no reverse contrast with the change of focus for a HAADF image. This is different from the HR-TEM image.

In addition, HAADF image intensity is monotonically dependent on the sample thickness. The HAADF image is also called “Z-contrast” image, indicating that the image intensity is proportional to the nth power of the atomic number Z. The origin of Z-related intensity is caused by the different scattering ability of an electron been scattered by a light element or heavy element. For example, the heavy element (Au, Pt, Cu, etc.) has a larger differential cross-section than the light element (C, N, O, etc.), so that the probability of an electron been scattered to a high angle by a heavy atom is much higher than that by a light element. As a result, the ADF detector can collect more scattered electrons when the electron beam is scanned at the position with more heavy elements. Thus, for a given specimen thickness, the region with heavy element shows a bright contrast while the region with light element shows a bright contrast. Therefore, this technique is exceptionally useful for the characterization of the element distribution in the specimen. In addition, the electrons scattered to high angles are mainly thermal diffuse scattering (TDS) electrons. Therefore, HAADF imaging is an incoherent imaging technique with a minimum diffraction effect.

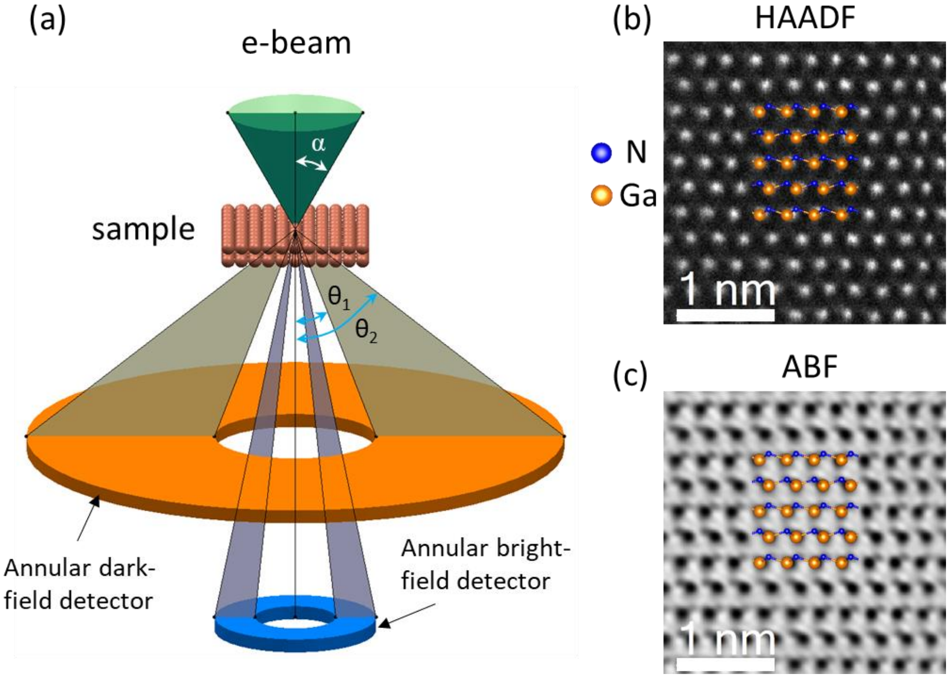

Figure 2.4. (a) Schematic diagram showing a STEM configuration with an annular dark-field detector and annular bright-field detector. The convergent semi-angle of the electron probe and the collection semi-angle of the ADF detector are α and θ, respectively. (b) Atomic resolution HAADF image of a GaN thin film grown by the MBE method. (c) Atomic resolution ABF image in the same region. Ga atoms can be seen clearly in the HAADF image. As a comparison, both Ga and N atoms can be identified in the ABF image.

2.1.3 Annular Bright-Field Imaging (ABF)

Apart from the HAADF image, a BF image can also be acquired simultaneously by collecting the electrons in the forward scattered beam with a circular bright-field (BF) detector. The BF image intensity is similar to the phase contrast image in TEM mode. Recently, a new annular bright-field (ABF) STEM imaging technique is developed to identify the presence of light elements in the specimen. Similar to the BF-STEM imaging, it also collects the forward scattered electrons using the BF detector, except the central part of the direct beam. In JEM-ARM200F, ABF-STEM imaging is carried out in two steps. Firstly, a beam stopper is used to block the central part of the BF detector, so that the transmitted electrons which do not suffer any scattering or undergo a very small scattering cannot be collected by the BF detector. Secondly, a 3 mm STEM BF aperture is inserted to block the electrons scattered at larger angles. Finally, the collection semi-angle of the electron probe is limited to a specific range (12 to 24 mrad). When the electron beam is positioned at the atomic columns of a light element, the electrons in the incident beam tend to propagate along the atomic column due to the channeling effect.[2] However, these electrons are blocked by the beam stopper, resulting in a smaller quantity of electrons that can be collected by the BF detector. Therefore, the light-element atomic columns are imaged as dark spots in ABF mode. On the contrary, when the electron beam is positioned on a heavy atomic column, there are more electrons scattered at high angles outside of the BF detector than the electrons that can be collected by the BF detector. As a result, the heavy-element atomic columns are also imaged as dark spots. Thus, both the light element and the heavy element in the specimen can be observed by ABF-STEM imaging. Moreover, ABF and HAADF imaging can be performed simultaneously, so information on heavy elements and light elements can be obtained using the HAADF and ABF images, respectively. Figure 2.4b shows an atomic resolution HAADF image of a GaN specimen in which only Ga atomic columns are displayed as bright spots. However, in Figure 2.4c, both Ga atomic columns and N atomic columns are shown as dark spots in the ABF image. Thus, the polarity of GaN can be easily identified as N-terminated.

2.1.4 Electron Energy Loss Spectroscopy (EELS)

The EELS technique allows us to analyze the energy distribution of the transmitted electrons passing through a TEM specimen. Figure 2.5 is the schematic of an incident electron beam scattered by a thin specimen. As the electrons pass through the specimen, a wide range of signals are generated due to the electron-matter interactions, including the transmitted electrons that leave the sample without scattering and can be collected by a BF detector, the elastically scattered electrons that leave the sample at high angles and can be collected by an ADF detector, the inelastically scattered electrons that loss some amount of energy, and the characteristic X-rays induced by the electron excitations in the sample. A fraction of the incident electrons may undergo inelastic scattering and lose some energy as they interact with the specimen. Simultaneously, the energy transferred to the specimen may provoke the electronic excitations in the specimen. Therefore, the characteristic X-rays can be generated when the excited atoms in the specimen fall back to the ground states. By analyzing the inelastic electrons and the characteristic X-rays, the chemical and compositional information of the specimen can thus be identified and quantified.[1-2]

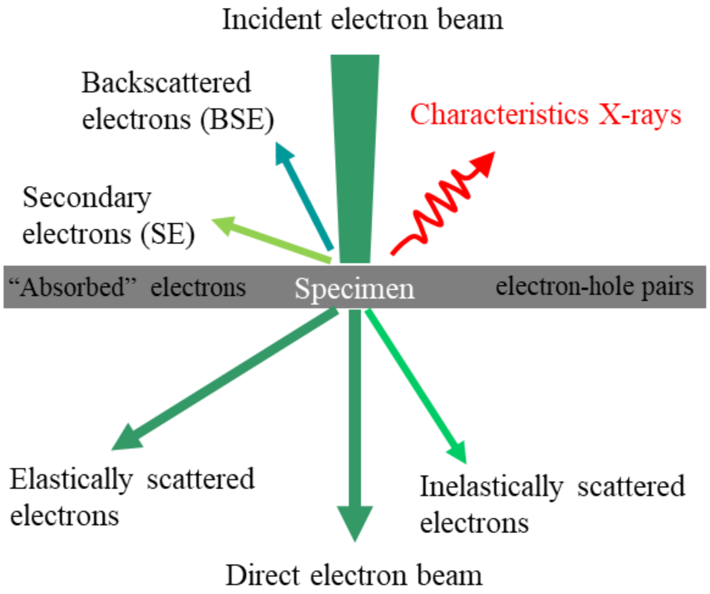

Figure 2.5. Schematic of the incident electron beam passing through an electron transparent specimen. A variety of signals are generated when the electrons pass through the specimen, including the backscattered and forward scattered electrons. For a thin TEM specimen, the majority of electrons will pass through the specimen without any interaction, to form the transmitted beam. The forward scattered electrons can be used for imaging and spectrum analysis. The characteristics X-rays and the inelastically scattered electrons can be used for the chemical information analysis.

An EELS spectrometer is an instrument designed to detect and analyze the inelastic electrons passing through the sample, including the plasmon excitations (5-30 eV) and the core-loss excitations (a hundred to a few thousand eV).[6] With the advance of the EELS instrument, especially the improvement of the chromatic aberration correction and the development of the fast cameras, the sub-eV energy resolution and high collection efficiency make EELS an ideal technique for the material characterization. In this research, EELS analysis is performed using a Gatan Enfina spectrometer mounted below the electron microscope.

Figure 2.6a shows a schematic of an EELS spectrometer attached to a STEM system. During the HAADF image acquisition, the scattered electrons passing through the ADF detector are collected simultaneously by the EELS spectrometer. These inelastically scattered electrons are emitted from the small volume in the specimen with the electron beam illumination. Thus, the chemical information extracted from EELS indicates the localized information in the specimen. Due to the serial acquisition mode of STEM imaging, each EEL spectra can be directly linked to the position of the electron beam on the specimen, enabling the spatially resolved distribution of EELS analysis. This site-specific analysis method is called spectrum imaging (SI).[6] A data cube is used to store the three-dimensional data that contains the spatial and spectral information in DigitalMicrograph® software (Gatan, Inc.). Figure 2.6b shows the schematic of how to perform the SI analysis using EELS. The element distribution in the specimen can be highlighted by selecting a specific range of energy in the spectrum. With the development of the aberration-corrected electron microscope, and the fast EELS/EDS spectrometer, the site-specific spectrum analysis is of great advantage over the other TEM techniques, enabling the analysis of the structure and composition of material at the atomic scale. For example, single atom identification can be achieved by the quantitative analysis of HAADF imaging and EELS.[7]

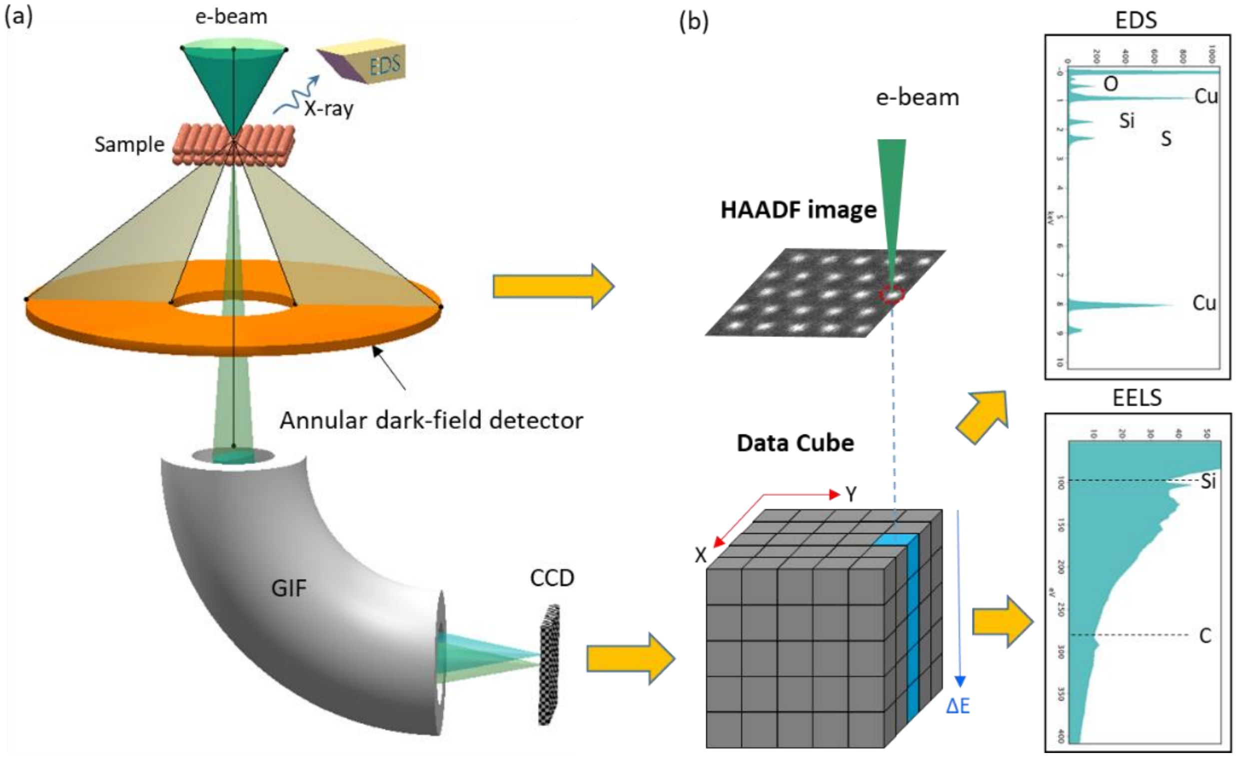

Figure 2.6. (a) Schematic of STEM spectrum imaging using EELS and EDS. During the HAADF image acquisition, the inelastically scattered electrons and the characteristic X-rays can be collected by an EELS spectrometer and an EDS detector, respectively. (b) Schematic of how to perform a spectrum imaging. In a data cube, two of the cube axes correspond to spatial information (X, Y), while the third dimension is for the EELS or EDS spectrum.

2.2 *In Situ* TEM Characterization

In situ TEM characterization is a type of experiment used to investigate a phenomenon without altering the original condition in an electron microscope. Real-time observations can be performed simultaneously under external stimuli, such as an electrical biasing, an applied force, or the change of temperature.[8] The chemical reaction details, which are difficult to be detected in conventional

TEM, can be easily observed without changing the reaction parameter. Therefore, the mechanism or key factor can be comprehensively explored and identified. In brief, *in situ* TEM characterization can be categorized into two types, either using a modified electron microscope that can engage gases to the specimen, or using a customized specimen holder to apply the external stimuli to the specimen.[8] In this research, all the *in situ* TEM characterization is carried out using the second route.

To study the defect dynamic and phase transition in 2D materials, three kinds of *in situ* TEM characterizations are performed: (1) *in situ* observation of the phase transition in $MoTe_2$ and other TMDs under the vacuum annealing; (2) *in situ* observation of phase transition in $MoTe_2$ under the electrical biasing; (3) *in situ* observation of defect dynamics in 2D materials under the electron beam illumination. The first and second observations are performed using a customized TEM holder, and the technical details are described in section 2.2.1. The third observation can be performed using a traditional TEM holder so that the experiment details will be discussed in the study of 2D materials.

2.2.1 *In Situ* Heating and Electrical Biasing

In situ heating and electrical biasing experiments are all performed with a Protochips Aduro™ 350 system.[9] It includes a customized double tilt TEM holder, an external power supply, a controller with software and cables, and the MEMS-based E-Chips. As shown in Figure 2.7a-b, the current or voltage from the controller can be applied to the E-Chips via four electrodes on the holder. Protochips holder is a multifunction platform that uses the flexibility of MEMS-based E-chips. Figure 2.7c-e show three types of E-Chips to perform the heating, electrical biasing, and electrical-and-heating experiment, respectively. For the heating E-Chip (Figure 2.7c), a current is applied between electrodes 1 and 4, so that localized heating of the ceramic SiC film is carried out using the joule-heating. In the window region, SiC film is etched to form nine holes (3x3 array). A 20 nm SiN film positioned below the SiC film is used to support the TEM specimen. There are two advantages of the MEMS-based heating holder over the traditional heating holder: the fast temperature ramp rate (1000 °C/ms) and the small thermal drift (0.5 nm/minute). Due to the small heating region, the thermal drift can be controlled pretty well, so that atomic resolution STEM imaging can be performed at a high temperature. Figure 2.7d shows the image of FIB optimized E-Chip for the electrical biasing experiment. The specimen is mounted between electrodes 1 and 4 so that the current or voltage through the specimen can be applied or measured using the two-wire mode. If needed, electrodes 2 and 3 can also be connected to the specimen, facilitating the four-wire measuring mode. The specimen preparation for the electrical biasing is discussed in section 2.3.4 in detail. Figure 2.7e shows the schematic of E-Chips, which can perform heating and electrical biasing simultaneously. The specimen heating is achieved using joule-heating vis electrodes 1 and 4, while the current or voltage is applied or measured via electrodes 2 and 3.

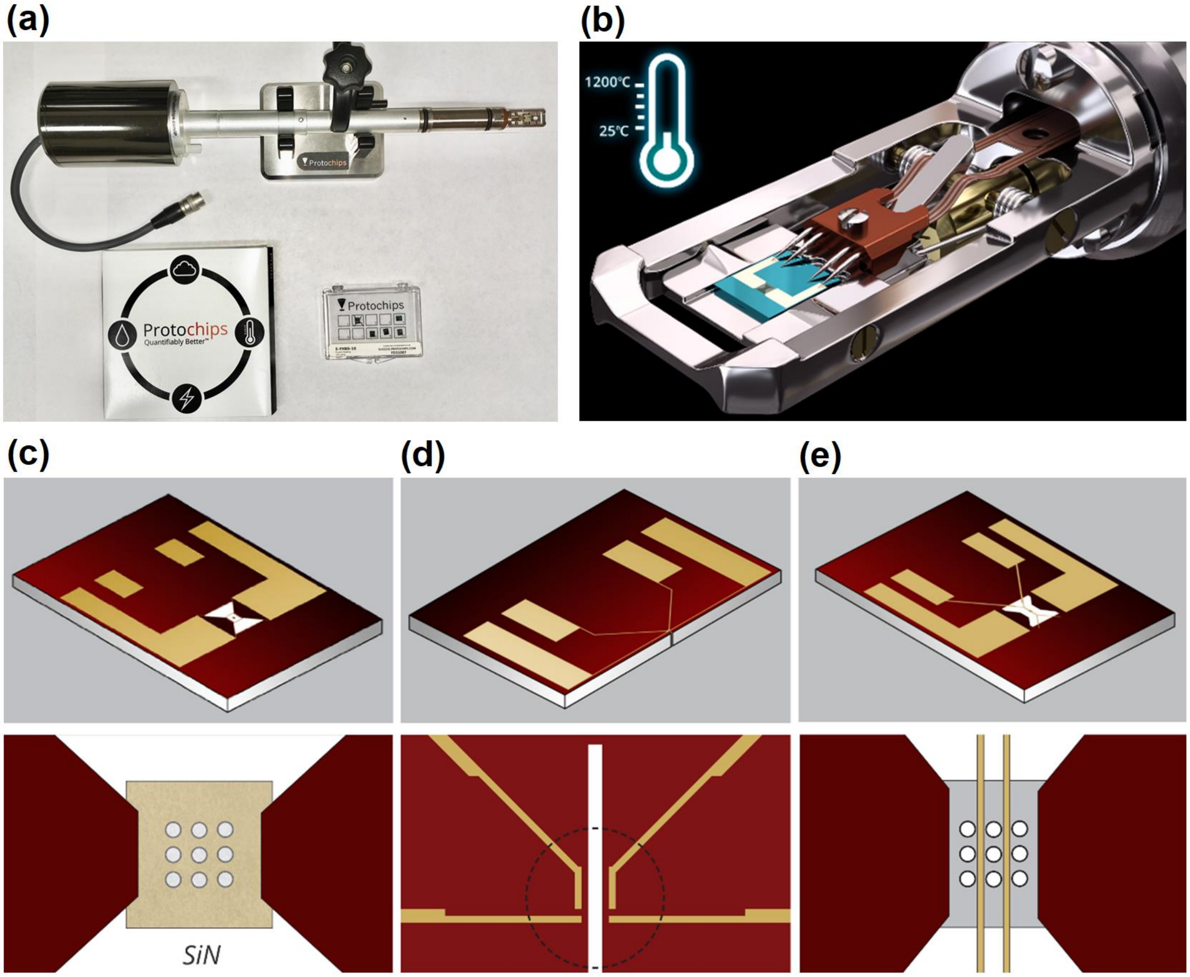

Figure 2.7. (a) Protochips *in situ* holder (b) Zoom-in of the holder head (c-e) Schematic of thermal E-Chip, FIB optimized electrical biasing E-Chip, and electro-heating E-Chip, respectively. Figures adapted from ref (9).

2.3 Specimen Preparation

This section describes the specimen preparation for the 2D materials research. Toward that end, it is divided into three sub-sections. Section 2.3.1 describes the materials used in the research. Section 2.3.2 introduces the focused ion beam. Section 2.3.3 and 2.3.4 describe the flake exfoliation and transfer for *in situ* heating experiments, and *in situ* electrical biasing experiments, respectively.

2.3.1 Materials

The MoTe2 crystals used in this work are chemical vapor synthesized (HQ Graphene) using high purity molybdenum (99.9975%, Alfa Aesar) and tellurium (99.999%, Alfa Aesar) powders with Te vapor as a transport agent. 10 at. % more Te above the initial Te: Mo = 2:1 were added in the crystal growth process to avoid a Te deficiency and thus a more reactive surface to air exposure. Fresh sample surfaces are simply cleaved in air with Scotch® tape and then immediately loaded into an ultrahigh vacuum (UHV) system (base pressure ~10-10 mbar) for the subsequent surface characterization and heating studies.

2.3.2 Focused Ion Beam

Focused ion beam (FIB) is a technique used particularly in the semiconductor industry and materials science, owing to its enormous advantage for the site-specific analysis, imaging, milling, deposition, and manipulation. A FEI Dual Beam Nova 200 focused ion beam system is used for the specimen preparation in this research, as shown in Figure 2.8. It consists of an ultra-high-resolution field emission scanning electron microscope (SEM), a focused ion beam using Ga^+ ions, and a gas injection system for the deposition of platinum (Pt), carbon, and silicon oxide. Additionally, it is also equipped with a high precision nanoscale manipulator, the OmniProbe 400 (Oxford Instruments), which can be used for the specimen transfer and manipulation during the *in situ* lift-out procedure. In this thesis, the FIB technique has been used during the characterization of 2D materials, such as the morphology inspection, TEM specimen fabrication, and the manipulation and transfer of 2D flakes to the *in situ* TEM grid for *in situ* TEM characterization.

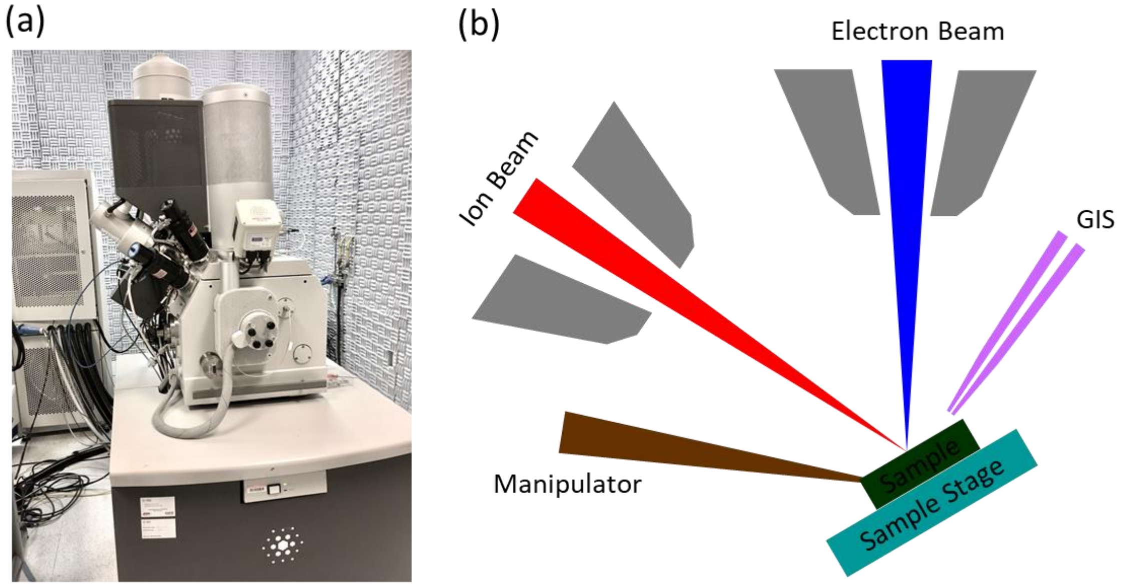

Figure 2.8. (a) FEI Dual Beam Nova 200 (b) Schematic of a FIB system, including an electron beam for imaging, an ion beam for milling, a gas injection system for deposition, and a manipulator for sample lift-out.

2.3.3 Flake Transfer for *In Situ* Heating Characterization

Originated from the graphene study, the mechanical exfoliation method, which is also called "Scotch Tape Method," is widely used in 2D materials research. In a layered material, the weak van der Waals interactions between the neighboring layers make it possible to exfoliate the atomically thin flake from the bulk crystal.[10] There are some undesired issues of this method, such as the small size of the flake, low yield, poor thickness control, and the removal of polymer residue. However, the discernible advantages of this method, such as easy operation, low cost, high quality of 2D flake, easy fabrication of the heterojunctions, make it an important and extensively used method during 2D materials research.

To perform *in situ* TEM characterization, the atomically thin 2D flakes need to be transferred to the *in situ* TEM grid, i.e., the Protochips heating or electrical biasing E-Chips. In this research, the specimen preparation is slightly different between *in situ* heating experiment and *in situ* electrical biasing experiment. For *in situ* heating experiments, the atomically thin flake is prepared using the mechanical exfoliation method, followed by the flake transfer to a heating grid using the polymer-assisted wet transfer method.[11] On the other side, the specimen preparation for *in situ* electrical biasing experiments is carried using a modified Au-assisted mechanical exfoliation method, followed by the flake transfer and TEM lamella fabrication using FIB (see section 2.3.4).

The flake transfer for *in situ* heating experiments is carried out using a customized flake transfer system, including an optical microscope with a long working distance objective lens, an XYR stage to support E-Chip, an XYZ stage with a glass slide to manipulate the position of flake, and a heating plate mounted on the XYR stage and controlled using a PID controller. Figure 2.9 shows the customized flake transfer system and its corresponding schematic, respectively.

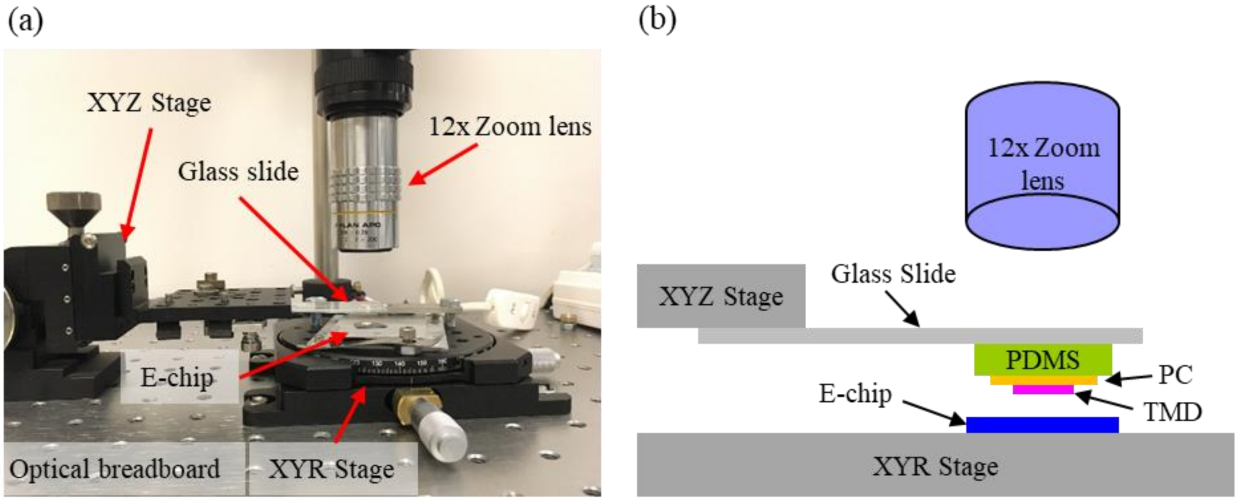

Figure 2.9. (a) The customized flake transfer system. (b) Schematic diagram of the flake transfer system.

Figure 2.10 shows the transfer of a bilayer $MoTe_2$ flake to a Protochips thermal E-Chip. Prior to the flake transfer, FIB is used to fabricate some holes about 800nm in diameter on the SiN film of the E-Chip. As illustrated in Figure 2.10a, the transfer of the $MoTe_2$ flake can be carried out in the following steps. Firstly, a $MoTe_2$ is exfoliated onto a 300 nm SiO_2/Si substrate using the scotch tape method and inspected with an optical microscope. Secondly, after the spin coating of a poly-bisphenol A carbonate (PC) film on the Si substrate, a PDMS stamp is used to cover the Si substrate and pick up the $MoTe_2$ flake in water. Thirdly, the PDMS stamp is attached to a glass slide with the $MoTe_2$ flake facing down and manipulated with the help of an XYZ stage. By manipulating the position of E-Chip using an XYR stage, the $MoTe_2$ flake can be attached to the window of E-Chip. Once done, E-Chip is heated to 110 °C to increase the adhesion between the flake and the E-Chip by reducing the number of air bubbles under the flake. More importantly, the adhesion between the PC film and PDMS stamp can be reduced to such an extent that they can be separated by lifting the glass slide using the stage. Lastly, a $MoTe_2$ flake is successfully transferred to the E-Chip after PC dissolving in the chloroform. The thermal E-Chips with the bilayer $MoTe_2$ flake can then be mounted on the Protochips holder for *in situ* heating study.

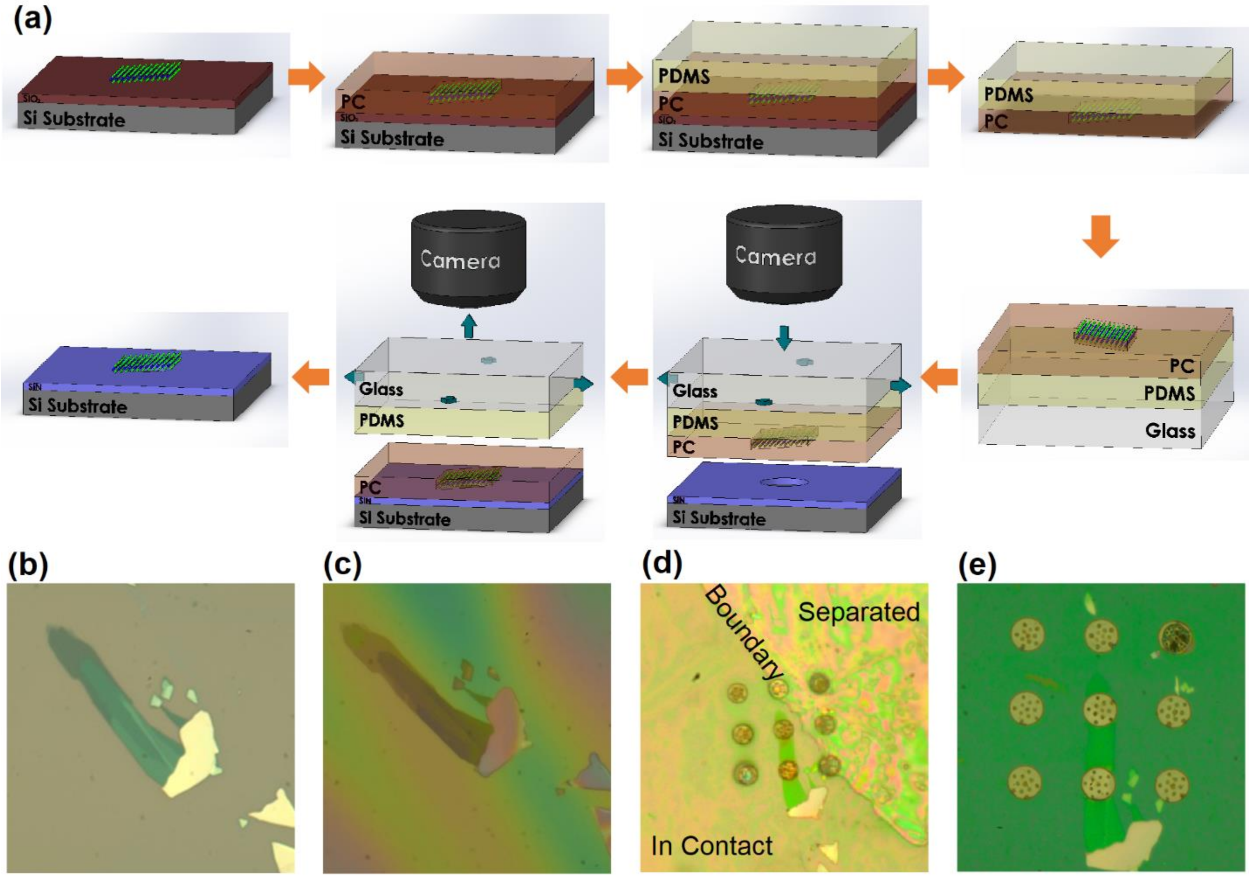

Figure 2.10. $MoTe_2$ flake transfer for *in situ* heating experiment. (a) Schematic illustration of a $MoTe_2$ flake transfer to a MEMS-based thermal E-Chip. (b-c) Optical image of a bilayer $MoTe_2$ flake on a silicon substrate and after PC spin coating, respectively. (d) $MoTe_2$ flake partially attached to E-Chip. The colorful contrast from the separated region indicates the gap between PDMS stamp and SiN film, while the clear contrast from the In Contact region suggests that the $MoTe_2$ flake is fully contacted with SiN film. (e) $MoTe_2$ flake successfully transferred onto the *in situ* TEM grid.

2.3.4 Flake Transfer for *In Situ* Electrical Characterization

In order to perform the *in situ* electrical biasing characterizations of $MoTe_2$, an Au/$MoTe_2$/Au sandwich structure needs to be fabricated prior to the flake transfer to electrical E-Chip. Figure 2.11a shows the schematic of the fabrication procedure. First of all, 50 nm Au is sputtered on a bulk $MoTe_2$ with a fresh surface. Next, a thermal release tape (TRT) is applied to the bulk crystal.

Due to the strong adhesion between Au and $MoTe_2$, a $MoTe_2$/Au/TRT structure is achieved when TRT is peeled off. Then another 50-100 nm Au is sputtered onto the fresh surface of $MoTe_2$ flake to form an Au/$MoTe_2$/Au sandwich structure. After that, the TRT is stamped to a heavily doped Si substrate with Au and Cr coating. Finally, by putting the Si substrate with TRT on a hot plate (~120 °C) for a few seconds, TRT and Au will be separated due to the reduced adhesion. Figure 2.11b-c shows the optical image of $MoTe_2$ before and after the 2nd Au coating, respectively.

The transfer of the as-prepared Au/$MoTe_2$/Au structure is performed using a FIB. Firstly, the target $MoTe_2$ flake with a suitable thickness is identified with the help of the optical image. Next, a TEM lamella is prepared and transferred to a FIB optimized Protochips electrical E-Chip (Figure 2.11d). After that, a 100 nm thick lamella with a width of 3 um is fabricated with the 30 kV Ga^+ ion beam. Finally, the lamella is carefully milled using the ion beam so that a Pt/Au/$MoTe_2$/Au/Cr/Si structure is isolated (Figure 2.11e-f). When a current is applied to the electrodes 1 and 2 of the E-Chip, it can only flow through the Au/$MoTe_2$/Au sandwich structure. Figure 2.11g shows one advantage of this transfer method. If the electrical measurement at the first position is completed, a second or even a third position can be used for the electrical biasing testing.

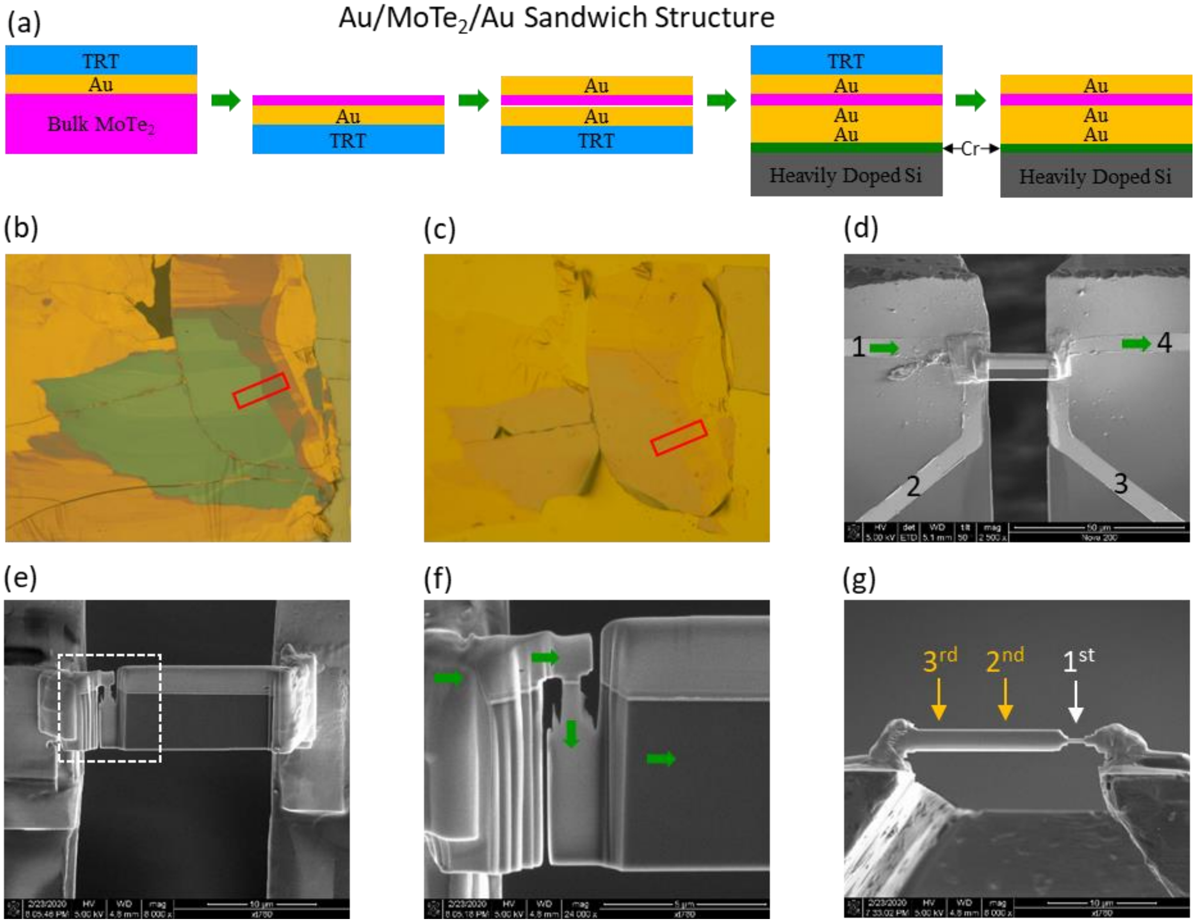

Figure 2.11. MoTe$_2$ flake transfer and TEM lamella fabrication for *in situ* electrical biasing experiments. (a) Schematic of the fabrication of Au/MoTe$_2$/Au sandwich structure. (b-c) Optical image of MoTe$_2$/Au/TRT and Au/MoTe$_2$/Au structure, respectively. (d) SEM image of the MoTe$_2$ flake transferred on Protochips electrical biasing E-Chip. Current or Voltage can be applied or measured through electrodes 1 and 4. (e-f) TEM lamella for the electrical biasing experiment. Isolation is performed using FIB in order that the current can flow across the Au/MoTe$_2$/Au structure. (g) Top view of the TEM lamella. Once the electrical measurement is completed at the 1st position, the flake can be thinned and isolated at the nearby region, so that a 2nd or 3rd position can be used for more electrical measurements.

2.4 *In Situ* Scanning Tunneling Microscopy (STM)

STM is an analytical technique that probes the geometric and electronic properties of sample surface at the atomic level. Figure 2.12 shows a schematic of STM system.[12-13] The components of a STM include a scanning tip, a piezoelectric controlled scanner, the control electronics (scan generator, current amplifier, high-voltage amplifier, feedback), and the vibration isolation system. The tip is mounted on a piezo-scanner and can scan over the sample surface in the x-y plane, and z-direction, independently. The principle of STM is based on the quantum mechanical tunneling effect.[14] When an atomically sharp and conductive tip approaches a conducting or semiconducting surface at a distance of approximately several angstroms, the wave functions of the tip may overlap with those of the sample. After applying a bias voltage between the tip and sample, electrons begin to "tunnel" through the vacuum between them, despite the fact that they are not in contact. The tunneling current is an exponential function of the tip-sample distance. Therefore, the remarkable sensitivity of the tunneling current with respect to the tip-sample distance can be measured and used to characterize the sample surface with sub-angstrom precision vertically.

There are two operation modes of STM, i.e., constant current mode and constant height mode, respectively. In constant current mode, the tunneling current, and hence the tip-sample distance, is held constant when the tip moves across the sample surface. Thus, the variation of sample surface is directly related to the changes of tip height. Therefore, the changes of tip height are recorded and mapped as a false-color image to represent the surface topography. In constant height mode, the bias voltage and tip height are both held constant while the tunneling current is measured when the tip is scanned over the sample surface. The spectroscopic measurements of the differential conductance dI/dV for a fixed bias voltage are measured and false-color plotted in a two-dimensional image to represent the changes of local density of electronic states (LDOS) of the sample surface. However, the as acquired data contain dI/dV information only for a specific bias voltage. A special STM technique, the so-called scanning tunneling spectroscopy (STS), can be used to obtain comprehensive spectroscopic information of a specific location. In brief, the tip is placed above a particular place on the sample, with the tip height fixed. The tunneling current is measured by sweeping the bias voltage. Thus, the spectroscopic information, i.e., the LDOS of the sample can be displayed using the dI/dV curve.

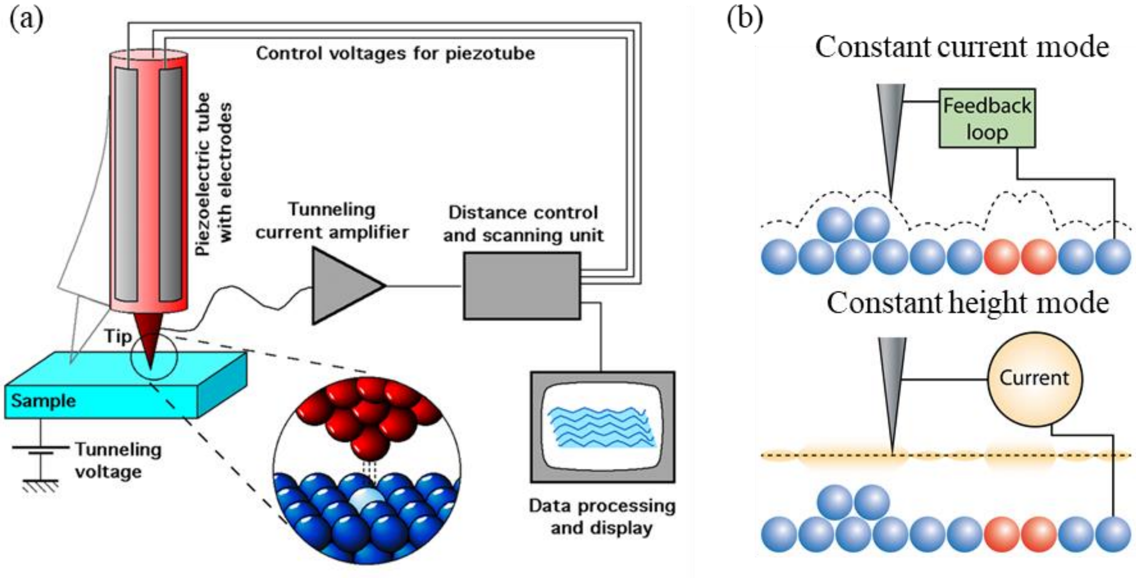

Figure 2.12. (a) Schematic of a STM system. Adapted from ref (12). (b) STM tip operating in the constant current mode and constant height mode, respectively. Adapted from ref (13).

In this research, *in situ* STM characterization of $MoTe_2$ is carried using the Omicron variable temperature STM, which is integrated in an *in situ* UHV system. Firstly, a bulk $MoTe_2$ crystal with a fresh surface is loaded into the analysis chamber in the UHV system for STM characterization. Then the sample is *in situ* transferred to a prep chamber for heating treatment. After that, the sample is transferred back to the analysis chamber for another STM characterization. By repeating this procedure, the surface morphologies of $MoTe_2$ from RT to 450 are systematically studied by STM analysis.

2.5 References

1. Pennycook, S. J.; Nellist, P. D., *Scanning transmission electron microscopy: imaging and analysis*. Springer Science & Business Media: **2011**.

2. Carter, C. B.; Williams, D. B., *Transmission electron microscopy: Diffraction, imaging, and spectrometry*. Springer: **2016**.

3. Erni, R., *Aberration-corrected imaging in transmission electron microscopy: An introduction*. World Scientific: **2010**.

4. Haider, M.; Rose, H.; Uhlemann, S.; Schwan, E.; Kabius, B.; Urban, K., A spherical-aberration-corrected 200kV transmission electron microscope. *Ultramicroscopy* **1998,** *75* (1), 53-60.

5. Müller, H.; Uhlemann, S.; Hartel, P.; Haider, M., Advancing the hexapole C s-corrector for the scanning transmission electron microscope. *Microscopy and Microanalysis* **2006,** *12* (6), 442-455.

6. Egerton, R. F., *Electron energy-loss spectroscopy in the electron microscope*. Springer Science & Business Media: **2011**.

7. Senga, R.; Suenaga, K., Single-atom detection of light elements: Imaging or spectroscopy? *Ultramicroscopy* **2017,** *180*, 150-155.

8. Luo, C.; Wang, C.; Wu, X.; Zhang, J.; Chu, J., In Situ Transmission Electron Microscopy Characterization and Manipulation of Two-Dimensional Layered Materials beyond Graphene. *Small* **2017,** *13* (35), 1604259.

9. Protochips, www.protochips.com.

10. Geim, A. K.; Novoselov, K. S., The rise of graphene. *Nature Materials* **2007,** *6*, 183-191.

11. Lin, J.; Lin, Y.-C.; Wang, X.; Xie, L.; Suenaga, K., Gentle transfer method for water- and acid/alkali-sensitive 2D materials for (S)TEM study. *APL Materials* **2016,** *4* (11), 116108.

12. Schmid, M., https://en.wikipedia.org/wiki/Scanning_tunneling_microscope.

13. Murphy, B. E. The physico-chemical properties of fullerenes and porphyrin derivatives deposited on conducting surfaces, Thesis. Trinity College Dublin, **2014**.

14. Güntherodt, H.-J.; Wiesendanger, R., *Scanning tunneling microscopy I: general principles and applications to clean and adsorbate-covered surfaces*. Springer: **1992**.

CHAPTER 3

IN SITU HEATING STUDY OF 2H-MOTE$_2$ TO MO$_6$TE$_6$ NANOWIRE PHASE TRANSITION

3.1 Preface

This chapter is adapted with permission from a publication "**New Mo$_6$Te$_6$ Sub-Nanometer-Diameter Phase from 2H-MoTe$_2$**" [Advanced Materials, 2017, 29, pp 1606264]. Copyright 2017, WILEY-VCH Verlag GmhH & Co. KGaA, Weinheim. The authors are Hui Zhu, Qingxiao Wang, Chenxi Zhang, Rafik Addou, Kyeongjae Cho, Robert M. Wallace*, and Moon J. Kim*. In this work, my contribution was in planning and performing the *in situ* TEM characterization, analyzing the corresponding data, and writing the manuscript. Hui Zhu is the coauthor of this research under the supervision of Prof. R. Wallace and contributes equally to this work, including the design of surface analysis related experiments (*in situ* STM, XPS, Raman), and writing the manuscript. The theoretical calculations by first-principles density functional theory (DFT) were performed by Dr. Chenxi Zhang under the supervision of Prof. K. Cho.

3.2 Introduction

Recently, two-dimensional (2D) nanomaterials, in particular graphene and transitional-metal dichalcogenides (TMDs), have attracted tremendous research interest because of novel electronic, optical, and mechanical properties associated with their atomically thin nature, van der Waals (vdW) interactions, and wide range of band gaps/band alignments.[1-4] TMDs, with a general formula of MX$_2$ (M = Mo and W, X = S, Se, and Te) and polymorphs, including the semiconducting hexagonal (2H), the metallic octahedral (1T), and the semi-metallic distorted octahedral (1T’) phases. As noted in the literature, the semiconducting-metal phase transition among polymorphs provides an appealing phase engineering alternative strategy for atomically thin nanoelectronics and optoelectronic device applications, when compared to the traditional chemical doping of contact regions to lower the contact resistance.[1-2, 5-10]

The ability to fabricate lateral/vertical metal-semiconductor heterojunctions with trap free interfaces is highly desirable to reduce the interfacial scattering, and hence to reduce contact resistance. Though the synthesis of heterojunctions is still not mature enough for contact purposes, methods of selective phase engineering, such as chemical (intercalation) doping to form the 1T phase in MoS_2, and charge/strain/defect engineering to form 1T’ phase in $MoTe_2$ are being developed.[5-6, 9-10] Despite these efforts, the metastable 1T or 1T’ phases are likely an obstacle for their applications.[11]

One-dimensional (1D), metallic M-X nanowires (NWs) with unique structures and intrinsic anisotropic metallic properties remain to be developed as an important complementary building block for nanodevices.[12-13] Recently, an isolated, nanometer-length M_6X_6 NW (X = S and Se) has been fabricated forming a “self-adapted” junction with MX_2 monolayers using electron-beam irradiation methods.[14-17] Such a top-down, subtractive fabrication method requires a precise beam control, relies on irradiation removal of MX_2 regions, and may limit its practical application for nanodevices.

We present an alternative strategy for long, stable metallic Mo_6Te_6-NW formation not previously reported through the annealing of 2H-$MoTe_2$ crystals (≈ 15-20 layers thick) under vacuum. The associated phase transition temperature (400-500 °C) is amenable to device integration, and the length of NWs can be in the micrometer range. Importantly, the NWs are thermally stable upon reannealing to 450 °C after the initial formation and stable for long storage times. We not only demonstrate that this type of phase transition exhibits an atomically sharp interface between the 2H-$MoTe_2$ and metallic Mo_6Te_6-NW-bundles, but also show from band bending behavior that such NWs may exhibit a hole injection effect due to band alignment with the 2H-$MoTe_2$. Finally, in contrast to previous reports,[18-23] this NW phase formation is observed within the bulk of layered $MoTe_2$ and does not require the introduction of a ternary intercalant species.

3.3 Experimental Section

3.3.1 STEM Specimen Preparation and Characterization

(1) Plan-view specimen preparation:

A $MoTe_2$ thin flake was exfoliated from bulk 2H-$MoTe_2$ crystals (HQ Graphene), which were also used in Scanning tunneling microscopy (STM)/ X-ray photoelectron spectroscopy (XPS) studies, with scotch tape[24] and then transferred onto a Quantifoil TEM grid by the dry transfer method. In the next step, the TEM grid with the $MoTe_2$ flake was loaded in FEI Dual Beam Nova 200 FIB, and the $MoTe_2$ flake was transferred to a Protochips thermal E-chips using our mask assisted method for *in situ* heating studies (Figure 3.1).

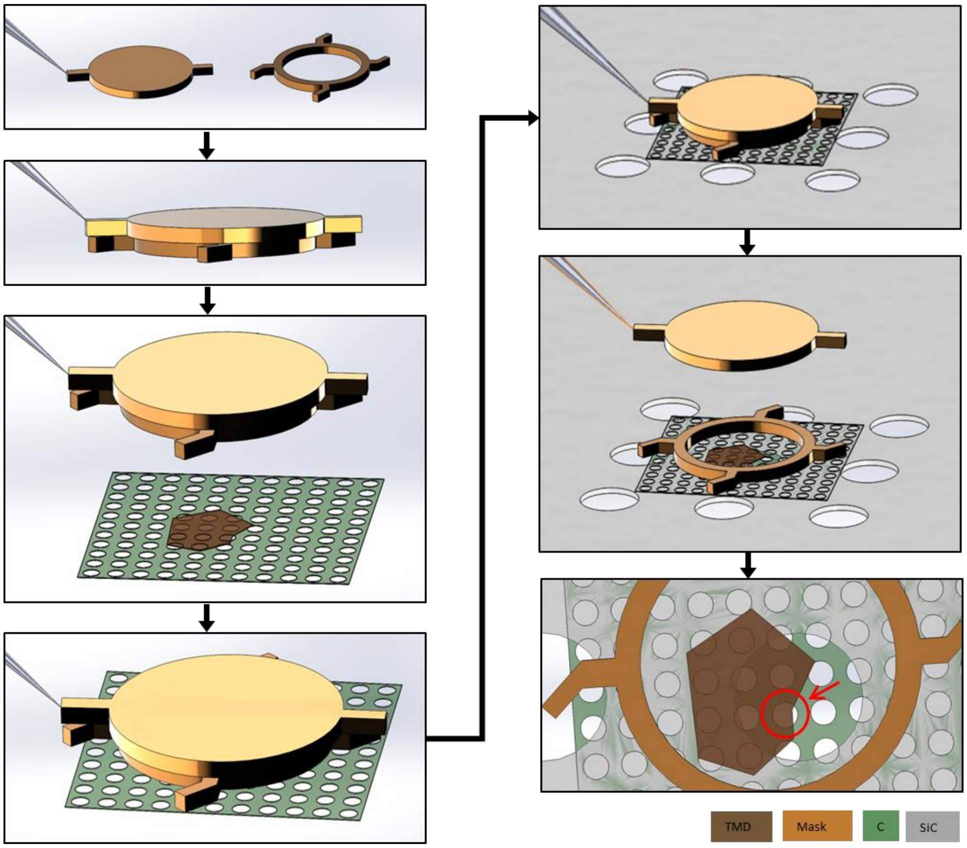

Figure 3.1. Schematic of the FIB assisted $MoTe_2$ flake transfer. Two masks are fabricated using a FIB and manipulated to cover the target $MoTe_2$ flake on a Quantifoil TEM grid. The flake is then transferred onto a Protochips thermal E-Chip, followed by the removal of the upper mask.

(2) Cross-Section specimen preparation of the plan-view specimen after heating:

In order to study the cross-section morphology of the plan-view specimen after heating, we prepared two STEM cross-section lamellas at two selected positions: one across the nanowire bundles and the other along the nanowire bundles growth direction, respectively. Prior to ion beam milling, the specimen surface is protected by e-beam assisted carbon deposition followed by SiO_2 and Pt deposition on the region of interest. The routine TEM lamella preparation method and *in situ* lift-out (ISLO) method[25] have been applied to transfer the STEM specimen onto an Omniprobe TEM grid for TEM study.

(3) Cross-Section specimen preparation for *in situ* heating study:

We used electron beam assisted SiO_2 and Pt deposition on the bulk $MoTe_2$ surface, then used the routine TEM specimen preparation method to prepare a lamella specimen down to ~100 nm in thickness. Following the recipe of the plan-view specimen preparation method using Omniprobe, the lamella was rotated to the horizontal orientation on the Omniprobe needle and then transferred to a heating E-chip by ISLO method for the heating study. Final thinning was performed with 5 kV Ga ions to remove the damaged layer on the lamella surface during 30 kV Ga ion milling.

(4) STEM imaging and spectroscopy analysis:

In-situ STEM heating was performed on the Protochips Aduro heating specimen holder, which enables heating a specimen from room temperature (RT) to the target temperature within one second so that the thermal drift is minimized even for high-resolution STEM imaging. The accuracy of the applied temperature on the Protochips heating grid is less than 5 °C. The base chamber pressure of the microscope is ~1.5×10^{-6} mbar. STEM Imaging was performed using a JEM-ARM200F (JEOL USA Inc.) equipped with a spherical aberration (Cs) corrector (CEOS GmbH, Heidelberg, Germany). The microscope was operated at 200 kV, and the probe convergence semi-angle was 23 mrad with a probe current of 18 pA. The corrector has been carefully tuned by the Zemlin-tableau method with Cs = 0.5 μm and the resolution is about 1 Å. The acquisition semi-angle for high angle annular dark field (HAADF) detector and annular bright field (ABF) detector was 90-370 mrad and 12-24 mrad, respectively. Energy Dispersive X-ray Spectroscopy (EDS) was performed with an Oxford X-MaxN100TLE with 100 mm^2 silicon drift detector. Prior study shows that the displacement threshold energy to create a Te vacancy in $MoTe_2$ is 5.9 eV, corresponding to the electron energy of 270 keV.[26] In this work, we use 200 kV for the imaging so electron beam induced irradiation effects are not responsible for the thermally activated Te desorption here.

3.3.2 Density Functional Theory (DFT) Calculations

The structure optimizations of the Mo_6Te_6 NWs were performed within the framework of DFT using Vienna ab initio package (VASP). Calculations based on the generalized gradient approximation (GGA) using the Perdew-Burke-Ernzerhof (PBE) function were carried out with the projector augmented wave (PAW) pseudopotential plane-wave method. The Monkhorst-Pack k-point sampling method in the Brillouin zone is Γ-centered with a $10\times10^{\times8}$ mesh in ionic optimization of 2H-$MoTe_2$. The sampling mesh for the ionic relaxation of Mo_6Te_6 NW is 4×4×10. The cutoff energy is 450 eV, and the criteria of convergence for energy and force are set to be 1×10^{-4} eV and 0.02 eV/Å, respectively. The Grimme-D3 Van der Waals correction is applied to include the interaction between Mo_6Te_6 NWs.

3.3.3 STM and XPS Characterization

A bulk $MoTe_2$ crystal was used for the surface STM and XPS characterization. The annealing and surface characterization was carried out in an Omicron Nanotechnology designed ultrahigh vacuum (UHV) system with a base pressure of ~10^{-10} mbar. The UHV system is equipped with a load-lock chamber, an annealing chamber, an XPS analysis chamber, and a room temperature STM (Omicron variable temperature STM.[27] **A freshly exfoliated** $MoTe_2$ **sample was quickly transferred into** the UHV system for initial surface analysis by XPS and STM. Then the sample was annealed in UHV at 200 °C, 300 °C, 400 °C, and 450 °C for 2 h, 1 h, 0.5 h and 0.25 h, respectively, and followed with XPS and STM characterization after the sample was cooled down to room temperature. A longer annealing time at a lower temperature is maintained to desorb possible (weakly bound) surface contaminants due to *ex-situ* sample preparation, whereas shorter annealing time is kept at a higher temperature to prevent significant tellurium desorption. During the annealing, the vacuum in the annealing chamber remains below 5×10^{-8} mbar. The error on the annealing temperature is less than 20 °C.

The STM images were obtained in constant current feedback mode at room temperature, and with polycrystalline W tips that were electrochemically etched and pulse cleaned for the STM/STS data. All bias voltages are applied to the sample with respect to the ground. The STM data were analyzed with WSxM software.

XPS spectra of Te 3*d*, Mo 3*d*, O 1*s*, C 1*s*, and Te 4*d* core levels and valence band regions were recorded with a monochromatic Al Kα X-ray source (hν = 1486.7 eV) with a pass energy of 15 eV and a take-off angle of 45° from the sample surface normal. The analytical spot size is ~640 μm^2. The XPS spectra were analyzed with AAnalyzer software,[28] and the stoichiometry of the $MoTe_2$ were determined using a relative sensitivity factor of 5.705 and 3.321 for Te $3d_{5/2}$ and Mo 3*d* peaks, respectively. To check the uniformity of the surface chemistry, stoichiometry and morphology, XPS and STM characterization is performed on multiple, independent surface regions on the initial surface or after annealing.

3.4 Results and Discussion

3.4.1 *In Situ* Heating Study of Few Layers $MoTe_2$

In this work, the 2H-$MoTe_2$ to Mo_6Te_6 NW transition process is monitored by scanning transmission electron microscopy (STEM) through three $MoTe_2$ orientations: plan-view [0001]

(Figure 3.2 and Figure 3.5B-D) and cross-sectional views [1-100] (Figure 3.3) and [11-20] (Figure 3.4 and Figure 3.5E-F), respectively. No obvious change can be found if the temperature is below 250 °C (Figure 3.2A-B). However, nanometer-sized bright spots appear once the temperature reaches 300 °C (Figure 3.2E-H). Finally, a streak morphology starts to propagate in $MoTe_2$ if the temperature is higher than 450 °C (Figure 3.2I-L and Figure 3.5B-D).

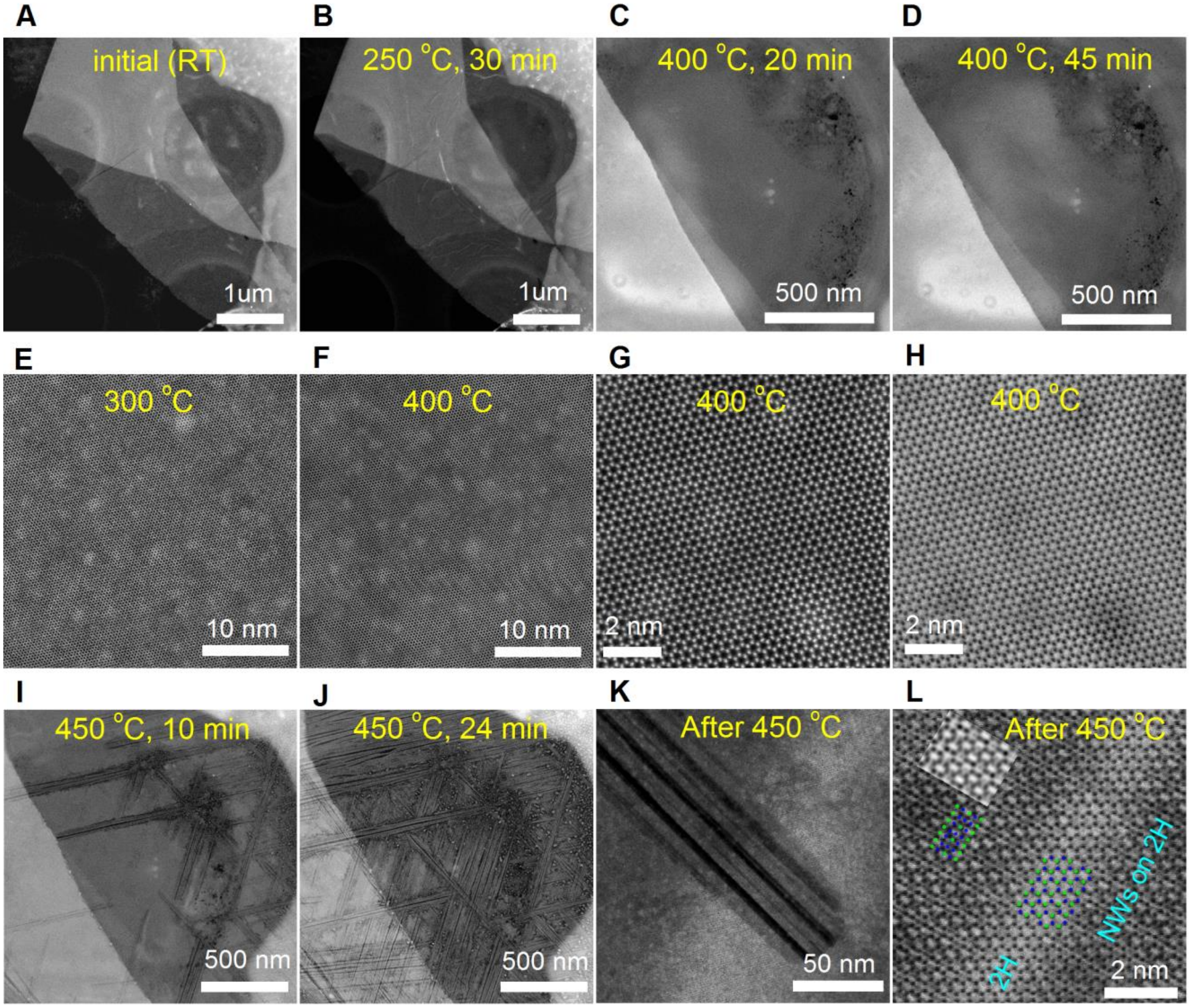

Figure 3.2. Morphology changes of plan-view 2H-$MoTe_2$ flake during the *in situ* heating process. (A-D) Low magnification HAADF images of the 2H-$MoTe_2$ flake when heated from room temperature (RT) to 400 °C. (E, F-H) STEM images of the 2H-$MoTe_2$ at 300 °C and 400 °C,

respectively, showing the generated nanometer-sized bright spots (in HAADF mode). High magnification images in (G) HAADF and (H) ABF mode in (F). (I, J) Dramatic morphology evolution of the 2H-$MoTe_2$ flake due to fast growth of Mo_6Te_6 NW bundles and Te desorption along the <11-20> directions. (K) HAADF image of the NW bundle interface with 2H-$MoTe_2$. (L) High magnification ABF image of the boundary region between the 2H-$MoTe_2$ and Mo_6Te_6 NWs. The inset exhibits a STEM simulation of the Mo_6Te_6 NW region with a NW separation of 8.9 Å and lattice constant c of 4.6 Å.

The NW formation rate/temperature is faster/lower with facilitated Te desorption. It is seen experimentally that NW formation is relatively facile on the plan-view specimen (Figure 3.2E) where Te loss is clearly detected at 300 °C in comparison to the cross-sectional [1-100] (Figure 3.3) and [11-20] specimens (Figure 3.4) where Te loss is detected upon annealing at 450 °C. As a result, Mo_6Te_6 NW-phase formation occurs near T = 450 °C for the plan-view [0001] specimen (Figure 3.2I-J and Figure 3.5B-D), and T = 500 °C for the cross-sectional view [1-100] and [11-20] specimens. Before the NW phase forms, the 2H-$MoTe_2$ structure is maintained, and the image contrast is only affected by some surface decomposition and Te desorption. The extent of the Te desorption increases with the annealing time or temperature.

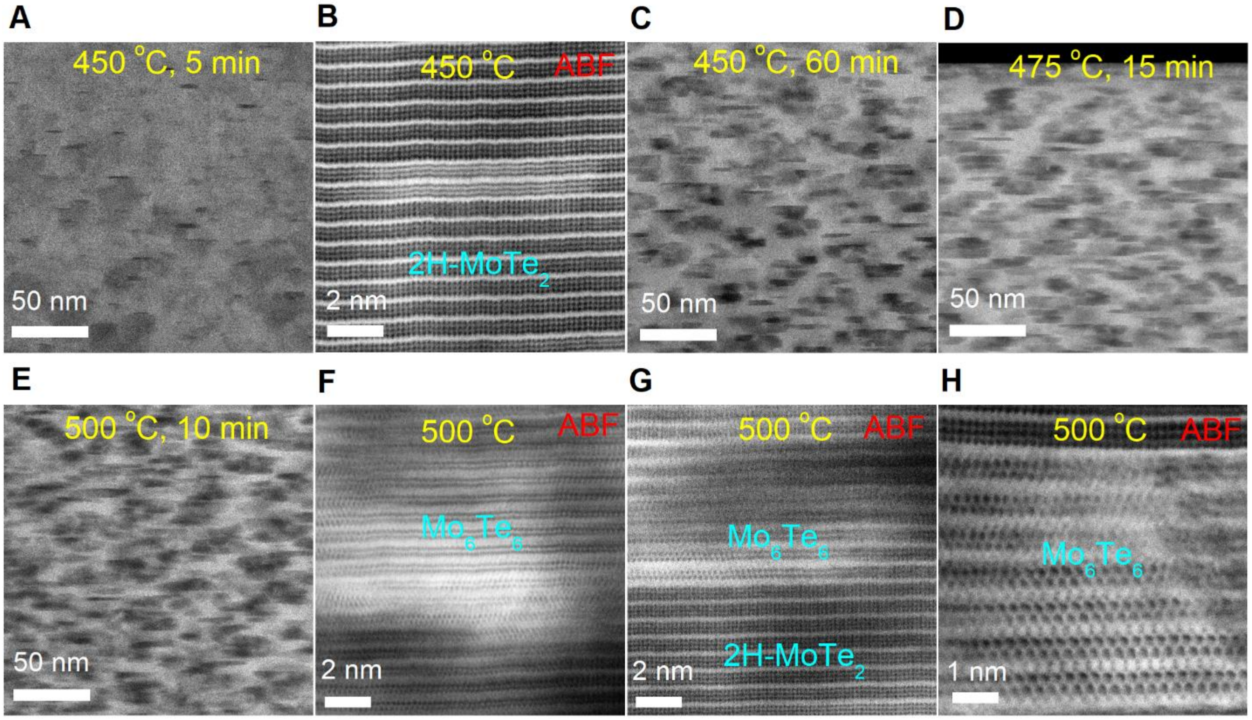

Figure 3.3. Morphology changes of cross-sectional view along 2H-$MoTe_2$ [1-100] orientation during the *in situ* heating process. (A) Streak morphology start to appear due to Te desorption in vacuum. (B) Zoom in of the streak morphology. (C-E) Low magnification image shows the increase of the density of the streak morphology in extent with annealing time and temperature. (F-H) Zoom in of Mo_6Te_6 NWs embedded in 2H-$MoTe_2$. The images are acquired at room temperature after 500 °C heating.

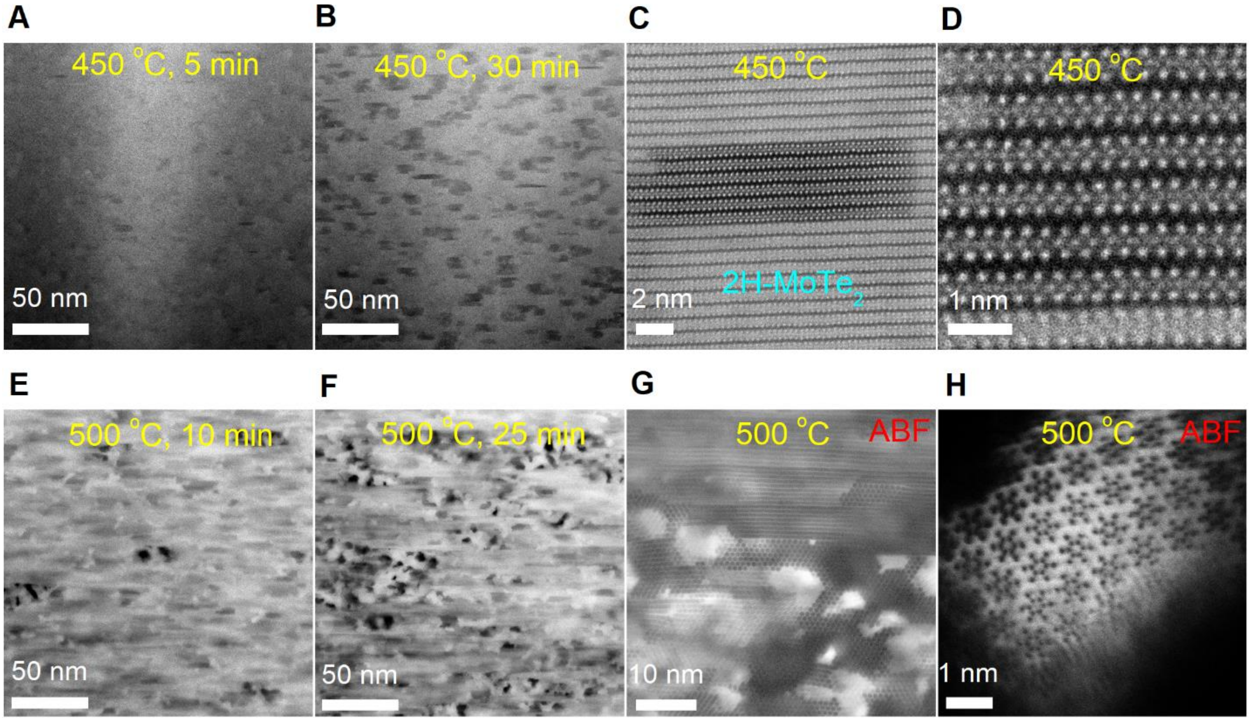

Figure 3.4. Morphology changes of cross-sectional view along 2H-$MoTe_2$ [11-20] orientation during the *in situ* heating process. (A-B) The density of the streak morphology increase with time during 450 °C heating. (C-D) Zoom in of the streak morphology. No Mo_6Te_6 NWs been formed in this stage. (E-F) Low magnification image shows the formation of Mo_6Te_6 NWs during 500 °C heating. Voids start to appear in the specimen. (G) Mo_6Te_6 NWs tend to be formed near the void region. (H) High resolution STEM image of Mo_6Te_6 NWs in a void region.

Figure 3.5B presents the overall morphology in plan-view of the 2H-$MoTe_2$ [0001] at 450 °C, showing the resulting “streak line” morphologies due to the Te desorption and formation of Mo_6Te_6 NW bundles along the three-fold 2H-$MoTe_2$ <11-20> crystallographic directions at 450 °C. NW bundles can be up to 1 micrometer in length. Energy dispersive X-ray spectroscopy (EDS, Figure 3.5C) demonstrates that the vacuum annealing process resulting in the Mo_6Te_6 NWs formation is associated with Te loss from the 2H-$MoTe_2$ structure so that the Te/Mo ratio at the NW region decreases to 1.07, which is consistent with the stoichiometry of Mo_6Te_6.

Transformation of 1D NWs of Mo_6Te_6 from 2H-$MoTe_2$ (Figure 3.5A) is neither predicted in the Mo-Te phase diagram nor reported in previous growth of $MoTe_2$ polymorphs (2H and 1T' phases).[29-33] This is likely because the 2H-to-1T' phase transition of $MoTe_2$ is favorable under thermodynamic equilibrium due to the small formation energy difference (0.03 eV) between its 2H and 1T' structure.[34] Indeed, the 2H-to-1T' phase transition can be triggered through thermal,[5, 35] strain,[6] charge,[36] or laser irradiation[7] approaches. The thermally driven 2H-to-1T' transition temperature for $MoTe_2$ under thermodynamic equilibrium is roughly in the range of 500-880 °C, and likely depends upon the concentration of Te.[11, 35] However, the similar electronegativity values for Mo and Te impact the Mo-Te bond strength/stability, making it easier for Mo-Te bond scission relative to other MX_2 transition-metal dichalcogenides. This bond scission, and thus desorption of volatile Te, may be further enhanced under vacuum annealing conditions and thus inhibit the 2H-to-1T' transition that is not observed during this experiment.

The role of Te loss/desorption in the formation of Mo_6Te_6 NWs is further accentuated upon comparing the formation rate of NWs on these STEM specimens at the same temperature. Real-time growth of Mo_6Te_6 NWs (T = 450 °C) are recorded in time-sequential STEM images along the plan-view (Figure 3.5D) and cross-sectional [11-20] directions (Figure 3.5E-F), respectively, showing a much faster formation rate of Mo_6Te_6 NWs along their *c* axial direction (which is also in alignment with the 2H-$MoTe_2$ <11-20> directions) than along their [100] direction. It is noted that the specimen described in Figure 3.5E-F has been used for the initial RT-to-500 °C annealing experiment to study the thermal stability of the [11-20] specimen (Figure 3.4) and then cooled down to RT for STEM imaging. Figure 3.5E-F are recorded at 450 °C upon reannealing the specimen. The lowered NW formation temperature is also attributed to an enhanced Te loss through pre-heating.

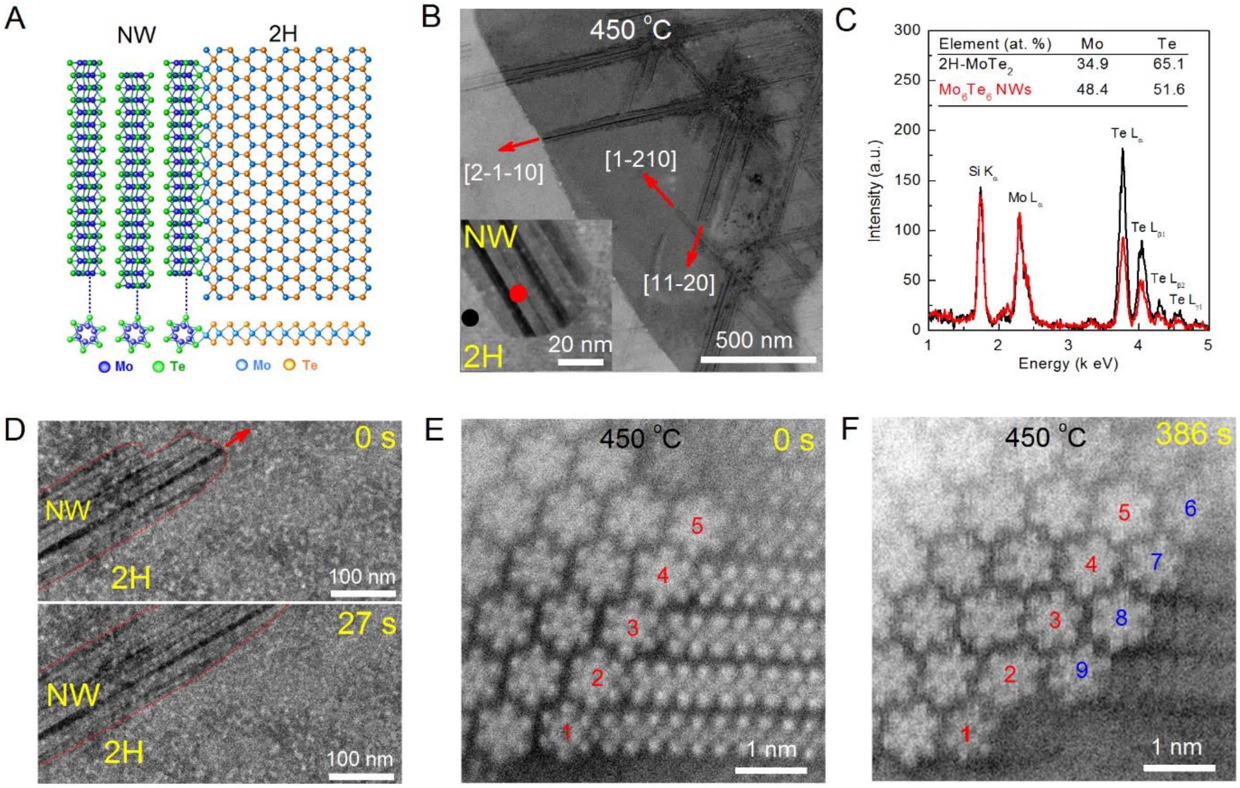

Figure 3.5. The transition and growth of Mo_6Te_6 NWs from 2H-$MoTe_2$. (A) Schematic of the transition from 2H-$MoTe_2$ to Mo_6Te_6 subnanometer-diameter NWs. (B) Large scale plan-view image of Mo_6Te_6 NW bundles grown on 2H-$MoTe_2$ (0001) surface at T = 450 °C along the <11-20> crystallographic directions (red arrows). The inset shows a zoomed-in image of the end of one NW bundles, which has a width of ~50 nm. (C) EDS analysis on top of Mo_6Te_6 NW bundles (red dot) and the nearby 2H-$MoTe_2$ region (black dot in the inset panel of B), respectively, showing the corresponding Te/Mo ratios of 1.07 (NWs) and 1.87 (2H phase). The Si signals in the EDS spectrum come from the underlying SiC supporting film of the heating E-chip. (D) Time sequence images of 2H-$MoTe_2$ (0001) show a fast growth of Mo_6Te_6 NWs along the 2H-$MoTe_2$ <11-20> directions at 450 °C. (E-F) Time sequence images viewed along the 2H-$MoTe_2$ [11-20] direction (or Mo_6Te_6 [001]) at 450 °C, showing new Mo_6Te_6 NWs formed from 2H-$MoTe_2$. All STEM images are recorded in high angle annular dark field (HAADF) mode.

A 1D chain of M-X NWs, with a basic formula of M_6X_6, consists of an infinitely staggered stack of two equilateral M_3Te_3 units (red triangles in Figure 3.6A). Each M_3X_3 unit has 3 X atoms at its vertexes and 3 M atoms between each pair of X atoms. EDS analysis in Figure 3.6B confirms the inner Mo core and outer Te decoration within one single Mo_6Te_6 NW. The binary Mo_6Te_6 NWs formed here follows a monoclinic assembly as schematically shown in Figure 3.6A and confirmed from a $c/2$ shift along the axial direction between two NW neighbors (Figure 3.6C). This monoclinic assembly is distinct from hexagonal *ternary* crystal compounds without the $c/2$ shift ($A_xMo_6X_6$, A = ternary elements such as alkali metals, indium, iodine, etc. filling the interstitial voids between NWs, x = 1-3), such as those described by, for example, Cheverel[18] and others[19-23] requiring intercalation of elements during crystal growth at high temperatures or long durations. The orientation and separation of stacked NWs can be affected by intercalated atoms.[37] The orientation can be defined by the rotation angle (α, shown in Figure 3.6A) with respect to the neighboring NWs, and can change to ~0° when inserted with interstitial Mo or Te atoms.[38] Here, the binary Mo_6Te_6 NWs without interstitial atoms show a configuration with a NW separation of 8.9±0.1 Å and each NW is slightly rotated for α ~11±1° (Figure 3.6D). This is consistent with the density functional theory (DFT) model stability study of the Mo_6Te_6 NWs after formation where the 11° rotated configuration, without interstitial atoms, is the energetically most stable.

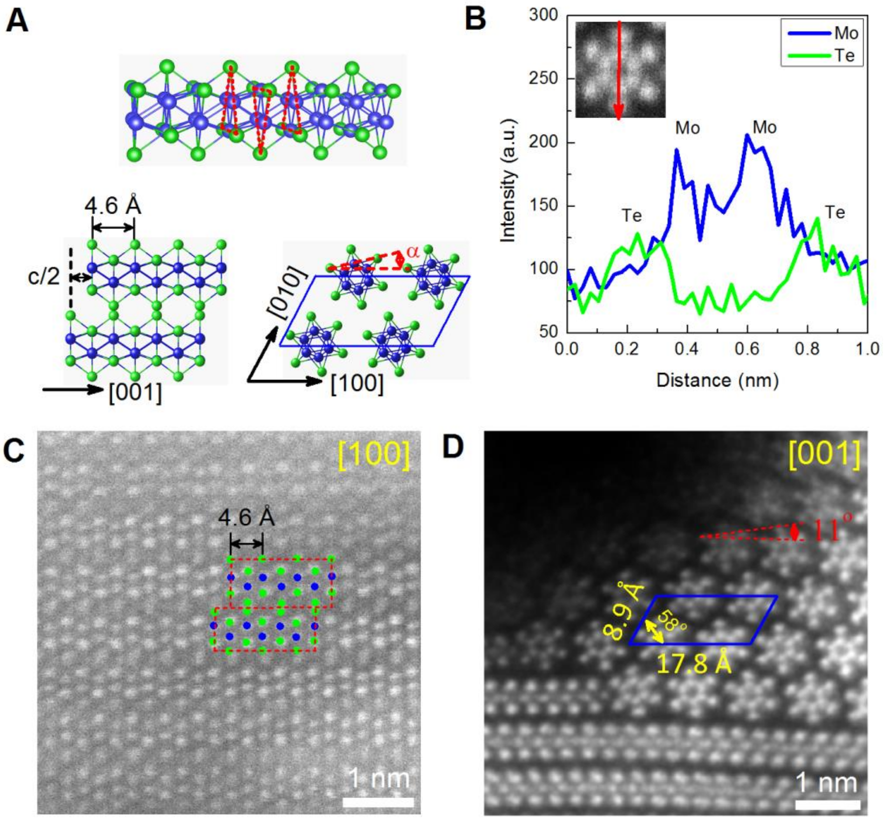

Figure 3.6. Monoclinic assembly of the Mo_6Te_6 NWs. (A) Atomic structure models of Mo_6Te_6 NWs viewed along different crystallographic directions. α is the relative rotation angle of the NW. (B) EDS line scan across one NW center, confirming the Mo and Te atomic positions in the NW structure. (C-D) High resolution cross-sectional STEM images of Mo_6Te_6 NWs along its (C) [100] and (D) [001] directions. In the STEM images, c is ~4.6 Å and α is ~11±1°. All STEM images are taken in HAADF mode.

In addition, the NW separation observed in our monoclinic assembly is also smaller than that of the hexagonal assembly from previous DFT calculations (NW separation of 9.45 Å, c = 4.58 Å).[39] As the layer thickness of the Mo_6Te_6 NWs (~7.6 Å) is larger than that of 2H-$MoTe_2$ (7 Å), dislocation core-like regions where two $MoTe_2$ layers join to become one Mo_6Te_6 NW can be observed during the phase transition process (Figure 3.7). It is obvious that the 2H-to-NW transition may not be limited within the same 2H layer. Regardless of the NW orientations and lattice mismatch, an atomically sharp $MoTe_2/Mo_6Te_6$ interface and vdW gap with the 2H-$MoTe_2$ substrate are preserved.

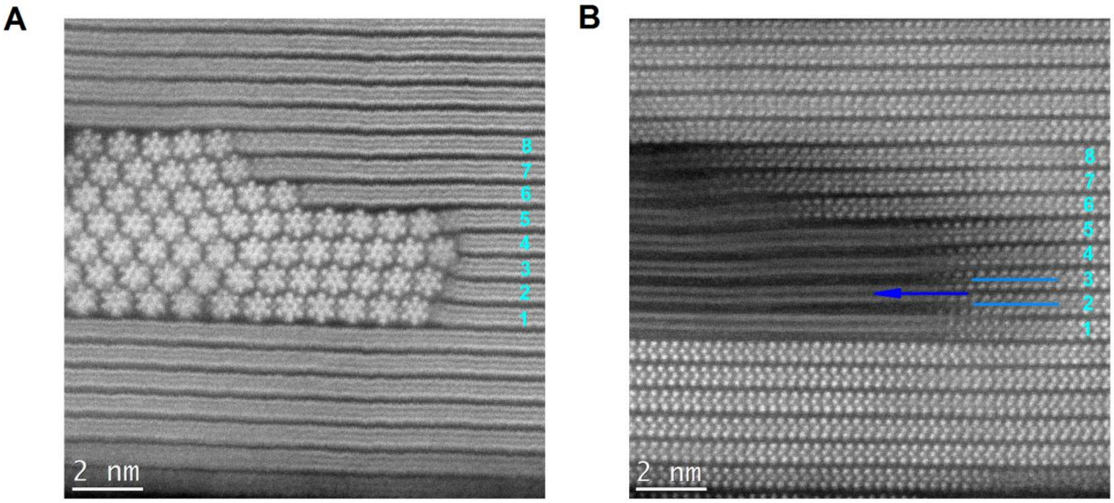

Figure 3.7. Dislocation core regions where two $MoTe_2$ layers join to become one Mo_6Te_6 NW. Images (A) and (B) are viewed along the axial direction of Mo_6Te_6 NWs and 2H-$MoTe_2$ [11-20], respectively. Clearly, 7 layers of NWs are aligned with 8 $MoTe_2$ layers, and some layers of Mo_6Te_6 (blue arrows) are formed by two adjacent $MoTe_2$ layers. Therefore, the 2H-$MoTe_2 \rightarrow Mo_6Te_6$ transition is not limited to the same $MoTe_2$ layer.

The electronic and chemical properties of Mo_6Te_6 NWs formed through the phase transition of the regions near the 2H-$MoTe_2$ surface are further investigated through *in situ* scanning tunneling microscopy (STM) and x-ray photoemission spectroscopy (XPS) with a bulk 2H-$MoTe_2$ crystal heated under ultra-high vacuum. STM (Figure 3.8A) confirms a full coverage of Mo_6Te_6 bundle networks on top of the 2H-$MoTe_2$ sample when annealed at 450 °C for 15 min, the same temperature for the growth of Mo_6Te_6 NWs on the STEM plan-view [0001] specimen. The lattice constants of NWs extracted from the STM measurements (NW separation of 9.0±0.2 Å and constant c along NW axis of 4.6±0.2 Å) are consistent with that of the 11° rotated NW configuration determined from the STEM. XPS (Figure 3.8B) also corroborates a significant presence of the new Mo_6Te_6 NW components (dark red curves, 572.2 eV for Te $3d_{5/2}$ and 227.5 eV for Mo $3d_{5/2}$) after the 450 °C annealing. An almost 0.4 eV downward shift of the substrate 2H-$MoTe_2$ components (blue curves) is induced with the coverage of Mo_6Te_6 NWs and indicates an upward band-bending from interfacial charge transfer (possibly hole injection) upon the Mo_6Te_6 NWs formation.

Scanning tunneling spectroscopy (Figure 3.8C) further provides evidence that Mo_6Te_6 NW bundles are metallic, which is also consistent with the observation of the alignment of valence band maximum with the Fermi level position. DFT band structures of a single Mo_6Te_6 nanowire and bulk Mo_6Te_6 NWs in a monoclinic assembly are shown in Figure 3.8D-E, confirming the intriguing semiconducting property of an isolated nanowire with a bandgap of ~0.3 eV and the metallic nature of Mo_6Te_6 NW bundles determined by a partially occupied conduction band.[40-41] However, we only detect Mo_6Te_6 NW bundles formed from the bulk $MoTe_2$ crystal in this work which is ternary element free, and consistent with the observed 11° orientation.

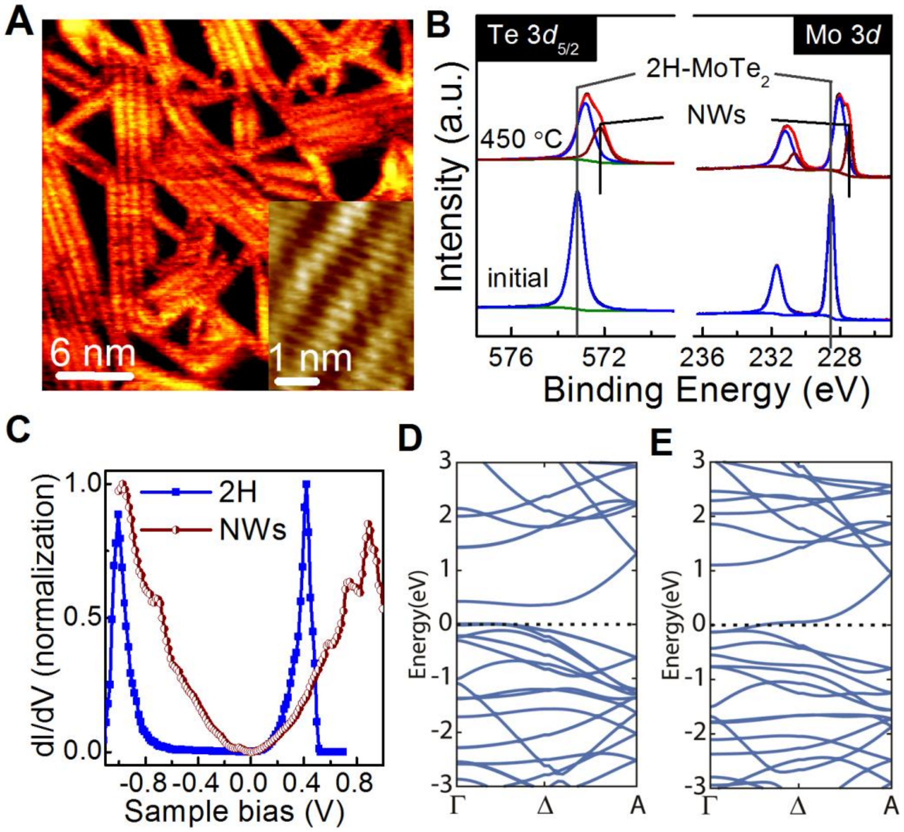

Figure 3.8. *In situ* XPS and STM observations of the Mo_6Te_6 NWs formed on top of 2H-$MoTe_2$. (A) STM image (sample bias V_b = -0.5 V and tunneling current I_t = 1.5 nA) of the formed Mo_6Te_6 NW networks on top of 2H-$MoTe_2$ upon the 450 °C annealing in ultra-high vacuum for 15 min. The inset shows an atomic image of the Mo_6Te_6 NWs. (B) XPS spectra of Te 3$d_{5/2}$ and Mo 3d doublet core-levels of the 2H-$MoTe_2$ crystal before and after the surface formation of Mo_6Te_6 NWs at 450 °C. The overall surface Te/Mo ratios determined from the curve fitting are 2.12±0.02 and 1.54±0.05 for the initial and 450 °C annealed surfaces, respectively. (C) Normalized differential conductive dI/dV spectra measured on the initial 2H-$MoTe_2$ surface (blue) and the formed Mo_6Te_6 NWs (dark red), respectively, showing the corresponding band gaps of ~1.02 eV and ~0 eV. DFT band diagrams of (D) single and (E) multiple Mo_6Te_6 NWs; Fermi level is set to zero as reference.

3.4.2 *In Situ* Heating Study of Monolayer and Bilayer $MoTe_2$

In section 3.4.1, we observed the formation of Mo_6Te_6 nanowires for few layers $MoTe_2$ under the vacuum annealing (450-500 °C). However, the dynamics of the 2H-NW phase transition cannot be observed at the atomic level because of the thickness of $MoTe_2$ flake. In this section, the *in situ* heating experiment is performed using a monolayer and bilayer $MoTe_2$ flake in the TEM column. Figure 3.9A shows the image of a monolayer $MoTe_2$ transferred on a Protochips thermal E-Chip, and its corresponding atomic-resolution HAADF image (see inset in Figure3.9A). In Figure 3.9B, nanometer-sized bright spots appear on the $MoTe_2$ flake after 300 °C annealing, which is consistent with the observation of few layers $MoTe_2$ in section 3.4.1. Since the energy required to move a Te atom into the vacuum is much lower than that for a Mo atom, Te vacancies are generated continuously when the heating is prolonged. Simultaneously, excess Mo atoms tend to migrate on the flake surface and react with the carbon residue to form the nanometer-sized MoC clusters. Therefore, pores can be initiated and expanded during the flake annealing. The dissociation of Te from the $MoTe_2$ flake and the formation of MoC_x clusters at relatively low temperature indicates that $MoTe_2$ has poor thermal stability.

After heating at 400 °C, large faceted hexagonal or triangular-shaped pores are observed along the <11-20> directions of $MoTe_2$ (Figure 3.9C). Interestingly, most of the edges of $MoTe_2$ flake are terminated with the Mo_6Te_6 NWs. The NW-terminated edge is similar to what reported in a recent publication of $Mo_xW_{1-x}Se_2$ under 500 °C annealing.[42] The temperature (400 °C) for NWs formation in monolayer $MoTe_2$ is lower than that in thick $MoTe_2$ flakes (450 °C), indicating that Te dissociation is easier for monolayer $MoTe_2$. Apart from Mo_6Te_6 NWs, MoC_x clusters are frequently observed in the pores or next to the edge of $MoTe_2$ flake.

Figure 3.9D shows a typical morphology of the flake after a long time annealing at 450 °C. The average length of NWs is less than 100 nm, which is remarkably smaller than the length of NWs formed in thick $MoTe_2$ flake. This can be easily explained by the nature of monolayer $MoTe_2$

flake that Te atoms in monolayer $MoTe_2$ are directly exposed to the vacuum. As a comparison, it is much more difficult for the Te atoms in a thick $MoTe_2$ flake to first migrate to the flake surface and then escape into the vacuum. Therefore, the 2H-NW phase transition can take place along Te escape channels, i.e., <11-20> $MoTe_2$ directions.

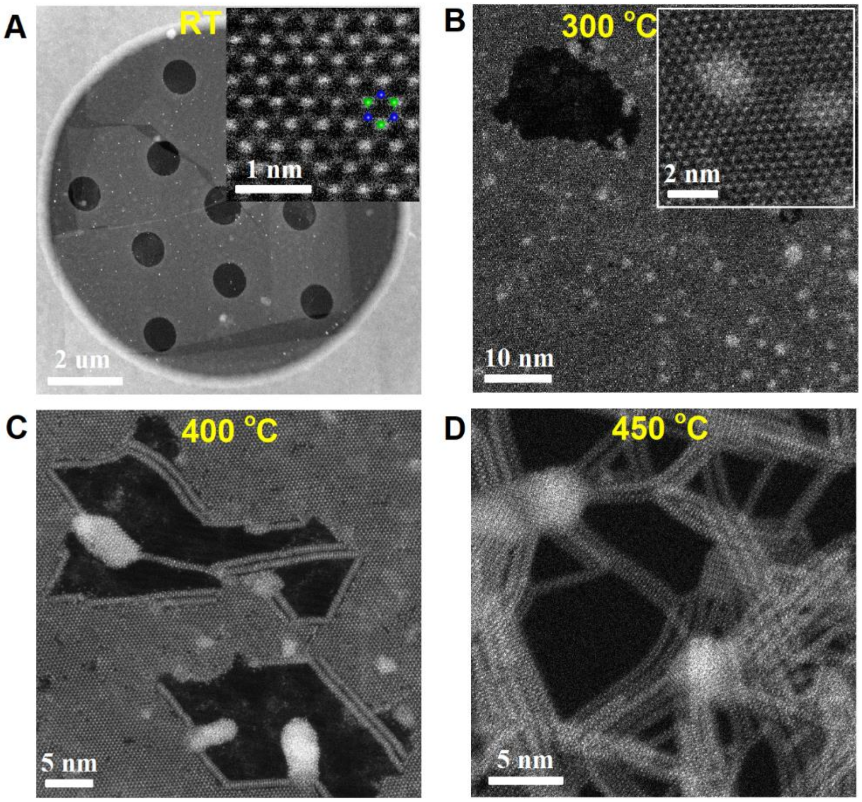

Figure 3.9. 2H-$MoTe_2$-to-Mo_6Te_6 NW phase transition in monolayer $MoTe_2$ (A) The morphology of a monolayer $MoTe_2$ and its corresponding atomic-resolution Z-contrast image. (B) Nanometer-sized bright spots observed at 300 °C. (C) Mo_6Te_6 NWs-terminated edges are observed after annealing at 400 °C. (D) Complete conversion of $MoTe_2$ to Mo_6Te_6 NWs after a long time annealing at 450 °C.

We also investigated the 2H-NW phase transition in a bilayer $MoTe_2$ flake (Figure 3.10). In addition to the NW-terminated edges, an abnormal intermediate phase is observed during the phase transition. Sequential STEM imaging is performed to analyze the NW formation. The initial morphology of the intermediate phase is highlighted by a dashed box in Figure 3.10A. After 494 s, the gliding of an NW is observed (Figure 3.10C), indicating the flexibility of NWs under the electron beam irradiation.[16, 43] However, the intermediate phase is quite stable even with the electron beam irradiation, and there is not much change in the structure. After 545 s, the intermediate phase starts to vibrate as a result of the continuous electron beam irradiation. Finally, the growth of a short NW to a long NW is observed during the folding of the intermediate phase. Figure 3.10B shows the zoom-in of the intermediate phase. Through a quantitative analysis of the Z-contrast STEM image, the number of atoms in an atomic column could be identified.[44] In particular, the thickness of the intermediate phase can be categorized into three types: low intensity, medium intensity, and high intensity, corresponding to one, two, and three atoms in an atomic column, respectively. The columns with low intensity can only be found at the edge of the intermediate phase. The columns with three atoms (high intensity) are generally separated by the columns with two atoms (medium intensity), and vice versa. After comparing with the structure of Mo_6Te_6 NW (as shown in Figure 3.10B), we found that the structure of three-atom columns is Te-Mo-Te, while the two-atom columns could be Te-Te, Mo-Mo, or Mo-Te, respectively. In addition, the two-atom columns (highlighted by purple circles) in Figure 3.10B are shared by two NW-like structures (highlighted by the red rectangles). As observed in Figure 3.10D, the vibration of the intermediate phase caused the atoms separation in Te-Te columns, resulting in the formation of NW from its edge.

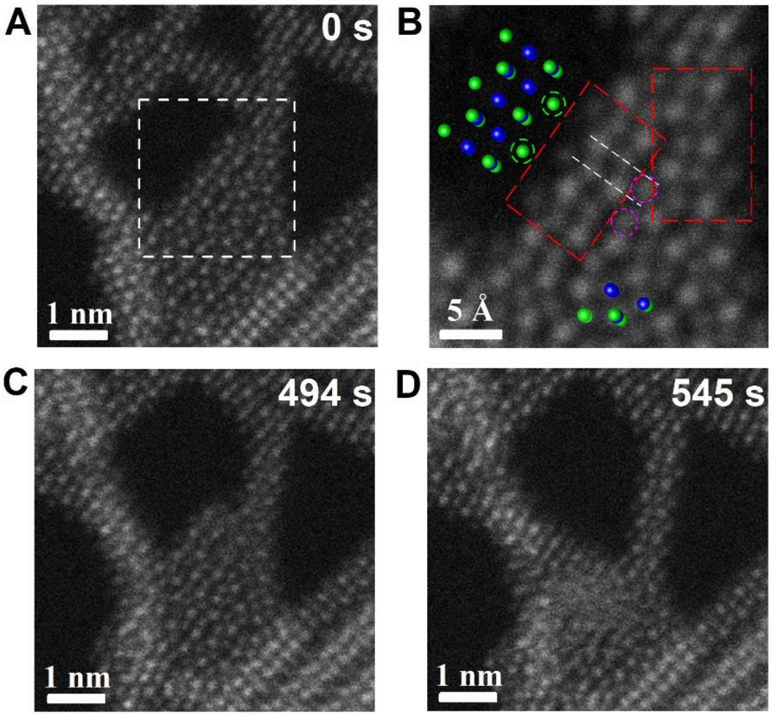

Figure 3.10. The intermediate phase founded in a bilayer $MoTe_2$ during the 2H-NW phase transition (A-B) Initial morphology of the intermediate phase. (C) The gliding of an NW. (D) NW formation at the edge of the intermediate phase.

3.4.3 Influence of Polymer Residue

In section 3.4.2, we observed the formation of nanometer-sized MoC_x clusters during vacuum annealing, indicating the influence of carbon residue during the phase transition. In this section, the influence of carbon residue is extensively analyzed.

Figure 3.11 shows two examples of the influence of carbon residue during TEM observation. Figure 3.11A shows a bilayer $MoTe_2$ flake with many carbon residues. A huge number of vacancies are created even with a fast scanning at low magnification. The ionization effect of the electron beam makes the carbon residue very reactive, even at room temperature. Figure 3.11B shows the tendrils morphology during vacuum annealing (without beam irradiation).

This morphology is occasionally observed from the $MoTe_2$ flake with heavy carbon residues. A more stable MoC is preferred during annealing when compared with the Mo_6Te_6 NWs.

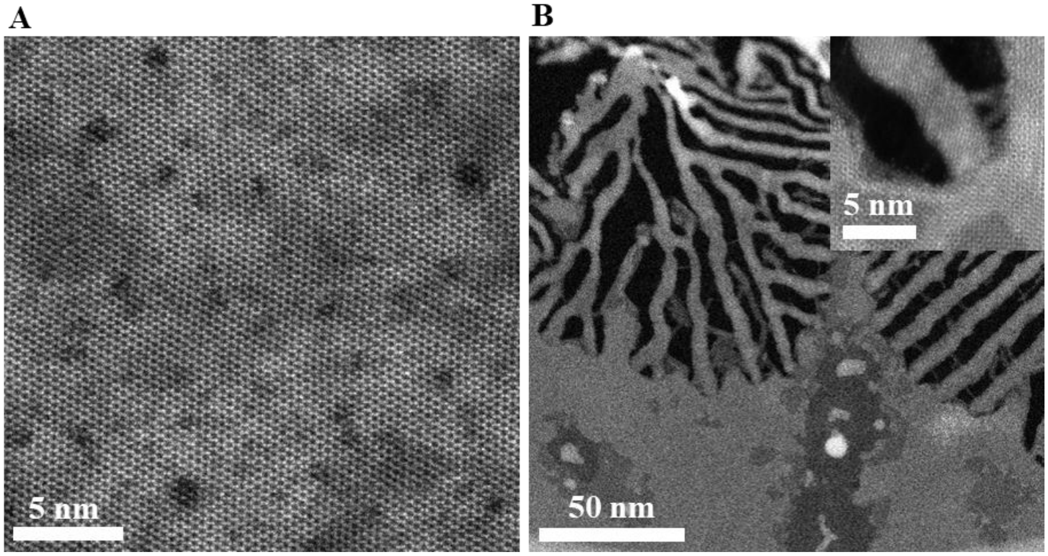

Figure 3.11. Influence of polymer residue (A) Vacancies are created in a bilayer $MoTe_2$ flake with many carbon residues, even a fast scan at low magnification is performed. (B) MoC_x of a tendrils morphology is observed for a $MoTe_2$ flake with heavy carbon residue.

The Mo_6Te_6 NW is relatively stable when the carbon residue is absent from the flake. However, it becomes unstable once there are carbon residues in the flake. Figure 3.12A-D shows the disappearance of a Mo_6Te_6 NW during a TEM observation at room temperature. There are medium carbon residues in this region, and NWs are formed at the edge of $MoTe_2$ flake prior to the observation (Figure 3.12A). After 67 s continuous scanning with the electron beam, the NW (highlighted with a dashed circle) starts to react with the carbon residue and break up from one end (Figure 3.12B). After 112 s, the NW shrinks from both ends and MoC_x clusters are formed at the edge of the flake (Figure 3.12C). Finally, the NW completely disappears after 160 s scanning, as shown in Figure 3.12D. This observation indicates the electron beam irradiation can significantly affect the stability $MoTe_2$ or Mo_6Te_6 NW when there are carbon residues. As a comparison, sequential images Figure 3.12E-H show the growth of a monolayer Mo_2C flake from the Mo_6Te_6 NWs during annealing. The Mo_6Te_6 NWs are formed prior to TEM observation. With the help of the electron beam irradiation, together with the annealing at various temperatures, a monolayer Mo_2C flake, originated from Mo_6Te_6 NWs (Figure 3.12E), gradually grows from a region with medium carbon residue (Figure 3.12F-H).

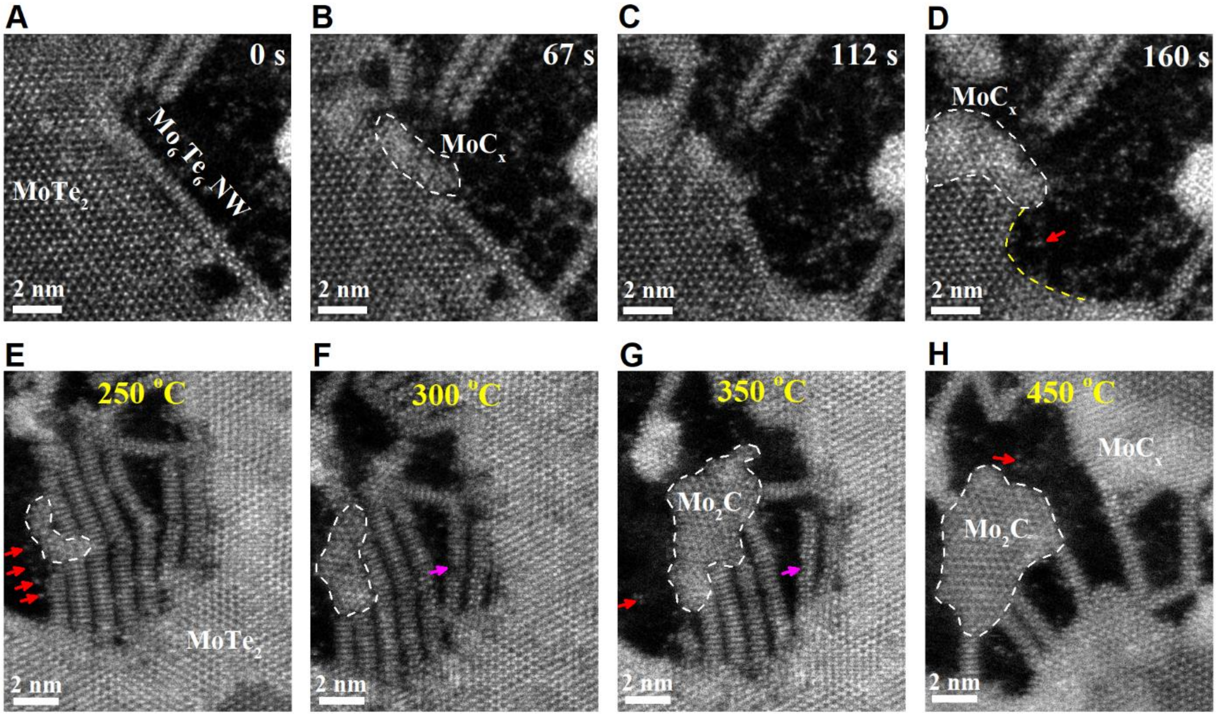

Figure 3.12. The stability of Mo_6Te_6 NWs under electron beam illumination. (A-D) Sequential images showing the disappearance of a Mo_6Te_6 NW. (E-H) Sequential images showing the formation of a monolayer Mo_2C flake from Mo_6Te_6 NWs. The MoC_x clusters and the etching of $MoTe_2$ are highlighted with the white and yellow dash lines, respectively. Single Mo or Te atoms (red arrows) can migrate along with the polymer residue. Polymer residue can react with Mo_6Te_6 NW under the electron beam illumination, highlighted by the purple arrow.

3.5 Conclusions

In conclusion, we present the first direct observation of the thermally driven phase transition from 2D 2H-$MoTe_2$ to 1D arrays of Mo_6Te_6 subnanometer-diameter NWs by vacuum annealing, *in situ* high-resolution STEM imaging and surface sensitive techniques (STM and XPS). The 2D-to-1D transition temperature range is 450-500 °C and primarily along the 2H-$MoTe_2$ <11-20> directions. We also observe the NW phase formation from the reconstruction at the edge of a monolayer flake at 400 °C and from the intermediate phase in bilayer $MoTe_2$, respectively. A novel NW-terminated edge is observed in monolayer $MoTe_2$ flake during vacuum annealing. The reduction of phase transition temperature is caused by the large specific surface of monolayer and bilayer $MoTe_2$, which facilitates the dissociation of Te from the $MoTe_2$ surface. We identify that the formation of Mo_6Te_6 NW from $MoTe_2$ is a complex process with multiple routes. A general hypothesis is that a Te deficient environment is required prior to the phase transition. The annealing or electron beam irradiation can provide the energy to overcome the energy barrier for the phase transition. In addition, we investigate the influence of carbon residue on the phase stability during the vacuum annealing, indicating that a clean $MoTe_2$ flake with a low concentration of carbon residue is required for the NW phase transition. Moreover, we study the electronic properties of the isolated Mo_6Te_6 NW and NW bundles using DFT calculation. DFT modeling shows that an isolated NW possesses a small gap (~0.3 eV) semiconducting property, while the NW bundles are predicted to be metallic. The metallic property of these bundles has been confirmed by STS and XPS measurements. The atomically sharp 2H-$MoTe_2$/Mo_6Te_6 NW interface highlights a potential strategy for contact engineering to improve the performance of $MoTe_2$ devices. Moreover, this low temperature, the thermally-driven transition, can be readily integrated into the fabrication of $MoTe_2$ based electronic devices as well.

3.6 References

1. Bhimanapati, G. R.; Lin, Z.; Meunier, V.; Jung, Y.; Cha, J.; Das, S.; Xiao, D.; Son, Y.; Strano, M. S.; Cooper, V. R., Recent advances in two-dimensional materials beyond graphene. *ACS Nano* **2015,** *9* (12), 11509-11539.

2. Chhowalla, M.; Shin, H. S.; Eda, G.; Li, L.-J.; Loh, K. P.; Zhang, H., The chemistry of two-dimensional layered transition metal dichalcogenide nanosheets. *Nature chemistry* **2013,** *5* (4), 263.

3. Radisavljevic, B.; Radenovic, A.; Brivio, J.; Giacometti, V.; Kis, A., Single-layer MoS 2 transistors. *Nature nanotechnology* **2011,** *6* (3), 147.

4. Bockrath, M.; Cobden, D. H.; McEuen, P. L.; Chopra, N. G.; Zettl, A.; Thess, A.; Smalley, R. E., Single-electron transport in ropes of carbon nanotubes. *Science* **1997,** *275* (5308), 1922-1925.

5. Kiriya, D.; Tosun, M.; Zhao, P.; Kang, J. S.; Javey, A., Air-stable surface charge transfer doping of MoS2 by benzyl viologen. *Journal of the American Chemical Society* **2014,** *136* (22), 7853-7856.

6. Kappera, R.; Voiry, D.; Yalcin, S. E.; Branch, B.; Gupta, G.; Mohite, A. D.; Chhowalla, M., Phase-engineered low-resistance contacts for ultrathin MoS 2 transistors. *Nature materials* **2014,** *13* (12), 1128-1134.

7. Cho, S.; Kim, S.; Kim, J. H.; Zhao, J.; Seok, J.; Keum, D. H.; Baik, J.; Choe, D.-H.; Chang, K. J.; Suenaga, K., Phase patterning for ohmic homojunction contact in MoTe2. *Science* **2015,** *349* (6248), 625-628.

8. Dawson, W.; Bullett, D., Electronic structure and crystallography of MoTe2 and WTe2. *Journal of Physics C: Solid State Physics* **1987,** *20* (36), 6159.

9. Hughes, H.; Friend, R., Electrical resistivity anomaly in β-MoTe2 (metallic behaviour). *Journal of Physics C: Solid State Physics* **1978,** *11* (3), L103.

10. Song, S.; Keum, D. H.; Cho, S.; Perello, D.; Kim, Y.; Lee, Y. H., Room Temperature Semiconductor–Metal Transition of MoTe2 Thin Films Engineered by Strain. *Nano Letters* **2016,** *16* (1), 188-193.

11. Keum, D. H.; Cho, S.; Kim, J. H.; Choe, D.-H.; Sung, H.-J.; Kan, M.; Kang, H.; Hwang, J.-Y.; Kim, S. W.; Yang, H., Bandgap opening in few-layered monoclinic MoTe 2. *Nature Physics* **2015,** *11* (6), 482-486.

12. Brusetti, R.; Monceau, P.; Potel, M.; Gougeon, P.; Sergent, M., The exotic superconductor Tl2Mo6Se6 investigated by low field magnetization measurements. *Solid state communications* **1988,** *66* (2), 181-187.

13. Armici, J.; Decroux, M.; Fischer, Ø.; Potel, M.; Chevrel, R.; Sergent, M., A new pseudo-one-dimensional superconductor: Tℓ2Mo6Se6. *Solid State Communications* **1980,** *33* (6), 607-611.

14. Liu, X.; Xu, T.; Wu, X.; Zhang, Z.; Yu, J.; Qiu, H.; Hong, J.-H.; Jin, C.-H.; Li, J.-X.; Wang, X.-R., Top–down fabrication of sub-nanometre semiconducting nanoribbons derived from molybdenum disulfide sheets. *Nature Communications* **2013,** *4* (1), 1-6.

15. Lin, J.; Cretu, O.; Zhou, W.; Suenaga, K.; Prasai, D.; Bolotin, K. I.; Cuong, N. T.; Otani, M.; Okada, S.; Lupini, A. R., Flexible metallic nanowires with self-adaptive contacts to semiconducting transition-metal dichalcogenide monolayers. *Nature nanotechnology* **2014,** *9* (6), 436.

16. Lin, J.; Zhang, Y.; Zhou, W.; Pantelides, S. T., Structural Flexibility and Alloying in Ultrathin Transition-Metal Chalcogenide Nanowires. *ACS Nano* **2016,** *10* (2), 2782-2790.

17. Lehtinen, O.; Komsa, H.-P.; Pulkin, A.; Whitwick, M. B.; Chen, M.-W.; Lehnert, T.; Mohn, M. J.; Yazyev, O. V.; Kis, A.; Kaiser, U., Atomic scale microstructure and properties of Se-deficient two-dimensional MoSe2. *ACS Nano* **2015,** *9* (3), 3274-3283.

18. Chevrel, R.; Sergent, M.; Seeber, B.; Fischer, Ø.; Grüttner, A.; Yvon, K., New ternary Mo (II)-compounds InxMo15Se19 containing Mo6Se8 and Mo9Se11 units. *Materials Research Bulletin* **1979,** *14* (4), 567-577.

19. Potel, M.; Chevrel, R.; Sergent, M.; Armici, J.; Decroux, M.; Fischer, Ø., New pseudo-one-dimensional metals: M2Mo6Se6 (M= Na, In, K, TI), M2Mo6S6 (M= K, Rb, Cs), M2Mo6Te6 (M= In, TI). *Journal of Solid State Chemistry* **1980,** *35* (2), 286-290.

20. Tarascon, J.; DiSalvo, F.; Waszczak, J., Physical properties of several M2Mo6X6 compounds (M= group IA metal; X= Se, Te). *Solid state communications* **1984,** *52* (3), 227-231.

21. Sheridan, J. G.; Heidelberg, A.; Brougham, D. F.; Nellist, P. D.; Langford, R. M.; Boland, J. J., Self-Assembly of LiMo3Se3 Nanowire Networks from Nanoscale Building-Blocks in Solution. *Langmuir* **2012,** *28* (43), 15344-15349.

22. Çakır, D.; Durgun, E.; Gülseren, O.; Ciraci, S., First principles study of electronic and mechanical properties of molybdenum selenide type nanowires. *Physical Review B* **2006,** *74* (23), 235433.

23. Hönle, W.; Von Schnering, H.; Lipka, A.; Yvon, K., New compounds with infinite chains of face-condensed octahedral Mo6 clusters: InMo3Se3, InMo3Te3, TlMo3Se3 and TlMo3Te3. *Journal of the Less Common Metals* **1980,** *71* (1), 135-145.

24. Castellanos-Gomez, A.; Buscema, M.; Molenaar, R.; Singh, V.; Janssen, L.; van der Zant, H. S. J.; Steele, G. A., Deterministic transfer of two-dimensional materials by all-dry viscoelastic stamping. *2D Materials* **2014,** *1* (1), 011002.

25. Mayer, J.; Giannuzzi, L. A.; Kamino, T.; Michael, J., TEM sample preparation and FIB-induced damage. *MRS bulletin* **2007,** *32* (5), 400-407.

26. Komsa, H.-P.; Kotakoski, J.; Kurasch, S.; Lehtinen, O.; Kaiser, U.; Krasheninnikov, A. V., Two-Dimensional Transition Metal Dichalcogenides under Electron Irradiation: Defect Production and Doping. *Physical Review Letters* **2012,** *109* (3), 035503.

27. Wallace, R. M., In-situ studies on 2D materials. *Ecs Transactions* **2014,** *64* (9), 109.

28. Herrera-Gomez, A.; Hegedus, A.; Meissner, P., Chemical depth profile of ultrathin nitrided SiO 2 films. *Applied physics letters* **2002,** *81* (6), 1014-1016.

29. Diaz, H. C.; Chaghi, R.; Ma, Y.; Batzill, M., Molecular beam epitaxy of the van der Waals heterostructure MoTe2 on MoS2: phase, thermal, and chemical stability. *2D Materials* **2015,** *2* (4), 044010.

30. Roy, A.; Movva, H. C.; Satpati, B.; Kim, K.; Dey, R.; Rai, A.; Pramanik, T.; Guchhait, S.; Tutuc, E.; Banerjee, S. K., Structural and electrical properties of MoTe2 and MoSe2 grown by molecular beam epitaxy. *ACS applied materials & interfaces* **2016,** *8* (11), 7396-7402.

31. Park, J. C.; Yun, S. J.; Kim, H.; Park, J.-H.; Chae, S. H.; An, S.-J.; Kim, J.-G.; Kim, S. M.; Kim, K. K.; Lee, Y. H., Phase-engineered synthesis of centimeter-scale 1T′-and 2H-molybdenum ditelluride thin films. *ACS Nano* **2015,** *9* (6), 6548-6554.

32. Naylor, C. H.; Parkin, W. M.; Ping, J.; Gao, Z.; Zhou, Y. R.; Kim, Y.; Streller, F.; Carpick, R. W.; Rappe, A. M.; Drndic, M., Monolayer single-crystal 1T′-MoTe2 grown by chemical vapor deposition exhibits weak antilocalization effect. *Nano letters* **2016,** *16* (7), 4297-4304.

33. Zhou, L.; Xu, K.; Zubair, A.; Liao, A. D.; Fang, W.; Ouyang, F.; Lee, Y.-H.; Ueno, K.; Saito, R.; Palacios, T. s., Large-area synthesis of high-quality uniform few-layer MoTe2. *Journal of the American Chemical Society* **2015,** *137* (37), 11892-11895.

34. K C, S.; Zhang, C.; Hong, S.; Wallace, R. M.; Cho, K., Phase stability of transition metal dichalcogenide by competing ligand field stabilization and charge density wave. *2D Materials* **2015,** *2* (3), 035019.

35. Vellinga, M.; De Jonge, R.; Haas, C., Semiconductor to metal transition in MoTe2. *Journal of Solid State Chemistry* **1970,** *2* (2), 299-302.

36. Zhang, C.; KC, S.; Nie, Y.; Liang, C.; Vandenberghe, W. G.; Longo, R. C.; Zheng, Y.; Kong, F.; Hong, S.; Wallace, R. M., Charge Mediated Reversible Metal–Insulator Transition in Monolayer MoTe2 and W x Mo1–x Te2 Alloy. *ACS Nano* **2016,** *10* (8), 7370-7375.

37. Tarascon, J.-M.; Hull, G.; DiSalvo, F., A facile synthesis of pseudo one-monodimensional ternary molybdenum chalcogenides M2Mo6X6 (X= Se, Te; M= Li, Na.. Cs). *Materials research bulletin* **1984,** *19* (7), 915-924.

38. Zhu, H.; Wang, Q.; Zhang, C.; Addou, R.; Cho, K.; Wallace, R. M.; Kim, M. J., New Mo6Te6 Sub-Nanometer-Diameter Nanowire Phase from 2H-MoTe2. *Advanced Materials* **2017,** *29* (18), 1606264.

39. Yamada, T.; Hasegawa, T.; Hiraoka, M.; Matsui, H.; Tokura, Y.; Saito, G., Control of film morphology and its effects on subthreshold characteristics in dibenzotetrathiafulvalene organic thin-film transistors. *Applied Physics Letters* **2008,** *92* (23), 210.

40. Gougeon, P.; Potel, M.; Padiou, J.; Sergent, M., Silver Molybdenum Telluride (AgMo6Te6): A New One-Dimensional Structure Type Having Linear Chains| Mo6/2|∞ 1. *J. Solid State Chem* **1987,** *68*, 137-142.

41. Hor, P.; Fan, W.; Chou, L.; Meng, R.; Chu, C.; Tarascon, J.; Wu, M., Study of the metal-semiconductor transition in Rb2Mo6Se6, Rb2Mo6Te6 and Cs2Mo6Te6 under pressures. *Solid state communications* **1985,** *55* (3), 231-235.

42. Sang, X.; Li, X.; Zhao, W.; Dong, J.; Rouleau, C. M.; Geohegan, D. B.; Ding, F.; Xiao, K.; Unocic, R. R., In situ edge engineering in two-dimensional transition metal dichalcogenides. *Nat Commun* **2018,** *9* (1), 2051.

43. Lin, J.; Cretu, O.; Zhou, W.; Suenaga, K.; Prasai, D.; Bolotin, K. I.; Cuong, N. T.; Otani, M.; Okada, S.; Lupini, A. R.; Idrobo, J.-C.; Caudel, D.; Burger, A.; Ghimire, N. J.; Yan, J.; Mandrus, D. G.; Pennycook, S. J.; Pantelides, S. T., Flexible metallic nanowires with self-adaptive contacts to semiconducting transition-metal dichalcogenide monolayers. *Nat Nano* **2014,** *9* (6), 436-442.

44. Pennycook, S. J.; Nellist, P. D., *Scanning transmission electron microscopy: imaging and analysis*. Springer Science & Business Media: **2011**.

CHAPTER 4

IN SITU HEATING STUDY OF INVERSION DOMAIN BOUNDARIES IN MOTE$_2$

4.1 Preface

This chapter includes the material adapted with permission from a publication entitled **“Defects and Surface Structural Stability of MoTe$_2$ under Vacuum Annealing”** [ACS NANO, 2017, 11, pp 11005-11014]. Copyright, 2017, American Chemical Society. The authors are Hui Zhu, Qingxiao Wang, Lanxia Cheng, Rafik Addou, Jiyoung Kim, Mon J. Kim*, and Robert M. Wallace*. In this work, my contribution was in planning and executing the *in situ* TEM experiments, performing TEM data interpretation, and writing the manuscript. Hui Zhu is the coauthor of this publication under the supervision of Prof. R. Wallace and contributes equally to this work, including the design of surface analysis related experiments (*in situ* STM characterization, XPS, Raman), the corresponding data interpretation, and writing the manuscript. Dr. L. Cheng and Dr. R. Addou were acknowledged for their helpful discussion during the research.

4.2 Introduction

Among group-VIB transition-metal dichalcogenides (TMDs), semiconducting molybdenum ditelluride (2H-MoTe$_2$) with a bandgap very similar to Si (~1.1 eV for monolayer and 1.0 eV for the bulk state), is a promising electronic and photovoltaic device candidate.[1] Additionally, MoTe$_2$ possesses facile phase transition behavior. For example, the phase transition between its semiconducting 2H structure and its semimetallic, distorted octahedral 1T’ structure due to their small formation energy difference (~0.03 eV) is well-known.[2] Versatile methods of stimulating this transition, such as temperature, strain, and charge injection, have been theoretically or experimentally suggested.[2-6] Techniques for synthesizing the 2H[7-9] and the 1T' phases[8, 10-11] of $MoTe_2$ have also been developed and seems relatively more controllable than the other TMDs. Distinct phases can be formed by selecting the starting precursors[11] or adjusting the synthesis temperatures.[1, 4] Mainly, the thermal equilibrium for the 2H-to-1T' transition temperature of $MoTe_2$ has been reported in a range of 500-880 °C, and is likely related to the Te concentration.[1, 4] Usually, a relatively lower Te concentration is concomitant with a lower phase transition temperature.[1, 4]

The thermal stability of $MoTe_2$ needs careful evaluation for practical nanoelectronic device applications compared to other TMDs. Brainard *et al*. have reported two distinct weight loss temperatures for $MoTe_2$; 427 °C arising from the evaporation of excess Te and 700 °C from the dissociation of $MoTe_2$.[12] This dissociation temperature is much lower than that for disulfides (870-1040 °C) and diselenides (930-980 °C),[12] and is related to the weaker Mo-Te bond strength reflected in the small electronegativity difference between Mo and Te.[13-14] Recently, using scanning transmission electron microscopy (STEM) and scanning tunneling microscopy (STM) techniques, we have discovered a weakened Mo-Te bond strength/stability under vacuum annealing conditions (~400-500 °C), leading to a distinct 2H-to-one dimensional Mo_6Te_6 nanowire (NW) transition along the <11-20> 2H-$MoTe_2$ crystallographic directions as well as a fast Te desorption along these directions.[15]

In this work, we used STM and STEM to investigate the surface structural evolution of $MoTe_2$ crystals upon an ultra-high vacuum annealing (200 °C to 400 °C), revealing poor thermal stability of $MoTe_2$ due to the surface dissociation and desorption. In particular, the role of one inherent, nonstoichiometric defect arising from an elemental Te adatom has also been investigated thoroughly. The surface dissociation is found to take place at 200 °C, forming Te vacancies, pinholes, and randomly shaped clusters. At 400 °C, layer-type etched pits and intense inversion domain boundaries (IDBs) are formed, and the latter of which is mainly organized into a "wagon wheel" (WW) type morphology covering the sample surface. The atomic structure model and electronic properties of the IDBs are identified by STEM and scanning tunneling spectroscopy (STS), respectively. Additionally, Mo_6Te_6 NWs are occasionally found at pit edges due to the enhanced Te desorption. Finally, in regard to the degradation of $MoTe_2$ towards oxidation and reduced thermal stability by Te desorption, methods to prevent the Te loss by encapsulation methods are explored.

4.3 Experimental Section

The $MoTe_2$ crystals used in this work are chemical vapor synthesized by HQ Graphene using high purity molybdenum (99.9975%, Alfa Aesar) and tellurium (99.999%, Alfa Aesar) powders with Te vapor as a transport agent. 10 at. % more Te above the initial Te: Mo = 2:1 were added in the crystal growth process to avoid a Te deficiency and thus a more reactive surface to air exposure. Fresh sample surfaces are simply cleaved in air with Scotch® tape and then immediately loaded into an ultrahigh vacuum (UHV) system[16] (base pressure ~10^{-10} mbar) for the subsequent surface characterization and heating studies.

The UHV system (Omicron Nanotechnology designed) consists of an annealing chamber and one analysis chambers for XPS and room temperature STM (Omicron variable temperature

STM) analysis.[16] Samples are *in situ* transferred to the prep chamber for heating treatments and transferred back to the analysis chamber for XPS/STM analysis after cooling down to room temperature. The sample manipulator in the annealing chamber allows a programmable controlled ramp-up rate of the substrate temperature. The ramp-up rate of the substrate temperature in this experiment is ~5 °C/minute. The STM images are obtained with electrochemically etched W tips in constant current mode. The STM/STS data are analyzed with WSxM software. XPS spectra are obtained with a monochromatic Al Kα (hν = 1486.7 eV) X-ray source, which has pass energy of 15 eV and a take-off angle of 45° and then analyzed with AAnalyzer software[17].

The crystallinity and defects in monolayer or few-layer $MoTe_2$ are investigated with STEM measurements. A $MoTe_2$ thin flake is transferred onto a Protochips *in situ* heating grid by poly(bisphenol A carbonate) assisted wet transfer method.[18] In order to avoid electron beam induced damage, STEM imaging is performed on an aberration-corrected JEM-ARM200F (JEOL USA Inc.) operating at 80 kV. The convergence semi-angle of the electron beam is 25 mrad while the collection semi-angle for the annular dark field (ADF) detector is 70-370 mrad. In order to improve the signal-to-noise ratio of the atomically resolved STEM images on monolayer $MoTe_2$, the deconvolution method has been performed using the DeConvHAADF software (HREM Research Inc.). HAADF-STEM image simulation has been performed using QSTEM software[19] with the same parameters as the experimental settings. To create defects in the $MoTe_2$ thin film, spike annealing is applied at 450 °C for 60 s and immediately cooled down to room temperature. The *in situ* observation of the migration of IDBs is performed at 250 °C. A cross-section STEM specimen of the STM heated bulk $MoTe_2$ crystal is prepared using a focused ion beam system (FEI Nova 200 Dual Beam). The inductively coupled plasma mass spectrometry technique (ICPMS)[20] with a detection limit of 0.1 part per billion was used to search for impurities on initial $MoTe_2$ crystals.

To test the passivation of $MoTe_2$ flakes, the conventional PMMA assisted graphene transfer method is employed to transfer monolayer graphene from a Cu substrate to $MoTe_2$ flakes deposited onto a 90 nm SiO_2 layer on a Si substrate.[21] The thermal stability of graphene/$MoTe_2$ flakes is evaluated using Raman microscopy (InVia Confocal Renishaw spectroscopy), with the temperature-controlled by an N_2 purged LINKAM THMS600 heat cell.[22] Raman measurements of $MoTe_2$ flakes are performed using a 532 nm excitation laser and a 0.22 mW laser power to minimize laser-induced local thermal heating damage.

4.4 Results and Discussion

4.4.1 Surface Dissociation and Development Te vacancy

The surface chemistry of the initially exfoliated crystals is investigated with XPS, as shown in Figure 4.1a. Sharp peak spectra of Te 3d5/2 (573.2 eV) and the Mo 3d doublet (228.5 eV for Mo 3d5/2 and 231.65 eV for Mo 3d3/2) with minimized Te-O (~576.1 eV) and Mo-O (~232.2 eV) oxides are typically detected on freshly exfoliated MoTe2 surfaces. Depending on samples and scanning locations, the Te/Mo atomic ratios obtained from the XPS analysis of the Te 3d5/2 and Mo 3d core level regions vary within the range of 2.1-2.4 and thus suggesting either a tellurium-rich (Te interstitials or intercalates) or a molybdenum-deficient (Mo vacancies or substitutions) chemical environment.[23] It is noted that the defects mentioned above are not introduced during the ex-situ preparation process that often associates with hydrocarbon adsorption or slight surface oxidation (i.e., Te-O and Mo-O bonds). The defect is suggested to be atomic Te dopants that have been consistently observed on MoTe2 crystals from other sources with a Te/Mo ratio of 2.4-2.6.[24]

Scanning Tunneling microscopy (STM) with atomic sensitivity are employed to examine possible defect states within the Te-rich $MoTe_2$: interstitial/intercalated Te atoms and Mo vacancies. Figure 4.1c,d show typical STM images of a freshly exfoliated $MoTe_2$ (0001) surface measured at negative sample biases (empty-state). The surface is decorated with a high concentration of randomly distributed, nanometer-sized bright "protrusions" that are rarely reported in previous STM studies on $MoTe_2$.[25-28] The "protrusions" have an areal density of 23±3%, and a spatial extension of 1-2 nm. Similar "protrusion" decorated surfaces are also observed on $MoTe_2$ samples from different sources with higher defect concentrations and Te/Mo ratios. Sample bias dependent STM analysis of the protrusions reveals that the apparent protrusion height is strongly sample bias dependent. In general, the average height is around 3±0.5 Å at negative sample biases, higher than the average value of 1.0±0.3 Å obtained at positive sample biases. The variation of protrusion heights or their lateral extensions under the same imaging condition (see Figure 4.1d) is related to the inhomogeneous defect distribution in the subsurface layers. In Figure 4.1d, three types of the lateral extension of protrusions are observed. Occasionally, protrusions (viz. defects residing in deeper layers) that are barely detected under positive sample biases can be pronounced at negative sample biases.[24] The bias polarity dependent STM appearance signifies the bias induced local electronic density state changes rather than topographic protrusions.[29-30] The contribution of defects from subsurface layers is also supported by the atomically resolved STM image inset in Figure 4.1d, where the protrusions only superimpose on the hexagonal $MoTe_2$ lattice without apparent surface adsorbates or vacancies. The central symmetric shape of protrusions and the above STEM observations suggest that each protrusion defect is likely to represent a single intercalated Te atom.

Subsurface dopants or defects that can cause such topographic contrasts (either hillocks or depressions, relying on donor or acceptor identity, spatial positions of defects, as well as the energy levels introduced) and the related tunneling models (including the effect of STM tip-induced band bending) have been extensively discussed in previous STM studies of GaAs, Si, and some TMDs surfaces.[30-35] The height and spatial extension of surface defects can be used as an indication of their subsurface location.[30] Similarly, considering the limited detection depth of the STM and the protrusion aspect ratio in Figure 4.1c and d, intercalated Te atoms residing underneath the subsurface 1st (first), 2nd, and 3rd layers are suggested. If tentatively assuming the apparent protrusions seen in Figure 4.1c to originate from the underlying two layers (extending ~1.4 nm in thickness given their much higher spatial/height resolutions than defects from the third layer), then the 353 protrusions counted in Figure 4.1c would roughly give an estimated defect concentration of 2.5×10^{19} cm-3: much higher than the concentration level of minority impurities detected by the mass spectrometry analysis. Such concentrations are consistent with a majority species: Te.

Given the existence of such high defect concentrations, the chemical stability of the $MoTe_2$ surfaces has been corroborated through air exposure experiments demonstrating that the oxygen uptake does not occur in a significant amount. Only less than 4 at.% of surface oxides (Te/Mo-O bonds) are detected after two days of air exposure. Therefore, the crystal is preserved for the following thermal stability study to examine the role of excess Te as well.

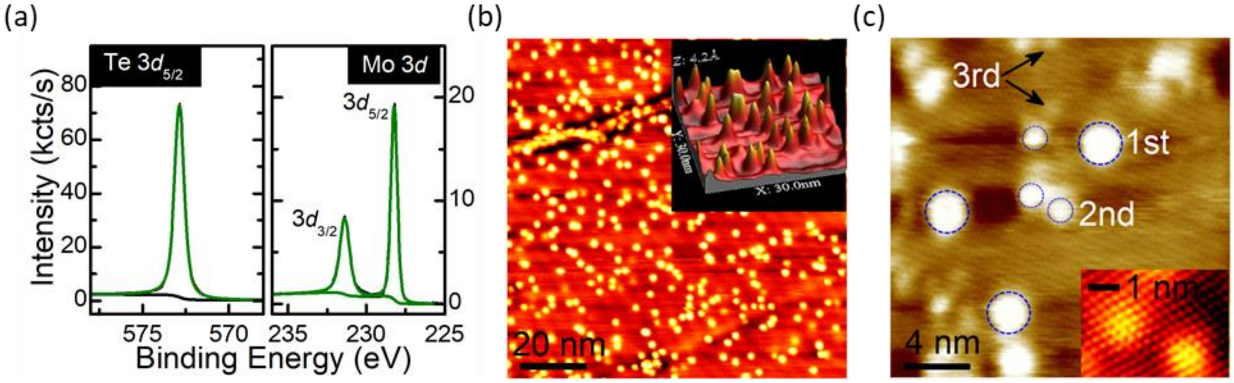

Figure 4.1. Excess Te in intrinsic $MoTe_2$ crystal (a) XPS spectra of Te $3d_{5/2}$ and Mo Mo $3d$ core level regions from a fresh-exfoliated bulk $MoTe_2$. (b-c) STM images of the bulk crystal taken at V_b = -0.6 V and -0.4 V, respectively. A 3D zoom-in image inset in panel (b) indicates the average height of protrusions is 3±0.5 Å. The inset in panel (c) is a 5.5 × 4.0 nm^2 atomically resolved STM image taken at V_b = +0.6 V. The tunneling current for all STM images is I_t = 1.5 A.

Figure 4.2a,b show atomic resolution HAADF-STEM images of a $MoTe_2$ flake (1L, top) and bilayer (2L, bottom) with an atomic number contrast (Z^2 contrast). Two types of point defects are identified: single atoms (indicated as yellow/green arrows) sitting on top of Te triangles (yellow/green triangles) and Te vacancies (green circles). In the 1L region, the image intensity at the Te_2 column sites (top and bottom Te atoms) is higher than that at the Mo atom sites if viewed along its [0001] zone axis. Therefore, Mo/Te atoms and defects can be easily distinguished based on their intensity differences (see the inset intensity line profile). It is noted that the Te atomic vacancies are likely generated by the initial 250 °C annealing, which was employed to remove surface residues from the transferring process, but clearly created some randomly distributed structural defects simultaneously. The STEM imaging was performed at 80 kV, which is much lower than the critical knock-on damage voltage of $MoTe_2$.[36] Since Mo vacancies are seldom observed in the STEM images, the surface adatoms are likely to be Te atoms that result in the high Te/Mo stoichiometry. In Figure 4.2b, the stable sites of the intercalated Te atoms are observed as either aligned with the underlying Mo atoms (indicated as green arrows/triangles) or at the hollow sites of Te triangles (yellow arrows/triangles), suggesting a random adsorption site. The latter case is apparently resolved and dominant in the 2L region. In addition, the in-plane lattice constant extracted from the plan-view HAADF image is 3.5 Å, consistent with the 2H structure reported in the literature.[25]

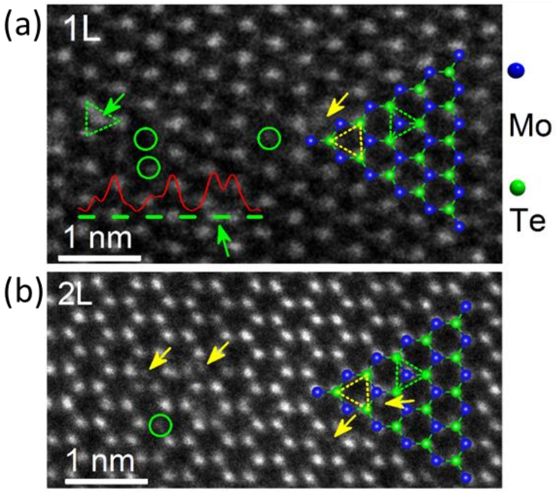

Figure 4.2. Vacancies and adatoms in Te rich-$MoTe_2$ (a) HAHAD-STEM image of a monolayer $MoTe_2$. (b) HAHAD-STEM image of a bilayer $MoTe_2$. Te vacancies and adatoms are indicated by green circles and green/yellow arrows, respectively.

The thermal stability of $MoTe_2$ is investigated with a UHV surface analysis system[16] where the sample is annealed at 200 °C, 300 °C and 400 °C for 2h, 1h, and 0.5h, respectively, and then followed by *in situ* STM analysis after the sample is cooled down to room temperature. Figure 4.3a,b presents the STM morphological evolution of the $MoTe_2$ after annealing at 200 °C and 300 °C, and reveals the poor structural stability of $MoTe_2$. The surface becomes more defective as the annealing temperature increases, which leads to the formation of apparent structural defects such as clusters and pinholes. Representative examples of structural defects are shown in Figure 4.3c-g and obtained from the 300 °C annealed sample surface.

One dominant type of structural defect is presented as bright clusters with arbitrary shapes and sizes (see blue squares in Figure 4.3c,d) and surrounded or centered by dark defects (depressions/pinholes). At 200 °C, these clusters show a as round shapes for sizes less than 3 nm and develop into a triangular-like shape for larger sizes at 300 °C. Examples of triangular clusters can be found in Figure 4.3c,e,g. The dark pinholes/depressions usually have a depth of 7 Å or less, generated by missing one layer Te-Mo-Te segments (see Figure 4.3f,g) or electron depletion introduced by Mo vacancies. Occasionally, depressions without any nearby clusters can also be found on the same sample surface (see white squares in Figure 4.3c,d). The cluster and pinhole/depression relationship indicates the clusters originate mainly from the curling-up/aggregation of un-dissociated particles/segments. STS has been performed on some cluster defects, and reveals a metallic-like behavior of those clusters due to the formation of gap states.

Besides large structural defects, traces of Te atomic vacancies (indicated with white arrows, see Figure 4.3c-g) are also detectable on the zoomed-in STM images. Especially, Te atomic vacancies (see inset in Figure 4.3d) can exist as a monovacancy and divacancy and suggest low formation energy of Te vacancies. However, forming Te atomic vacancies may not necessarily correspond to a decreased Te/Mo atomic ratio on the sample surface. Based on our previous *in situ* XPS study of the 2H-$MoTe_2$-to-Mo_6Te_6 NW transition process,[15] an initial Te/Mo atomic ratio increment stage is present before the 400 °C. The transition phenomenon is attributed to the complicated surface decomposition as well as the out-diffusion of the intercalated Te atoms.

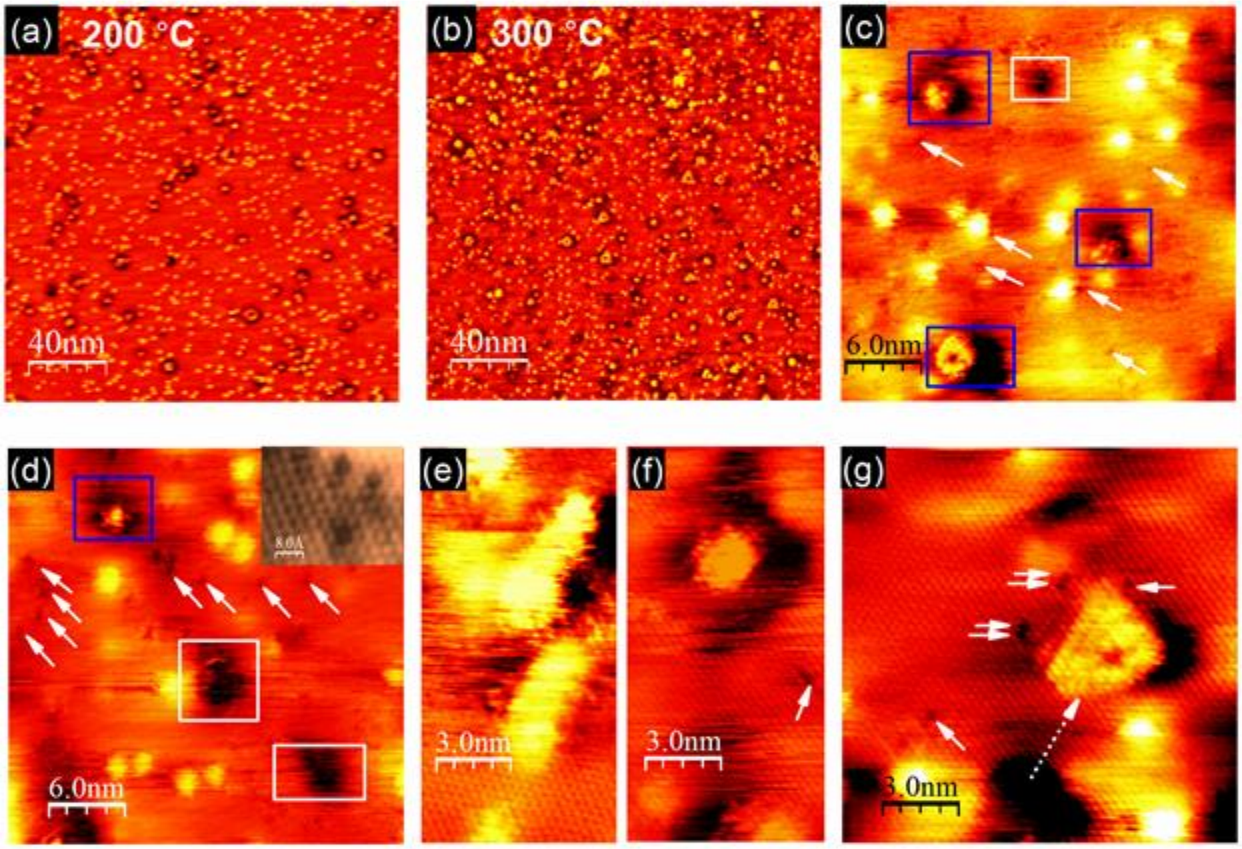

Figure 4.3. STM images of the $MoTe_2$ surface after 200 °C and 300 °C UHV annealing. Large scale images (200×200 nm^2) of $MoTe_2$ at (a) 200 °C and (b) 300 °C, respectively, imaged at V_b = -0.8 and I_t = 0.6 A. (c-g) Example of surface defects generated at 300 °C obtained at V_b = +0.15 V and I_t = 1.5 A. The height/depth of bright clusters (marked with blue squares)/dark depressions (white squares) are measured to be ~7 Å or less. An atomic resolution STM image of Te atomic vacancies (indicated with white arrows) are presented in the inset in panel (d).

4.4.2 STM Characterization of Wagon Wheels

A dramatic change in the surface morphology is immediately observed in Figure 4.4 after annealing the sample to 400 °C for 0.5 h. When imaged at negative sample biases, the topmost layers (Figure 4.4a,b) are almost covered with enlarged layer-type pits and periodic motifs organized in a hexagonal arrangement. Meanwhile, clustering defects and the tunneling contrasts of the underlying intercalated Te atoms are nearly indiscernible on the entire sample surface. The pits have an aerial coverage of 5-10 %, a depth of 7±1 Å (1 monolayer), and can reach a lateral dimension of ~20 nm. As suggested by the dashed lines in Figure 4.4a, the orientation (dashed lines) and the center-to-center distance (see solid lines) of hexagonal arrangements can change locally and are probably interrupted by step edges of pits, boundaries, strains, or local defects. A periodicity ranging from ~3-5 nm has been measured. It is also noted that Mo_6Te_6 NWs mainly generated at 450 °C are occasionally visible at 400 °C along the pit edges (see "streak line" morphologies in Figure 4.4a).

Close examination of STM images recorded at negative sample bias (Figure 4.4c, Vb = -1 V) and at positive sample bias (Figure 4.4d, Vb = +0.4 V), respectively, reveals that such motifs are actually the "axle" of a "wagon-wheel" (WW) pattern: a skewed hexagonal pattern composed of six pairs of twin lines ("spokes" of WW). A high-resolution STM image of such WW networks (Figure 4.4e) reveals that the triangular regions enclosed by the "spokes" possess the same hexagonal arrangement as the initial 2H phase, while the spoke has a twin-line separation of 6.2±1 Å. A similar WW morphology has also been observed for $MoSe_2$ grown on MoS_2,[37-38] HOPG,[39-41] and other substrates and is also recently noted on the MBE grown $MoTe_2$ on MoS_2 with reduced Te flux.[9, 26] The twin-line separation measured here is consistent with the observations on $MoSe_2$ and $MoTe_2$ that it is close to $\sqrt{3}\times a$ (a = 3.5 Å, the 2H-$MoTe_2$ lattice constant).[9, 41] However, this is the first observation of WW structures formed from a bulk 2H-$MoTe_2$ sample, as demonstrated by STM.

The sample-bias dependent morphology contrasts shown in Figure 4.4c-e demonstrate the contribution from localized gap states near the spoke regions. To assess the electronic characteristics of the WW structure, STS measurements (Figure 4.4f) are performed at the triangular center and spoke regions, respectively, and directly compared with the initial 2H phase. As shown, the triangular center shows a rigid downward shift of ~0.12 eV with respect to the initial 2H phase, whereas the spoke region has a similar CBM as the triangular center, but its valence band maximum (VBM) is upward bent towards the Fermi level due to the metallic property of the spoke.[9, 41-42] However, with the interaction of underlying semiconducting $MoTe_2$, it is challenging to uniquely resolve the metallic property of the spoke.

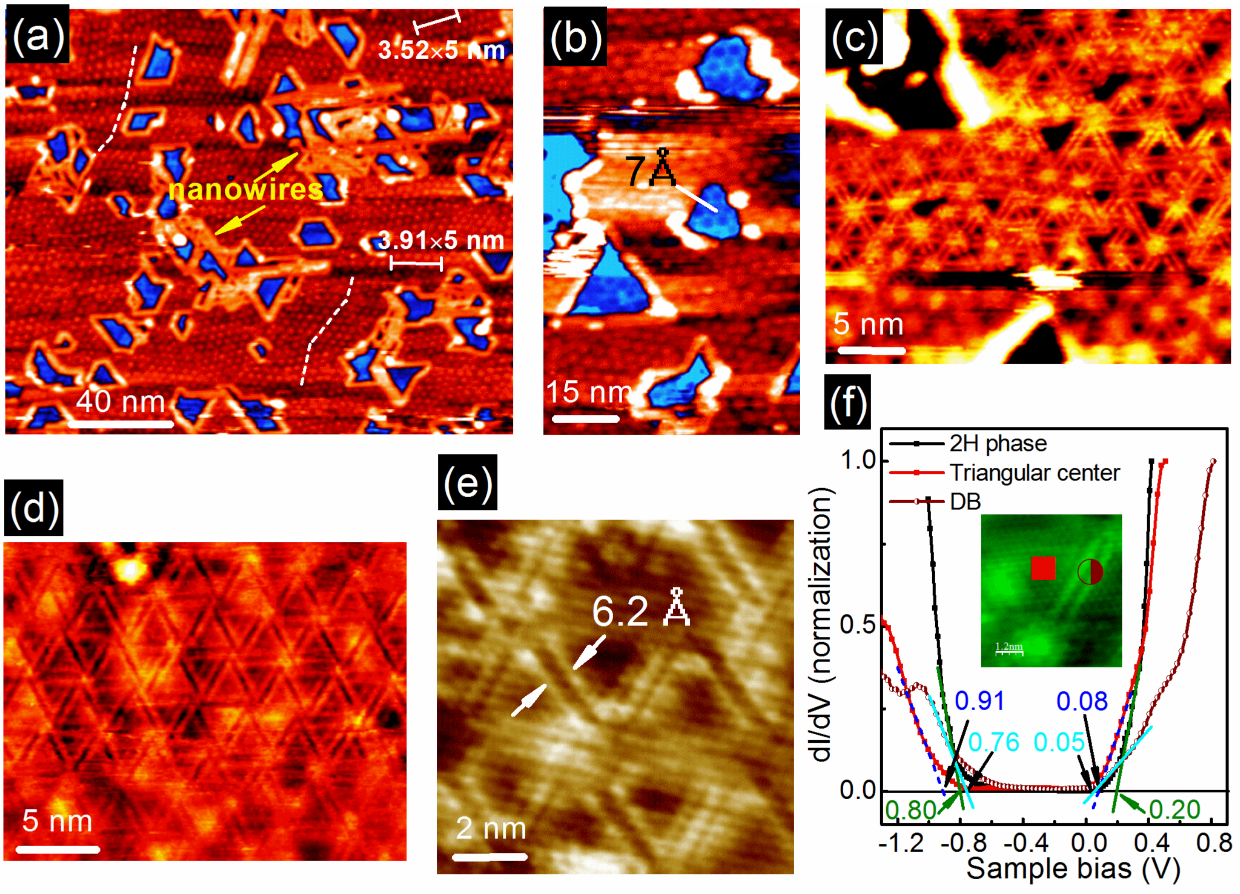

Figure 4.4. (a) 200 × 170 nm^2 and (b) 60 × 100 nm^2 STM images of the $MoTe_2$ surface after the 400 °C annealing, recorded at I_t = 0.6 nA and V_b = -0.8 V and -0.6 V, respectively. The topmost and the exposed sublayer through large pits are covered with hexagonal motifs with an irregular periodicity (3-5 nm) that changes locally. The depth of pits relative to the substrate is measured to be 7±1 Å. (c) 40 × 35 nm^2 and (d) 25 × 20 nm^2 STM images of the zoomed-in surface taken at

opposite sample biases showing the wagon wheel network of twin line boundaries. The (c, d) images are taken at V_b = -0.4 V and +0.4 V, respectively, and at I_t = 1 nA, (e) 10 × 10 nm^2 atomic resolution of WW patterns (V_b = +0.2 V and I_t = 0.6 nA) showing the twin line separation of 6.2±1 Å and the same trigonal atomic arrangement as the 2H phase inside the triangular region. (f) STS measurements on triangular center (square) and IDB (circle) and compared with that on the initial 2H-$MoTe_2$.

4.4.3 TEM Characterization of Inversion Domain Boundaries

The generation of the WW networks on $MoSe_2$ or $MoTe_2$ was initially interpreted as a moiré interference caused by lattice mismatches or rotation between two materials[26, 38, 43] and was later demonstrated to be the result of the chalcogen vacancy induced inversion domain boundary (IDB) formation.[9, 42, 44] Although moiré interference can be involved and change the morphology contrast of IDBs and the domains enclosed by IDBs,[41-42] in this work, the comprehensive STM (Figure 4.4) and subsequent STEM study (Figure 4.5) confirms the IDB structure of the twin-lines and directly rules out the moiré/interference effect. First, the WW patterns shown in STM images do not have a long-range periodicity/orientation as a moiré interference pattern would, and moiré interference is not observed in the domain regions. Second, the existence of the WW morphology is independent of substrates, which has been confirmed in monolayer and bilayer $MoTe_2$ (see Figure 4.5) through the STEM imaging on a $MoTe_2$ flake which has been flashed to 450 °C for one minute and then quickly cooled down.

WWs exhibit a strong pattern of irregularity. Figure 4.5a shows two WW patterns in one monolayer region, in which the domain sizes in the bottom WW are not identical, and the bottom WW would have the same axle structure as the top one, if one IDB (indicated by a yellow line) can translate downward by one lattice vector. To enhance the domain contrast, the Mo edge of the IDBs in the simulated STEM image (Figure 4.5c) are highlighted with green and red colors to outline domain shapes and orientations. In Figure 4.5c, WWs of different sizes and orientations are observed, and this monolayer region has been tailored irregularly by continuous or discontinuous IDBs with W shapes, rotational (or enclosed) triangular shapes, or just kink shapes. This may be the reason why the periodicity and orientation of WWs change in the STM images. Except for the WW morphology, single triangular domain and different domain morphologies have also been found through the STM and STEM studies. Nevertheless, it is difficult to distinguish which group color represents the pristine domain or the inversion domain as each type of domain has comparable coverage and can be interconnected. Figure 4.5d shows a STEM image of bilayer $MoTe_2$ with IDBs. The irregular patterns and the intensity difference at different atomic positions indicates that there are plenty of IDBs in both layers. Figure 4.5e-f show the STEM image simulation when a IDB is overlaid on a pristine $MoTe_2$ and a $MoTe_2$ with IDBs, respectively. The experimental result perfectly matches with the second simulation, indicating that IDBs are formed in both layers of $MoTe_2$.

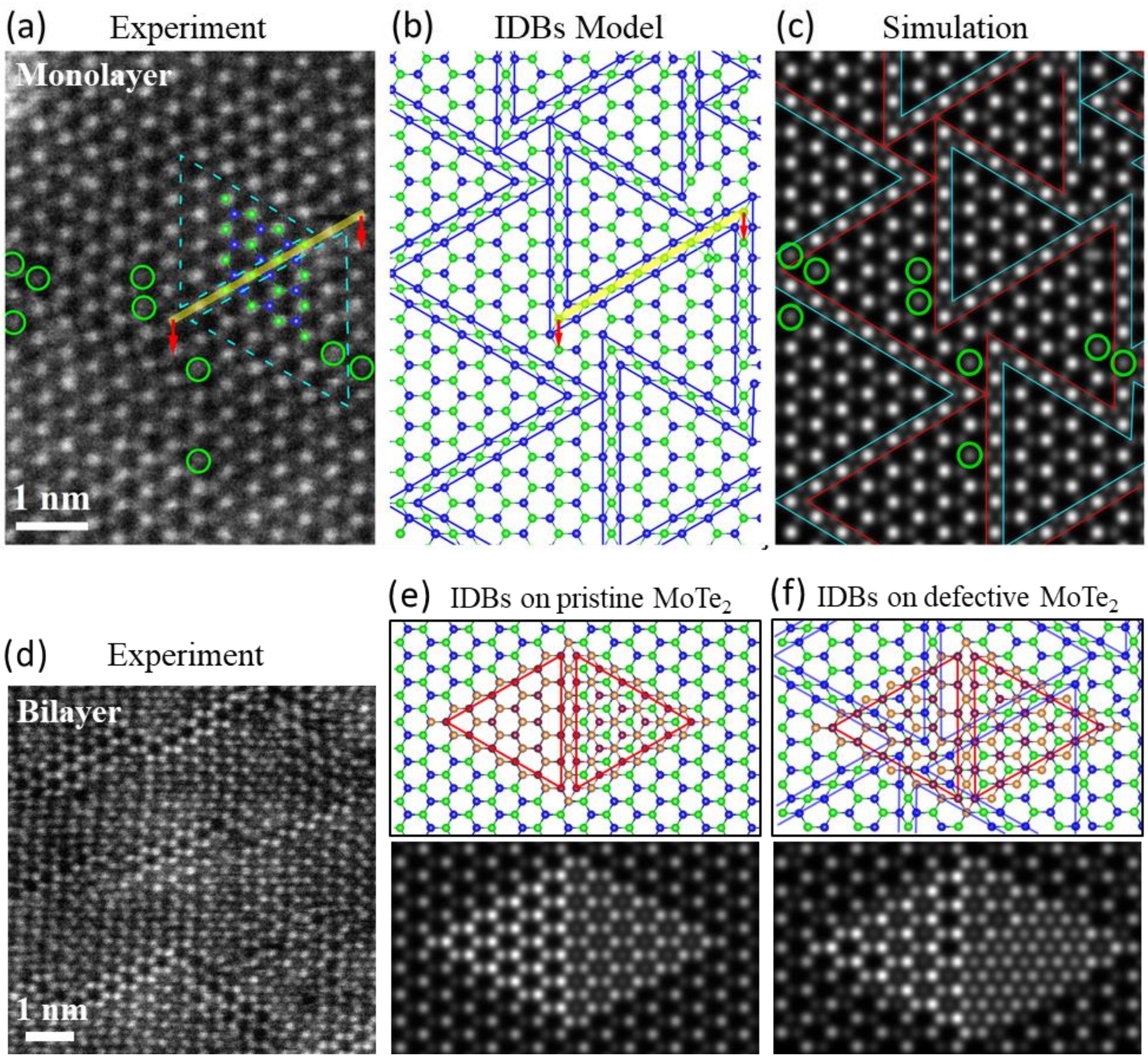

Figure 4.5. Atomic structure of IDBs on monolayer and bilayer $MoTe_2$ after 450 °C flash annealing for 1 min. (a) A Z-contrast STEM image of two neighboring wagon wheel (WW) patterns in monolayer $MoTe_{2.}$ (b,c) WW atomic model along with its STEM simulation image. Colored lines outline the domain boundaries and green circles indicate the Te single vacancies. (d) A Z-contrast STEM image of a bilayer $MoTe_2$ with IDBs. (e) Atomic model and STEM image simulation of IDBs on a pristine monolayer $MoTe_2$. (f) Atomic model and STEM image simulation of IDBs on a defective monolayer $MoTe_2$. Scale bars: 1nm.

After the 450 °C spike annealing, the STEM sample is then slowly reannealed from room temperature to 450 °C. It is found that the domain morphology can change extremely fast during the reannealing process. Figure 4.6a-c shows three sequential STEM images of one monolayer region at 250 °C, where the positions of IDBs are labeled with yellow lines to display the fast development of IDBs with time. These images demonstrate that IDBs can grow, migrate, and disappear easily at even lower temperature, thereby all the WWs morphologies observed in STM and STEM images are probably just intermediate states. The observations also suggest a kinetic process resulting in the formation and translation of WWs.

The atomic structure of IDBs is one type of 60° IDBs containing a line of Te_2 dimers surrounded by (four) two-fold symmetric, Mo atoms along with the zigzag directions (<11-20> directions) of the $MoTe_2$ lattice. Other than the commonly suggested mirror-symmetric inversion domain accompanied by this type of IDBs, the inversion domain is usually shifted away from the mirror-symmetric positions by one lattice vector along the IDBs (see shifted blue lines along the IDBs in Figure 4.5c).[44-45] As each Mo atom at IDBs retains six Te atoms surrounded, the local stoichiometry of IDBs decreases from $MoTe_2$ to $MoTe_{1.5}$ (Mo_4Te_6),[44-45] indicating a Te deficiency. Meanwhile, there is no particular mass loss along the Te_2 line at the IDBs, suggesting the formation mechanism of this type IDBs on $MoTe_2$ is slightly different from what is reported driven by chalcogen line vacancies.[44, 46] Generally, chalcogen line vacancies are more favorable than random single vacancies at high temperatures due to the lowered formation energy.[46]

Komsa et al. have shown the mobile and agglomeration of single S vacancies into line defects under the electron beam exposure of MoS_2 in the TEM.[47] However, Lin et al. also demonstrate the migration/growth of the same type of $MoSe_{1.5}$ IDBs in $MoSe_2$ is driven by Se atomic vacancy and gliding of Mo atoms.[47] The latter explanation is more reasonable for the development/migration of IDBs in $MoTe_2$. In Figure 4.5a-c, the displacement of Mo atoms can be monitored/measured when using Te positions as the reference. To illustrate the gliding/displacement of Mo atoms, close-up views of the same region and the corresponding atomic structures are displaced at the bottom panel in Figure 4.6a-c, in which Mo atoms are colored differently to indicate the location of Mo atoms at different sites while the arrows show the displacement direction of those Mo atoms for the next frame. It seems that the movement of Mo atoms is a random process. This may be related to the random locations of Te vacancies and the characteristics of their random migrations. The latter is indicated by the appearance (and disappearance) of Te vacancies that are marked in the zoomed-in regions in Figure 4a-c (see green and red circles). Occasionally, the hopping and migration of surface Te adatoms from either the intercalated Te source or the pristine lattice are also observable, making the analysis of the detailed mechanism even more difficult. Nevertheless, it is certain that the final IDB morphology is unpredictable from the random migration and generation of Te vacancies during the annealing process.

In this STEM study, Te vacancies are more frequently detected as single vacancies, di-vacancies, or Te_2 column vacancies rather than Te line vacancies. Further, Te deficiency will facilitate the formation of either Mo_6Te_6 NWs or $MoTe_2$ layer-type defects (see regional pits and Mo_6Te_6 NWs in Figure 4.4a).[15] Therefore, the thermal degradation of $MoTe_2$ crystals is mainly caused by the low Te-Mo bonding strength itself, independent of the unexpected Te doping from the crystal growth process.

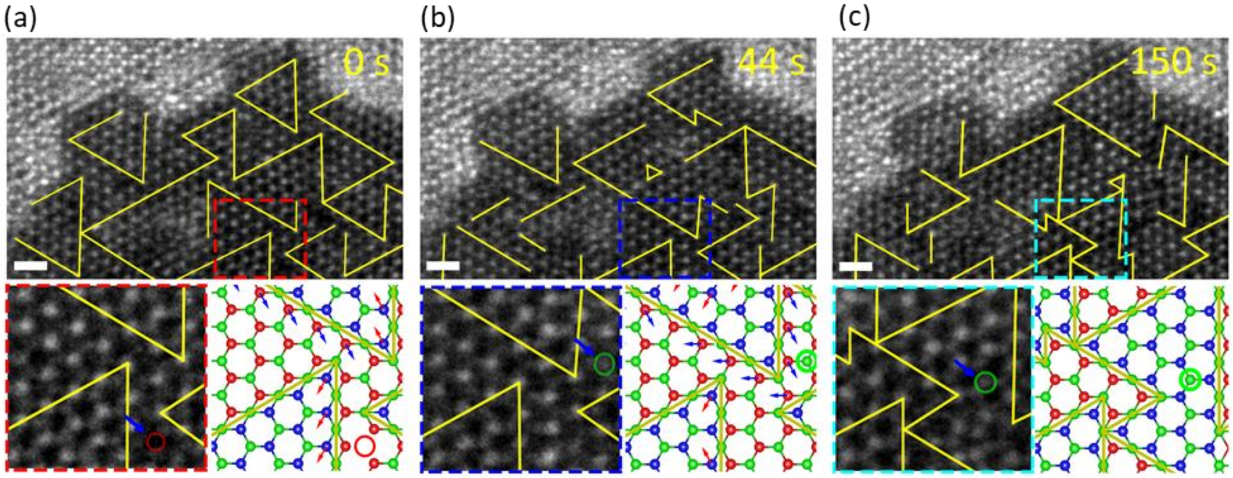

Figure 4.6. Z-contrast STEM images showing the fast transformation of IDBs upon reannealing at 250 °C. High resolution STEM images (bottom left) and the corresponding schematic models (bottom right) highlight the IDB migration driven by the gliding of Mo atoms. Arrows in the schematic models indicate the displacement direction of Mo atoms during the IDB migration process. Green/red circles suggest the relocation of the as-formed Te single vacancy/Te_2 column vacancy (missing the top and bottom Te atoms) during the annealing process. Scale bars: 1nm.

4.4.4 Influence of Vacancy on Inversion Domain Boundaries

In section 4.4.3, we show that a domain boundary is created in 2H-$MoTe_2$ flake if a Mo atom glides to its neighboring hollow site. In this section, the role of Te vacancies during the evolution of IDBs is identified through serial imaging of a monolayer $MoTe_2$ with IDBs. Te vacancy induced Mo migration is crucial to the formation of IDBs. During the *in situ* annealing, the creation or annihilation of Te vacancies is achieved via the hopping of Te atoms on the flake. The energy barrier for a Mo atom to glide to its neighboring site decreases if a Te vacancy is created next to this Mo atom.

To track the Te hopping and Mo migration more accurately, a faster scanning is applied during the image acquisition. Figure 4.7 presents the *in situ* observation of an IDB development.

The time sequence STEM images are acquired at 150 °C with a time interval of 6 s per frame (Figure 4.7A-E). The corresponding image simulations and the atomic models are shown in Figure 4.7F-J and Figure 4.7K-O, respectively. At t = 0 s, three Mo atoms, labeled by the yellow circles in Figure 4.7A, start to glide along the upper right direction to their neighboring hollow sites. Interestingly, there is a Te single vacancy (highlighted by white arrow) next to the first Mo atom, as a result, the gliding of this Mo atom is easier to happen. Moreover, as shown in Figure 4.7K, this Mo atom (in cyan color, highlighted by a yellow circle) is located at the corner where two IDBs meet. So it is surrounded by two Mo atoms (in blue color) from the adjacent domains. The distance between this Mo atom (in cyan color) and its neighboring two Mo atoms (in blue color) is about 2 Å, which is much smaller than the distance of Mo-Mo in 2H-$MoTe_2$ (3.5Å). The densely packed environment, together with the Te vacancy next to it, forces Mo to glide toward the direction with less atomic concentration to reduce its energy. At t = 6 s, as shown in Figure 4.7B, three Mo atoms migrate to their new positions, form a flat domain boundary. Limited by the scan rate, we captured 3 Mo atoms migration between the two frames (with a 6 s interval). Similarly, a newly densely packed environment of Mo atoms is formed in Figure 4.7B. The two Mo atoms, highlighted by the yellow circles, tend to glide in a similar manner to their upper right directions. As the similar operation continues, as shown in Figure 4.7C-D, a long and flat domain boundary is formed (Figure 4.7E). However, the morphology of an IDB is unpredictable due to the random migration/generation of Te vacancies and the gliding of Mo atoms. Therefore, the development of IDBs in the flake is a dynamic process during the vacuum annealing.

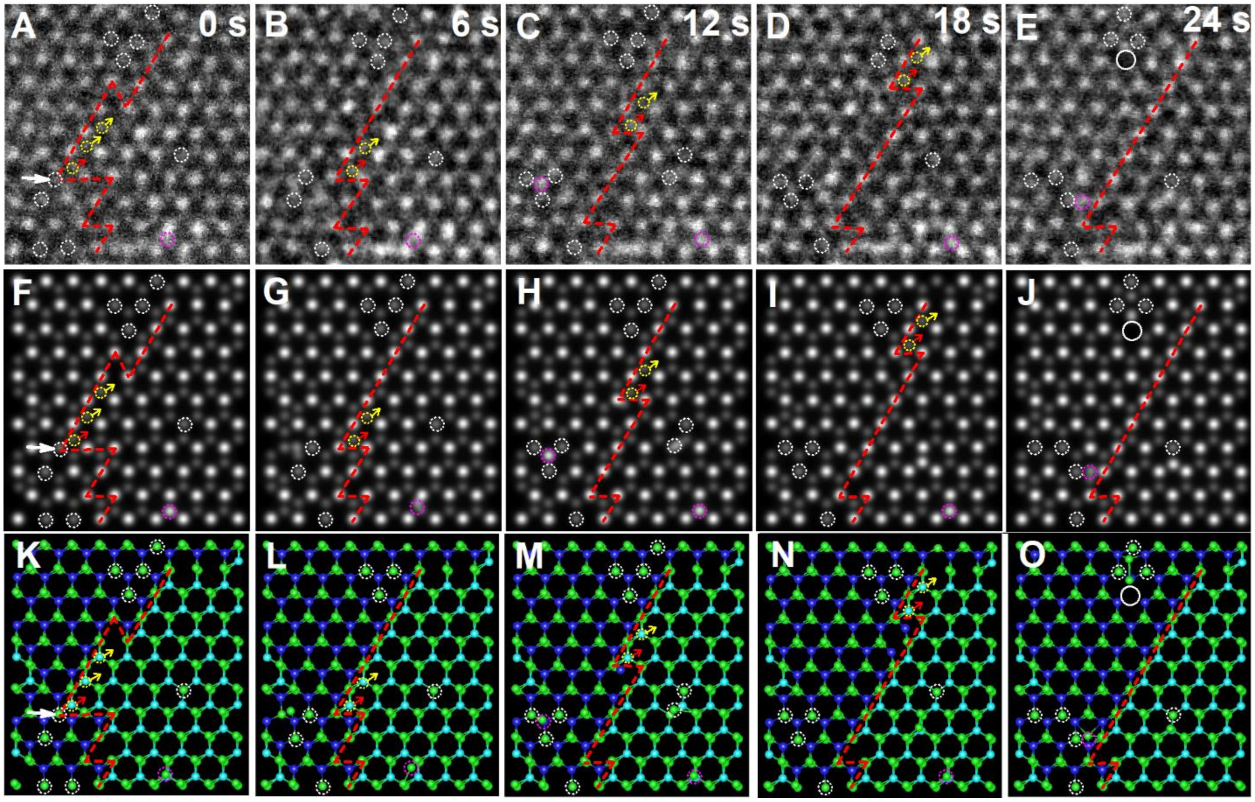

Figure 4.7. Vacancy migration induced the IDB dynamics (A-E) Sequential STEM images showing the migration of Mo atoms and the change of IDB. (F-J) STEM image simulation correlating with the experimental result. (K-O) The corresponding atomic models in A-E. The inversion grain boundary is highlighted with the red dashed line. Mo atoms of the neighboring domains are labelled with blue and cyan color, respectively. The migration of Mo atoms along the domain boundary and their migration directions are highlighted using the yellow circles and yellow/red arrows, respectively. Vacancies and ad-atoms are highlighted with white and purple circles.

4.5 Conclusions

In summary, we investigate the thermal stability of $MoTe_2$ and the role of excess Te that is present within the CVT-synthesized $MoTe_2$ crystals. The excess Te does not affect the underlying crystallinity or lower the chemical stability, but only induces n-type doping of the synthesized $MoTe_2$ crystals. The heating treatment can result in excess of surface/intercalated Te. However, the poor structural stability can also enable the desorption of the bonded Te as well. Te vacancies are easily formed at a temperature as low as 200 °C, and facilitate one type of 60° inversion domain boundaries at the 400 °C, which is further intertwined as a wagon wheel morphology when the domain boundary intensity increases. The Te deficiency at higher temperatures leads to the formation of either Mo_6Te_6 NWs or substantial pits/holes so that it is difficult to maintain the hexagonal lattice structure for $MoTe_2$.[15] Furthermore, the role of Te vacancies on the evolution of inversion domain boundaries is extensively investigated. The work demonstrates a particularly low thermal stability of $MoTe_2$ even with an excess of Te inside. Importantly, it is also demonstrated that effective passivation of $MoTe_2$ is of crucial importance in enhancing its thermal stability and chemical stability.

4.6 References

1. Keum, D. H.; Cho, S.; Kim, J. H.; Choe, D. H.; Sung, H. J.; Kan, M.; Kang, H.; Hwang, J. Y.; Kim, S. W.; Yang, H.; Chang, K. J.; Lee, Y. H., Bandgap Opening in Few-Layered Monoclinic MoTe2. *Nat. Phys.* **2015,** *11*, 482.

2. Cho, S.; Kim, S.; Kim, J. H.; Zhao, J.; Seok, J.; Keum, D. H.; Baik, J.; Choe, D.; Chang, K. J.; Suenaga, K.; Kim, S. W.; Lee, Y. H.; Yang, H., Phase Patterning for Ohmic Homojunction Contact in MoTe2. *Science* **2015,** *349*, 625.

3. Zhou, Y.; Reed, E. J., Structural Phase Stability Control of Monolayer MoTe2 with Adsorbed Atoms and Molecules. *J. Phys. Chem. C* **2015,** *119*, 21674.

4. Vellinga, M. B.; de Jonge, R.; Haas, C., Semiconductor to Metal Transition in MoTe2. *J. Solid State Chem.* **1970,** *2*, 299.

5. Song, S.; Keum, D. H.; Cho, S.; Perello, D.; Kim, Y.; Lee, Y. H., Room Temperature Semiconductor-Metal Transition of MoTe2 Thin Films Engineered by Strain. *Nano Lett.* **2016,** *16*, 188.

6. Zhang, C.; Kc, S.; Nie, Y.; Liang, C.; Vandenberghe, W. G.; Longo, R. C.; Zheng, Y.; Kong, F.; Hong, S.; Wallace, R. M.; Cho, K., Charge Mediated Reversible Metal-Insulator Transition in Monolayer MoTe2 and WxMo1-xTe2 Alloy. *ACS Nano* **2016,** *10*, 7370.

7. Roy, A.; Movva, H. C. P.; Satpati, B.; Kim, K.; Dey, R.; Rai, A.; Pramanik, T.; Guchhait, S.; Tutuc, E.; Banerjee, S. K., Structural and Electrical Properties of MoTe2 and MoSe2 Grown by Molecular Beam Epitaxy. *ACS Appl. Mater. Interfaces* **2016,** *8*, 7396.

8. Park, J. C.; Yun, S. J.; Kim, H.; Park, J. H.; Chae, S. H.; An, S. J.; Kim, J. G.; Kim, S. M.; Kim, K. K.; Lee, Y. H., Phase-Engineered Synthesis of Centimeter-Scale 1T′- and 2H-Molybdenum Ditelluride Thin Films. *ACS Nano* **2015,** *9*, 6548.

9. Diaz, H. C.; Ma, Y.; Chaghi, R.; Batzill, M., High Density of (Pseudo) Periodic Twin-Grain Boundaries in Molecular Beam Epitaxy-Grown van Der Waals Heterostructure: MoTe2/MoS2. *Appl. Phys. Lett.* **2016,** *108*, 191606.

10. Naylor, C. H.; Parkin, W. M.; Ping, J.; Gao, Z.; Zhou, Y. R.; Kim, Y.; Streller, F.; Carpick, R. W.; Rappe, A. M.; Drndic, M.; Kikkawa, J. M.; Johnson, A. T. C., Monolayer Single-Crystal 1T′-MoTe2 Grown by Chemical Vapor Deposition Exhibits a Weak Antilocalization Effect. *Nano Lett.* **2016,** *16*, 4297.

11. Zhou, L.; Xu, K.; Zubair, A.; Liao, A. D.; Fang, W.; Ouyang, F.; Lee, Y. H.; Ueno, K.; Saito, R.; Palacios, T.; Kong, J.; Dresselhaus, M. S., Large-Area Synthesis of High-Quality Uniform Few-Layer MoTe2. *J. Am. Chem. Soc.* **2015,** *137*, 11892.

12. Brainard, W. A., *The thermal stability and friction of the disulfides, diselenides, and ditellurides of molybdenum and tungsten in vacuum (109̄ to 106̄ torr)*. National Aeronautics and Space Administration: 1968.

13. Gamble, F. R., Ionicity, Atomic Radii, and Structure in the Layered Dichalcogenides of Group IVb, Vb, and VIb Transition Metals. *J. Solid State Chem.* **1974,** *9*, 358.

14. Bernède, J. C.; Amory, C.; Assmann, L.; Spiesser, M., X-Ray Photoelectron Spectroscopy Study of MoTe2 Single Crystals and Thin Films. *Appl. Surf. Sci.* **2003,** *219*, 238.

15. Zhu, H.; Wang, Q.; Zhang, C.; Addou, R.; Cho, K.; Wallace, R. M.; Kim, M. J., New Mo6Te6 Sub-Nanometer-Diameter Nanowire Phase from 2H-MoTe2. *Adv. Mater.* **2017,** *29*, 1606264.

16. Wallace, R. M., In-Situ Studies on 2D Materials. *ECS Trans.* **2014,** *64*, 109.

17. Herrera-Gómez, A.; Hegedus, A.; Meissner, P. L., Chemical Depth Profile of Ultrathin Nitrided SiO2 Films. *Appl. Phys. Lett.* **2002,** *81*, 1014.

18. Lin, J.; Lin, Y. C.; Wang, X.; Xie, L.; Suenaga, K., Gentle Transfer Method for Water- and Acid/alkali-Sensitive 2D Materials for (S)TEM Study. *APL Mater.* **2016,** *4*, 116108.

19. Ishizuka, K. In *DeConvHAADF: Software cs-corrector for STEM-HAADF microscopy*, Proc. 8th Asia-Pacific Conference on Electron Microscopy, 2004.

20. Addou, R.; Wallace, R. M., Surface Analysis of WSe2 Crystals: Spatial and Electronic Variability. *ACS Appl. Mater. Interfaces* **2016,** *8*, 26400.

21. Suk, J. W.; Kitt, A.; Magnuson, C. W.; Hao, Y.; Ahmed, S.; An, J.; Swan, A. K.; Goldberg, B. B.; Ruoff, R. S., Transfer of CVD-Grown Monolayer Graphene onto Arbitrary Substrates. *ACS Nano* **2011,** *5*, 6916.

22. Cheng, L.; Jandhyala, S.; Mordi, G.; Lucero, A. T.; Huang, J.; Azcatl, A.; Addou, R.; Wallace, R. M.; Colombo, L.; Kim, J., Partially Fluorinated Graphene: Structural and Electrical Characterization. *ACS Appl. Mater. Interfaces* **2016,** *8*, 5002.

23. Lin, Z.; Carvalho, B. R.; Kahn, E.; Lv, R.; Rao, R.; Terrones, H.; Pimenta, M. A.; Terrones, M., Defect Engineering of Two-Dimensional Transition Metal Dichalcogenides. *2D Mater.* **2016,** *3*, 22002.

24. Zhu, H.; Wang, Q.; Cheng, L.; Addou, R.; Kim, J.; Kim, M. J.; Wallace, R. M., Defects and surface structural stability of MoTe2 under vacuum annealing. *ACS Nano* **2017,** *11* (11), 11005-11014.

25. Tang, S.; Kasowski, R.; Parkinson, B., Scanning Tunneling Microscopy of the Subsurface Structures of Tungsten Ditelluride and Molybdenum Ditelluride. *Phys. Rev. B: Condens. Matter Mater. Phys.* **1989,** *39*, 9987.

26. Diaz, H. C.; Chaghi, R.; Ma, Y.; Batzill, M., Molecular Beam Epitaxy of the van Der Waals Heterostructure MoTe2 on MoS2: Phase, Thermal, and Chemical Stability. *2D Mater.* **2015,** *2*, 1.

27. Caulfield, J. C.; Fisher, A. J., Electronic Structure and Scanning Tunnelling Microscope Images of Missing-Atom Defects on MoS2 and MoTe2 Surfaces. *J. Phys.: Condens. Matter* **1997,** *9*, 3671.

28. Lezama, I. G.; Ubaldini, A.; Longobardi, M.; Giannini, E.; Renner, C.; Kuzmenko, A. B.; Morpurgo, A. F., Surface Transport and Band Gap Structure of Exfoliated 2H-MoTe2 Crystals. *2D Mater.* **2014,** *1*, 21002.

29. Matthes, T. W.; Sommerhalter, C.; Rettenberger, A.; Bruker, P.; Boneberg, J.; Lux-Steiner, M. C.; Leiderer, P., Imaging of Dopants in Surface and Sub-Surface Layers of the Transition Metal Dichalcogenides WS2 and WSe2 by Scanning Tunneling Microscopy. *Appl. Phys. A: Mater. Sci. Process.* **1998,** *66*, 1007.

30. Zheng, J. F.; Liu, X.; Newman, N.; Weber, E. R.; Ogletree, D. F.; Salmeron, M., Scanning Tunneling Microscopy Studies of Si Donors (SiGa) in GaAs. *Phys. Rev. Lett.* **1994,** *72*, 1490.

31. Johnson, M. B.; Albrektsen, O.; Feenstra, R. M.; Salemink, H. W. M., Direct Imaging of Dopants in GaAs with Cross-Sectional Scanning Tunneling Microscopy. *Appl. Phys. Lett.* **1993,** *63*, 2923.

32. Sinthiptharakoon, K.; Schofield, S. R.; Studer, P.; Brázdová, V.; Hirjibehedin, C. F.; Bowler, D. R.; Curson, N. J., Investigating Individual Arsenic Dopant Atoms in Silicon Using Low-Temperature Scanning Tunnelling Microscopy. *J. Phys.: Condens. Matter* **2014,** *26*, 12001.

33. Sommerhalter, C.; Matthes, T. W.; Boneberg, J.; Lux-Steiner, M. C.; Leiderer, P., Investigation of Acceptors in P-Type WS2 by Standard and Photo-Assisted Scanning Tunneling Microscopy/spectroscopy. *Appl. Surf. Sci.* **1999,** *144*, 564.

34. van der Wielen, M. C. M. M.; van Roij, A. J. A.; van Kempen, H., Direct Observation of Friedel Oscillations around Incorporated SiGa Dopants in GaAs by Low-Temperature Scanning Tunneling Microscopy. *Phys. Rev. Lett.* **1996,** *76*, 1075.

35. Whangbo, M. H.; Ren, J.; Magonov, S. N.; Bengel, H.; Parkinson, B. A.; Suna, A., On the Correlation between the Scanning Tunneling Microscopy Image Imperfections and Point Defects of Layered Chalcogenides 2H-MX2 (M = Mo, W; X = S, Se). *Surf. Sci.* **1995,** *326*, 311.

36. Komsa, H. P.; Kotakoski, J.; Kurasch, S.; Lehtinen, O.; Kaiser, U.; Krasheninnikov, A. V., Two-Dimensional Transition Metal Dichalcogenides under Electron Irradiation: Defect Production and Doping. *Phys. Rev. Lett.* **2012,** *109*, 1.

37. Parkinson, B. A.; Ohuchi, F. S.; Ueno, K.; Koma, A., Periodic Lattice Distortions as a Result of Lattice Mismatch in Epitaxial Films of Two-Dimensional Materials. *Appl. Phys. Lett.* **1991,** *58*, 472.

38. Murata, H.; Koma, A., Modulated STM Images of Ultrathin MoSe2 Films Grown on MoS2(0001) Studied by STM/STS. *Phys. Rev. B: Condens. Matter Mater. Phys.* **1999,** *59*, 10327.

39. Liu, H.; Zheng, H.; Yang, F.; Jiao, L.; Chen, J.; Ho, W.; Gao, C.; Jia, J.; Xie, M., Line and Point Defects in MoSe2 Bilayer Studied by Scanning Tunneling Microscopy and Spectroscopy. *ACS Nano* **2015,** *9*, 6619.

40. Jiao, L.; Liu, H. J.; Chen, J. L.; Yi, Y.; Chen, W. G.; Cai, Y.; Wang, J. N.; Dai, X. Q.; Wang, N.; Ho, W. K.; Xie, M. H., Molecular-Beam Epitaxy of Monolayer MoSe2: Growth Characteristics and Domain Boundary Formation. *New J. Phys.* **2015,** *17*, 53023.

41. Liu, H.; Jiao, L.; Yang, F.; Cai, Y.; Wu, X.; Ho, W.; Gao, C.; Jia, J.; Wang, N.; Fan, H.; Yao, W.; Xie, M., Dense Network of One-Dimensional Midgap Metallic Modes in Monolayer MoSe2 and Their Spatial Undulations. *Phys. Rev. Lett.* **2014,** *113*, 66105.

42. Barja, S.; Wickenburg, S.; Liu, Z.; Zhang, Y.; Ryu, H.; Ugeda, M. M.; Hussain, Z.; Shen, Z. X.; Mo, S.; Wong, E.; Salmeron, M. B.; Wang, F.; Crommie, M. F.; Ogletree, D. F.; Neaton, J. B.; Weber-Bargioni, A., Charge Density Wave Order in 1D Mirror Twin Boundaries of Single-Layer MoSe2. *Nat. Phys.* **2016,** *12*, 751.

43. Kobayashi, K., Moiré Patterns in Scanning Tunneling Microscopy Images of Layered Materials. *J. Vac. Sci. Technol., B: Microelectron. Process. Phenom.* **1996,** *14*, 1075.

44. Lin, J.; Pantelides, S. T.; Zhou, W., Vacancy-Induced Formation and Growth of Inversion Domains in Transition-Metal Dichalcogenide Monolayer. *ACS Nano* **2015,** *9*, 5189.

45. Zhou, W.; Zou, X.; Najmaei, S.; Liu, Z.; Shi, Y.; Kong, J.; Lou, J.; Ajayan, P. M.; Yakobson, B. I.; Idrobo, J. C., Intrinsic structural defects in monolayer molybdenum disulfide. *Nano Lett.* **2013,** *13*, 2615.

46. Lehtinen, O.; Komsa, H.; Pulkin, A.; Whitwick, M. B.; Chen, M.; Lehnert, T.; Mohn, M. J.; Yazyev, O. V.; Kis, A.; Kaiser, U.; Krasheninnikov, A. V., Atomic Scale Microstructure and Properties of Se-Deficient. *ACS Nano* **2015,** *9*, 3274.

47. Komsa, H. P.; Kurasch, S.; Lehtinen, O.; Kaiser, U.; Krasheninnikov, A. V., From Point to Extended Defects in Two-Dimensional MoS2: Evolution of Atomic Structure under Electron Irradiation. *Phys. Rev. B: Condens. Matter Mater. Phys.* **2013,** *88*, 035301.

CHAPTER 5

CONCLUSIONS AND FUTURE WORK

5.1 Conclusions

This dissertation focuses mainly on the characterization of the defects and phase transition in $MoTe_2$ flake (monolayer, bilayer, and few layers). We investigate the structural, chemical, and electrical properties of $MoTe_2$ using various *in situ* techniques, including STM, TEM, XPS, and Raman.

In Chapter 2, a flake transfer method with a low concentration of carbon residue for *in situ* heating experiment is developed. A lamella fabrication method for *in situ* electrical-biasing experiment is demonstrated.

In Chapter 3, a novel Mo_6Te_6 nanowire phase transition in 2H-$MoTe_2$ by vacuum annealing is extensively investigated. We first observe the 2H-NW phase transition for the few layers $MoTe_2$ and find out that the NWs propagate along the 2H-$MoTe_2$ <11-20> directions when the flake is annealed at 450 °C. Then, we explore the phase transition in monolayer and bilayer $MoTe_2$ and observes a novel NW-terminated edges at 400 °C. Lastly, we investigate the influence of carbon residue on the phase stability during the vacuum annealing and prove that a clean $MoTe_2$ flake with a low concentration of carbon residue is required for the NW phase transition.

In Chapter 4, the thermal stability of $MoTe_2$ is comprehensively explored. Firstly, the structures and electronic properties of the surface defects in $MoTe_2$ are carried out using *in situ* STM and XPS. Then, a Wagon Wheel pattern is observed in $MoTe_2$ after 400 °C vacuum annealing using STM. After that, the atomic structure of the Wagon Wheel pattern is characterized using *in* *situ* TEM. We confirm that the Wagon Wheel pattern is the boundary of the inversion domains in $MoTe_2$. The formation of inversion domains indicates the poor thermal stability of $MoTe_2$ under annealing. Lastly, we observe the transformation of inversion domains using the serial STEM imaging and confirm the role of Te vacancies for the evolution of inversion domains.

5.2 Future Work

Appendices show the current ongoing work for the *in situ* electrical-biasing study of the phase transition in $MoTe_2$ under a strong electrical field. These tasks are expected to finish soon. According to the previous publications, a 1T’ phase or an unknown structural transition could be observed. However, based on our preliminary results, the Mo_6Te_6 NW phase, rather than the 1T’ phase, was observed. It might be the result of joule-heating when a large current was applied. The optimization of experiment parameters, such as the selection of the proper biasing voltage and the issue of discharge that causes TEM lamella damage, needs to be investigated in detail. Moreover, the TMD/metal interface is also an interesting research topic for the electrical-biasing study. The influence of different interfaces between TMDs (MoS_2, $MoSe_2$, $MoTe_2$, WSe_2, etc.) and electrodes (Au, Cr, etc.) will be investigated.

APPENDIX A

PRELIMINARY RESULT OF *IN SITU* ELECTRICAL STUDY OF MOTE$_2$

A.1 Specimen preparation for *in situ* electrical-biasing characterization

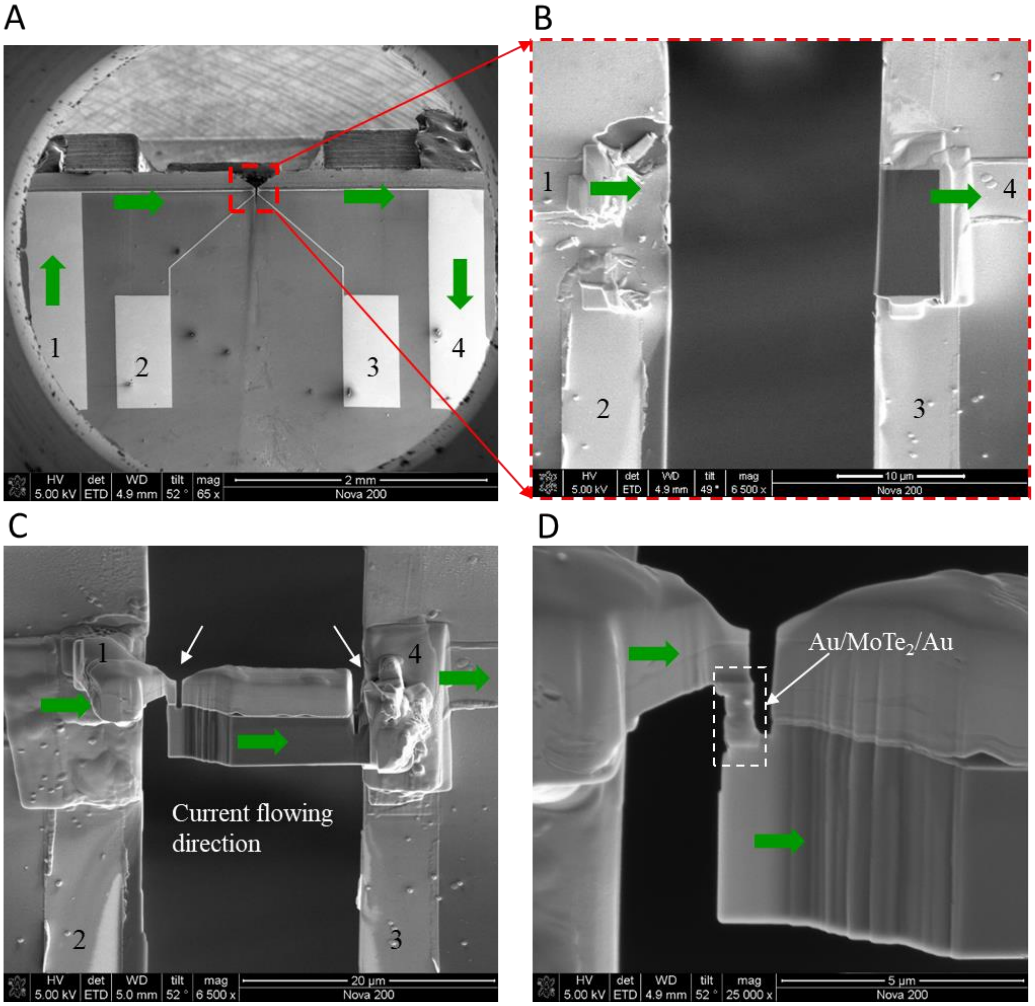

Figure A.1. MoTe$_2$ flake transfer and lamella fabrication for *in situ* electrical-biasing studies (A-B) SEM image of Protochips electrical E-chips (C-D) SEM image of a MoTe$_2$ lamella mounted between two electrodes. The special isolation in the lamella is carried out using FIB so that the electrical current can only flow along the guided direction (green arrows) to pass the Au/MoTe$_2$/Au structure.

A.2 Electrical biasing for thin and thick $MoTe_2$:

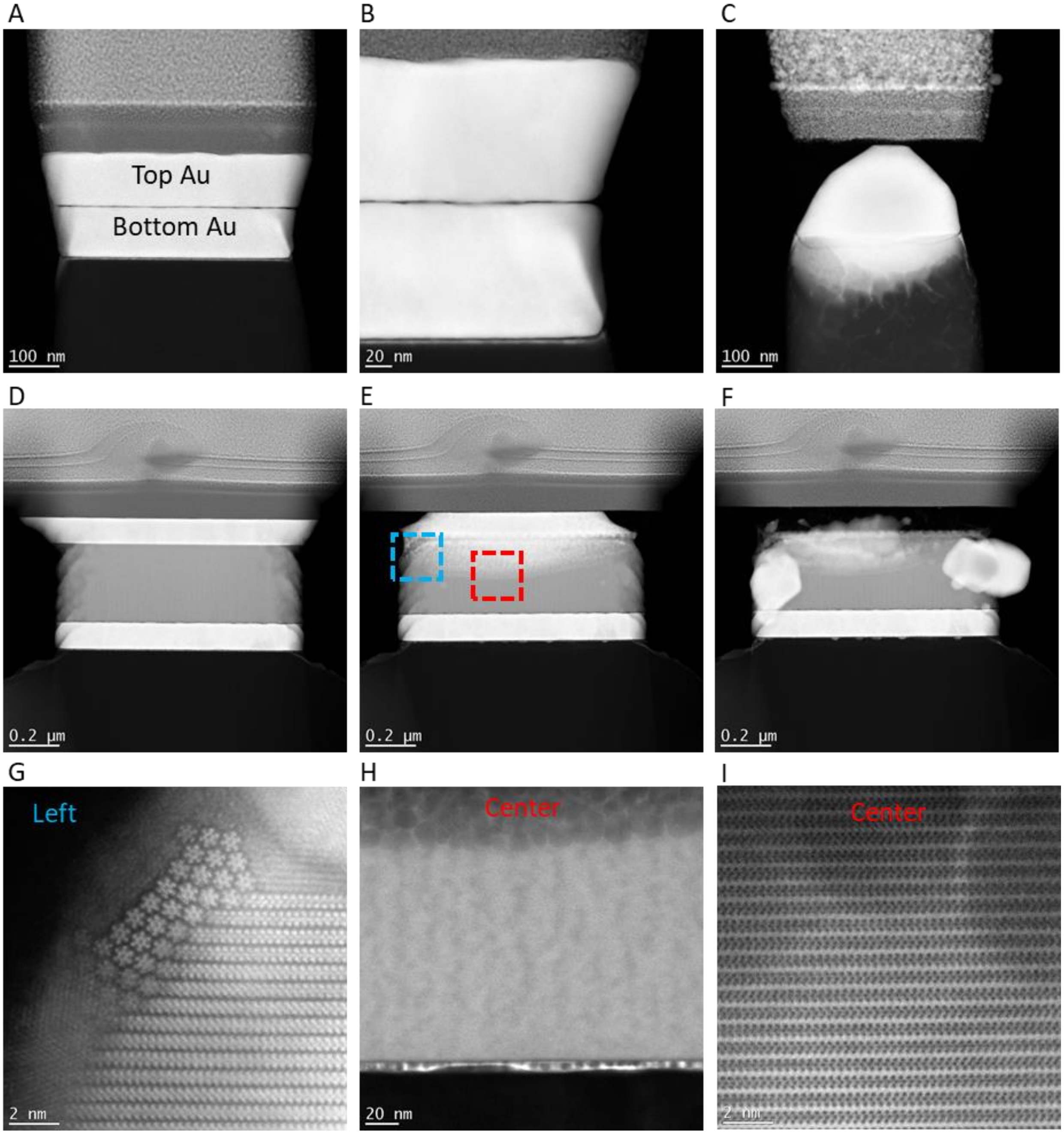

Figure A.2. (A-C) Electrical biasing for a thin $MoTe_2$ flake. The flake might be damaged during Au sputtering, resulting in the direct connection of the top and bottom Au layer. (D-F) Electrical biasing for a thick $MoTe_2$ flake. (G) Mo_6Te_6 NWs are observed at the flake edge. (H-I) The ABF image at the center of the flake shows some contrast change. However, the change of $MoTe_2$ lattice is not observed.

APPENDIX B

STABILITY AND STRUCTURE OF NW PHASE AFTER FORMATION

To elucidate the thermodynamic stability of Mo_6Te_6 NWs with multiple configurations, their formation energies are compared using density functional theory (DFT). The formation energy is normalized (eV/atom) for comparison purpose. For example, the formation energy for Mo_6Te_6_11° configuration is calculated by $\frac{E_{Mo_6Te_6}(11°)-6\mu_{Mo}-6\mu_{Te}}{12}$ and the formation energy for Mo_6Te_6 with one Te intercalated atom is calculated by $\frac{E_{Mo_6Te_6+Te}-6\mu_{Mo}-7\mu_{Te}}{13}$. They can be expressed as $E_f = \frac{E_{MoTe_x}-\mu_{Mo}-x\mu_{Te}}{1+x}$, where x indicates the Te/Mo stoichiometric ratio for different phases of molybdenum telluride ($MoTe_x$): Mo_6Te_6 (x=1), and Mo_6Te_6 NW with Te intercalation (x=7/6), etc. The chemical potential used in the formula is an independent parameter which is irrelevant with x. Its accurate value for this nonequilibrium phase transition is difficult to be calculated, so a rough but simple method is used instead. The total energy for Mo_6Te_6_11° configuration is selected as a reference value. For Te poor condition, the energy of bulk Mo is used to calculate μ_{Mo} and thus μ_{Te} is calculated using $\frac{E_{Mo_6Te_6}(11°)-6\mu_{Mo}}{6}$. While for Te rich condition, the energy of bulk Te is used to calculate μ_{Te} and thus μ_{Mo} is calculated using $\frac{E_{Mo_6Te_6}(11°)-6\mu_{Te}}{6}$. The formation energy for each $MoTe_x$ configuration under different chemical potential (i.e. Te poor and Te rich) has been calculated and listed in Table B.1.

Table B.1. The formation energy (Ef) schematic illustrations of different configurations of molybdenum tellurides. The formation energy is normalized to eV/atom.

	E_f(Te-poor) (eV/atom)	**E_f(Te-rich) (eV/atom)**	**Configuration**
Mo_6Te_6-11°	**0.000**	**0.000**	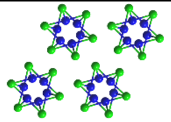
Mo_6Te_6-0°	**0.016**	**0.016**	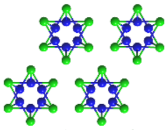
Mo_6Te_6-0°-Te-octahedral	**0.034**	**0.022**	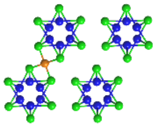
Mo_6Te_6-0°-Te-prismatic	**0.041**	**0.028**	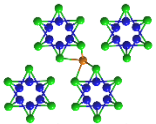
Mo_6Te_6-0°-Te - octahedral + prismatic	**0.078**	**0.055**	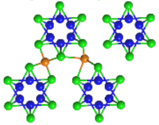
Mo_6Te_6-0°-Mo-octahedral	**0.061**	**0.073**	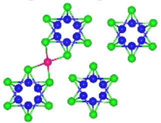

BIOGRAPHICAL SKETCH

Qingxiao Wang was born in Henan, China, in 1982. He received his bachelor's degree in 2003, majoring in Applied Physics, from The University of Science and Technology Beijing. After graduation, he worked in the failure analysis lab of Chartered Semiconductor as a senior engineer for 4 years, focusing on the material characterization using TEM. Then he worked in the Imaging and Characterization Core Lab at King Abdullah University of Science and Technology as a research engineer for 4 years, focusing on the aberration-corrected electron microscopy. In August 2014, he enrolled in the Materials Science and Engineering PhD program at The University of Texas at Dallas under the supervision of Dr. Moon J. Kim. His research focuses on the phase transition and defects study of 2D materials. His area of expertise includes the material characterization with *in situ* transmission electron microscopy (TEM) and focused ion beam (FIB).

CURRICULUM VITAE

Qingxiao Wang

Contact Information:

Dept. of Materials Science & Engineering
The University of Texas at Dallas
800 W. Campbell Rd.
Richardson, TX 75080, USA
E-mail: Qingxiao.Wang@utdallas.edu

Education:

Ph.D. in Materials Science and Engineering, The University of Texas at Dallas, 2020

Bachelor of Science in Applied Physics, University of Science and Technology Beijing, 2003

Experience:

The University of Texas at Dallas, Richardson, TX
Research Assistant, Department of Materials & Engineering 09/2014-present

King Abdullah University of Science and Technology, Thuwal, Saudi Arabia
Research Engineer, The Imaging and Characterization Core Lab 04/2010-08/2014

Chartered Semiconductor Manufacturing Ltd, Woodlands, Singapore
Senior Engineer, Failure Analysis Lab 09/2006-04/2010

Research Interests:

- Aberration-corrected electron microscopy
- *In situ* TEM characterization for nanomaterials and two-dimensional materials
- Focused ion beam related characterization techniques

Publications:

1. Qin, J.-K.; Liao, P.-Y.; Si, M.; Gao, S.; Qiu, G.; Jian, J.; **Wang, Q**.; Zhang, S.-Q.; Huang, S.; Charnas, A., Raman response and transport properties of tellurium atomic chains encapsulated in nanotubes. *Nature Electronics* **2020**, 1-7.

2. Zhu, H.; Addou, R.; **Wang, Q**.; Nie, Y.; Cho, K.; Kim, M.; Wallace, R., Surface and interfacial study of atomic layer deposited Al2O3 on MoTe2 and WTe2. *Nanotechnology* **2019**, 31 (5), 055704.

3. Wang, Y.; Wang, R.; Wan, S.; **Wang, Q**.; Kim, M. J.; Ding, D.; Wu, W., Scalable nanomanufacturing and assembly of chiral-chain piezoelectric tellurium nanowires for wearable self-powered cardiovascular monitoring. *Nano Futures* **2019**, 3 (1), 011001.

4. Shen, T.; Valencia, D.; **Wang, Q**.; Wang, K.-C.; Povolotskyi, M.; Kim, M. J.; Klimeck, G.; Chen, Z.; Appenzeller, J., MoS2 for Enhanced Electrical Performance of Ultrathin Copper Films. *ACS applied materials & interfaces* **2019**, 11 (31), 28345-28351.

5. Saharia, J.; Bandara, Y. N. D.; Lee, J. S.; **Wang, Q**.; Kim, M. J.; Kim, M. J., Fabrication of hexagonal boron nitride based 2D nanopore sensor for the assessment of electro-chemical responsiveness of human serum transferrin protein. *Electrophoresis* **2019**.

6. Pang, C.-S.; Hung, T. Y.; Khosravi, A.; Addou, R.; **Wang, Q**.; Kim, M. J.; Wallace, R. M.; Chen, Z., Atomically Controlled Tunable Doping in High Performance WSe2 Devices. arXiv preprint arXiv:1910.08619 **2019**.

7. Hadamek, T.; Shin, D.; Posadas, A.; Demkov, A.; Kwon, S.; **Wang, Q**.; Kim, M.; Rangan, S.; Bartynski, R. In Integration of Eu2O3 with GaN (0001) and determination fundamental material properties, *APS Meeting Abstracts,* **2019**.

8. Zhou, G.; Addou, R.; **Wang, Q**.; Honari, S.; Cormier, C. R.; Cheng, L.; Yue, R.; Smyth, C. M.; Laturia, A.; Kim, J., High-Mobility Helical Tellurium Field-Effect Transistors Enabled by Transfer-Free, Low-Temperature Direct Growth. *Advanced Materials* **2018**, 1803109.

9. Zhang, B.; Zheng, T.; **Wang, Q**.; Guo, Z.; Kim, M. J.; Alshareef, H. N.; Gnade, B. E., Stable and low contact resistance electrical contacts for high temperature SiGe thermoelectric generators. *Scripta Materialia* **2018**, 152, 36-39.

10. Wang, Y.; Qiu, G.; Wang, R.; Huang, S.; **Wang, Q**.; Liu, Y.; Du, Y.; Goddard, W. A.; Kim, M. J.; Xu, X.; Ye, P. D.; Wu, W., Field-effect transistors made from solution-grown two-dimensional tellurene. *Nature Electronics* **2018**, 1 (4), 228-236.

11. Wan, S.; **Wang, Q**.; Ye, H.; Kim, M. J.; Xia, X., Pd–Ru Bimetallic Nanocrystals with a Porous Structure and Their Enhanced Catalytic *Properties. Particle & Particle Systems Characterization* **2018**.

12. Nie, Y.; Barton, A.; Addou, R.; Zheng, Y.; Walsh, L.; Eichfield, S.; Yue, R.; Cormier, C.; Zhang, C.; **Wang, Q**., Dislocation driven spiral and non-spiral growth in layered chalcogenides: morphology, mechanism, and mitigation. *Nanoscale* **2018**.

13. Kormondy, K. J.; Cho, Y.; Posadas, A. B.; Zheng, L.; Lai, K.; **Wang, Q**.; Kim, M. J.; He, Q.; Borisevich, A. Y.; Downer, M. C., Piezoelectric modulation of nonlinear optical response in BaTiO3 thin film. *Applied Physics Letters* **2018**, 113 (13), 132902.

14. Che, Z.; Li, J.; **Wang, Q**.; Wang, L.; Zhang, H.; Zhang, Y.; Wang, X.; Wang, J.; Kim, M. J., The formation of atomic-level interfacial layer and its effect on thermal conductivity of W-coated diamond particles reinforced Al matrix composites. Composites Part A: *Applied Science and Manufacturing* **2018**, 107, 164-170.

15. Chaney, A.; Turski, H.; Nomoto, K.; **Wang, Q.**; Hu, Z.; Kim, M.; Xing, H. G.; Jena, D. In Realization of the first GaN based tunnel field-effect transistor, *2018 76th Device Research Conference (DRC)*, IEEE: **2018**; pp 1-3.

16. Zhu, H.; **Wang, Q**.; Zhang, C.; Addou, R.; Cho, K.; Wallace, R. M.; Kim, M. J., New Mo6Te6 Sub-Nanometer-Diameter Nanowire Phase from 2H-MoTe2. *Advanced Materials* **2017**, 29 (18), 1606264.

17. Zhu, H.; **Wang, Q.**; Cheng, L.; Addou, R.; Kim, J.; Kim, M. J.; Wallace, R. M., Defects and surface structural stability of MoTe2 under vacuum annealing. *ACS Nano* **2017**, 11 (11), 11005-11014.

18. Zhang, B.; Zheng, T.; **Wang, Q**.; Zhu, Y.; Alshareef, H. N.; Kim, M. J.; Gnade, B. E., Contact resistance and stability study for Au, Ti, Hf and Ni contacts on thin-film Mg2Si. *Journal of Alloys and Compounds* **2017**, 699, 1134-1139.

19. **Wang, Q.**; Zhu, H.; Zhang, C.; Addou, R.; Cho, K.; Wallace, R. M.; Kim, M. J., *In Situ* Heating Study of 2H-MoTe2 to Mo6Te6 Nanowire Phase Transition. Microscopy and Microanalysis **2017**, 23 (S1), 1764-1765.

20. Walsh, L. A.; Smyth, C. M.; Barton, A. T.; **Wang, Q**.; Che, Z.; Yue, R.; Kim, J.; Kim, M. J.; Wallace, R. M.; Hinkle, C. L., Interface Chemistry of Contact Metals and Ferromagnets on the Topological Insulator Bi2Se3. *The Journal of Physical Chemistry C* **2017**, 121 (42), 23551-23563.

21. Lund, C.; Romanczyk, B.; Catalano, M.; **Wang, Q**.; Li, W.; DiGiovanni, D.; Kim, M. J.; Fay, P.; Nakamura, S.; DenBaars, S. P.; Mishra, U. K.; Keller, S., Metal-organic chemical vapor

deposition of high quality, high indium composition N-polar InGaN layers for tunnel devices. *Journal of Applied Physics* **2017**, 121 (18), 185707.

22. Lee, A. W.; Ruoyu, Y.; **Qingxiao, W.**; Adam, T. B.; Rafik, A.; Christopher, M. S.; Hui, Z.; Jiyoung, K.; Luigi, C.; Moon, J. K.; Robert, M. W.; Christopher, L. H., W Te 2 thin films grown by beam-interrupted molecular beam epitaxy. *2D Materials* **2017**, 4 (2), 025044.

23. Hestroffer, K.; Lund, C.; Koksaldi, O.; Li, H.; Schmidt, G.; Trippel, M.; Veit, P.; Bertram, F.; Lu, N.; **Wang, Q**.; Christen, J.; Kim, M. J.; Mishra, U. K.; Keller, S., Compositionally graded InGaN layers grown on vicinal N-face GaN substrates by plasma-assisted molecular beam epitaxy. *Journal of Crystal Growth* **2017**, 465, 55-59.

24. Hadamek, T.; Shin, D.; Posadas, A. B.; Demkov, A. A.; Kwon, S.; **Wang, Q**.; Kim, M., Hexagonal to monoclinic phase transformation in Eu2O3 thin films grown on GaN (0001). *Applied Physics Letters* **2017**, 111 (14), 142901.

25. Cheng, L.; Lee, J.; Zhu, H.; Ravichandran, A. V.; **Wang, Q**.; Lucero, A. T.; Kim, M. J.; Wallace, R. M.; Colombo, L.; Kim, J., Sub-10 nm Tunable Hybrid Dielectric Engineering on MoS2 for Two-Dimensional Material-Based Devices. *ACS Nano* **2017**, 11 (10), 10243-10252.

26. Chen, P.-Y.; Posadas, A. B.; Kwon, S.; **Wang, Q**.; Kim, M. J.; Demkov, A. A.; Ekerdt, J. G., Cubic crystalline erbium oxide growth on GaN (0001) by atomic layer deposition. Journal of Applied Physics **2017**, 122 (21), 215302.

27. Burg, G. W.; Prasad, N.; Fallahazad, B.; Valsaraj, A.; Kim, K.; Taniguchi, T.; Watanabe, K.; **Wang, Q**.; Kim, M. J.; Register, L. F.; Tutuc, E., Coherent Interlayer Tunneling and Negative Differential Resistance with High Current Density in Double Bilayer Graphene–WSe2 Heterostructures. *Nano Letters* **2017**, 17 (6), 3919-3925.

28. Barrera, D.; **Wang, Q**.; Lee, Y.-J.; Cheng, L.; Kim, M. J.; Kim, J.; Hsu, J. W. P., Solution synthesis of few-layer 2H MX2 (M = Mo, W; X = S, Se*). Journal of Materials Chemistry C* **2017**, 5 (11), 2859-2864.

29. Barrera, D.; Jawaid, A.; Daunis, T. B.; Cheng, L.; **Wang, Q**.; Lee, Y.-J.; Kim, M. J.; Kim, J.; Vaia, R. A.; Hsu, J. W. P., Inverted OPVs with MoS2 hole transport layer deposited by spray coating. *Materials Today Energy* **2017**, 5, 107-111.

30. Azcatl, A.; **Wang, Q**.; Kim, M. J.; Wallace, R. M., Al2O3 on WSe2 by ozone based atomic layer deposition: Nucleation and interface study. *APL Materials* **2017**, 5 (8), 086108.

31. Ye, H.; **Wang, Q**.; Catalano, M.; Lu, N.; Vermeylen, J.; Kim, M. J.; Liu, Y.; Sun, Y.; Xia, X., Ru Nanoframes with an fcc Structure and Enhanced Catalytic Properties. *Nano Letters* **2016**.

32. Ye, H.; Mohar, J.; **Wang, Q**.; Catalano, M.; Kim, M. J.; Xia, X., Peroxidase-like properties of Ruthenium nanoframes. *Science Bulletin* **2016**, 61 (22), 1739-1745.

33. **Wang, Q**.; Wang, J.; Kim, M. J., Simple Specimen Preparation Method for *In Situ* Heating Experiments. *Microscopy and Microanalysis* **2016**, 22 (S3), 132-133.

34. Vilá, R. A.; Momeni, K.; **Wang, Q**.; Bersch, B. M.; Lu, N.; Kim, M. J.; Chen, L. Q.; Robinson, J. A., Bottom-up synthesis of vertically oriented two-dimensional materials. *2D Materials* **2016**, 3 (4), 041003.

35. Tang, S.; Peng, C.; Xu, J.; Du, B.; **Wang, Q**.; Vinluan, R. D.; Yu, M.; Kim, M. J.; Zheng, J., Tailoring Renal Clearance and Tumor Targeting of Ultrasmall Metal Nanoparticles with Particle Density. *Angewandte Chemie* **2016,** 128 (52), 16273-16277.

36. Gopalan, D. P.; Mende, P. C.; de la Barrera, S. C.; Dhingra, S.; Li, J.; Zhang, K.; Simonson, N. A.; Robinson, J. A.; Lu, N.; **Wang, Q**.; Kim, M. J.; D'Urso, B.; Feenstra, R. M., Formation of hexagonal boron nitride on graphene-covered copper surfaces. *Journal of Materials Research* **2016**, 31 (07), 945-958.

37. Desai, S. B.; Madhvapathy, S. R.; Sachid, A. B.; Llinas, J. P.; **Wang, Q**.; Ahn, G. H.; Pitner, G.; Kim, M. J.; Bokor, J.; Hu, C.; Wong, H.-S. P.; Javey, A., MoS2 transistors with 1-nanometer gate lengths. *Science* **2016**, 354 (6308), 99-102.

38. Azcatl, A.; Qin, X.; Prakash, A.; Zhang, C.; Cheng, L.; **Wang, Q**.; Lu, N.; Kim, M. J.; Kim, J.; Cho, K.; Addou, R.; Hinkle, C. L.; Appenzeller, J.; Wallace, R. M., Covalent Nitrogen Doping and Compressive Strain in MoS2 by Remote N2 Plasma Exposure. *Nano Letters* **2016**, 16 (9), 5437-5443